UNICAMP

UNIVERSIDADE ESTADUAL DE CAMPINAS

Instituto de Física
Gleb Wataghin

ITALO LAMBERT SOARES ANDRADE

Estudo de Acoplamento Magnético entre Microfios Metálicos e Cavidades 3D Induzido Eletricamente

Study of Electrically Induced Magnetic Coupling Between Metallic Microwires and 3D Cavities

Campinas

2025

Italo Lambert Soares Andrade

Study of Electrically Induced Magnetic Coupling Between Metallic Microwires and 3D Cavities

Estudo de Acoplamento Magnético entre Microfios Metálicos e Cavidades 3D Induzido Eletricamente

Dissertation presented to the Institute of Physics Gleb Wataghin of the University of Campinas in partial fulfillment of the requirements for the degree of Master in Physics, in the area of Physics.

Dissertação apresentada ao Instituto Física Gleb Wataghin da Universidade Estadual de Campinas como parte dos requisitos exigidos para a obtenção do título de Mestre em Física, na área de Física.

Supervisor: Prof. Dr. Francisco Paulo Marques Rouxinol

Co-supervisor: Prof. Dr. Amir Ordacgi Caldeira

Este trabalho corresponde à versão final da Dissertação defendida pelo aluno Italo Lambert Soares Andrade e orientada pelo Prof. Dr. Prof. Dr. Francisco Paulo Marques Rouxinol.

Campinas

2025

Ficha catalográfica
Universidade Estadual de Campinas (UNICAMP)
Biblioteca do Instituto de Física Gleb Wataghin
Lucimeire de Oliveira Silva da Rocha - CRB 8-9174

An24s

Andrade, Italo Lambert Soares, 2000-
Study of electrically induced magnetic coupling between metallic microwires and 3D cavities / Italo Lambert Soares Andrade. – Campinas, SP : [s.n.], 2025.

Orientador: Francisco Paulo Marques Rouxinol.
Coorientador: Amir Ordacgi Caldeira.
Dissertação (mestrado) – Universidade Estadual de Campinas (UNICAMP), Instituto de Física Gleb Wataghin.

1. Magnônica de cavidade. 2. Spintrônica. 3. Ressonância ferromagnética. 4. Microfios. 5. Materiais magnéticos. I. Rouxinol, Francisco Paulo Marques, 1977-. II. Caldeira, Amir Ordacgi, 1950-. III. Universidade Estadual de Campinas (UNICAMP). Instituto de Física Gleb Wataghin. IV. Título.

Informações complementares

Título em outro idioma: Estudo de acoplamento magnético entre microfios metálicos e cavidades 3D induzido eletricamente
Palavras-chave em inglês:
Cavity magnonic
Spintronics
Ferromagnetic resonance
Microwires
Magnetic materials
Área de concentração: Física
Titulação: Mestre em Física
Banca examinadora:
Francisco Paulo Marques Rouxinol [Orientador]
Pascoal José Giglio Pagliuso
Sean Richard Giblin
Data de defesa: 20-03-2025
Programa de Pós-Graduação: Física

Objetivos de Desenvolvimento Sustentável (ODS)
Não se aplica

Identificação e informações acadêmicas do(a) aluno(a)
- ORCID do autor: https://orcid.org/0009-0006-0186-9981
- Currículo Lattes do autor: http://lattes.cnpq.br/2604106458073703

- Prof. Dr. Francisco Paulo Marques Rouxinol (IFGW/ UNICAMP) - Presidente e Orientador

- Prof. Dr. Pascoal José Giglio Pagliuso (IFGW/ UNICAMP)

- Prof. Dr. Sean Richard Giblin (Cardiff University)

A ata da defesa com as respectivas assinaturas dos membros encontra-se no SIGA/Sistema de Fluxo de Dissertação/Tese e na Secretaria do Programa da Unidade.

Acknowledgements

A master's program is intensive and fast. Yet, during these two transformative years I had the opportunity to learn with and enjoy the company of several kind people. I would like to thank my senior lab colleagues: Lucas Ruela, Gustavo Moreto, Ednilson Lopes and Diego Molina, who taught me a lot and were always available to help; the lab undergraduate students: Mariana, Beatriz, Valentina, Ágatha and Kawan for their support and for giving me the chance to try explaining what I was doing; the postdocs at LMBT, Alberto, and especially Pablo Ribeiro who helped me get my project started; the LMBT PhD student Lucas Palhares; Jorge, o Bom, for teaching me about screws and for the ever-present willingness to help; André, for the patience and the amazing job in my copper machined parts; Alfredo from CCS Nano for the help with the FIB; Flávio Gandra for teaching me a little bit about PLL ESR; my colleagues during the courses that helped me through the tough lists, as well as many others Unicamp students and staff, who definitely contributed to my formation in some way.

I would like to give special thanks for the Professors Kleber Pirota and Amir Caldeira for the discussions and help with this problem. I also thank Amir for the classes and the physics discussions in his office; I was always impressed by his fast reasoning and profound knowledge of physics. Finally, I could not be more grateful to my supervisor, Francisco Rouxinol, who far beyond teaching me only physics, taught me to be a better student, a better professional; to be a physicist. He made me look at aspects of the scientific work which I did not pay attention to, and also taught me to always be active toward my goals. I am sure his supervision will have profound impacts in my career and life.

This study was financed in part by the Coordenação de Aperfeiçoamento de Pessoal de Nível Superior – Brasil (CAPES) – Finance Code 001 via the process 88887.822401/2023-00. I thank CAPES for this scholarship that allowed me to dedicate myself fully to my studies over the past two years. I would also like to thank the São Paulo Research Foundation (FAPESP), Brazil, for the essential funding support provided through Grant numbers 2017/08602-0, 2017/22035-1, and 2017/22037-4, which enabled the acquisition of key equipment and the establishment of this remarkable laboratory. I am also grateful to the NAMITEC INCT, under Grant number 406193/2022-3, and to the Associação para Promoção da Excelência do Software Brasileiro – SOFTEX, under Grant number 01245.002636/2023-81, for their financial support. I thank Engineering Simulation and Scientific Software (ESSS) for funding the ANSYS software license, and Autodesk for their Student Access on Inventor.

Finally, I thank the Physics Graduate Office for their efforts in expediting the preparations for my defense.

Abstract

This master's thesis presents the results of a study conducted at the Laboratory of Physics of Quantum Devices (LFDQ) and Laboratory of Materials and Low Temperatures (LMBT), whose goal was to investigate, in the context of the newly developing field of cavity magnonics, the interaction of microwaves with metallic microwires of CoFeSiB. The focus is on the characterization of the ferromagnetic resonance and the nature of the coupling. The metallic character imposes challenges in describing this resonance due to skin effect, but it also allows for the resonance to be driven by the strong induced magnetic field of the currents generated by an impinging electric field, ultimately realizing an electrically mediated coupling. It is this coupling that is discussed and studied in this work.

First, the physics of ferromagnetic resonance, including its behaviour in the presence of metallic materials, is presented, together with the description of the photon-magnon coupling as two coupled harmonic oscillators. The two are related by dissipation in the weak coupling regime. Then the microwires and their characteristics are presented. Following, the main experimental techniques used are explained, and finally the results of the experiments are displayed and analysed.

The main results are that the ferromagnetic resonance occurs at the Kittel plane resonance condition – due to the smallness of the skin depth –, and that the coupling with the electric field is not only realizable, but much stronger than the magnetic counterpart. Coupling strengths of over 50 MHz were achievable, although the magnetic dissipation of the system is too large ($>$ 800 MHz) making it impossible a strong coupling regime, and hence coherent coupling, to be reached.

The possibility of using the metallic character to realize this electrical coupling has not yet been explored in cavity magnonics, although metallic materials like permalloy have been studied. This work should raise the awareness about the importance of considering the metallic character of samples in studying cavity magnonics, including their geometry and electromagnetic environment.

Keywords: Cavity Magnonics; Spintronics; Ferromagnetic Resonance; Microwires; Magnetic Materials

Resumo

Esta tese de mestrado apresenta os resultados de um estudo conduzido no Laboratório de Física de Dispositivos Quânticos (LFDQ) e no Laboratório de Materiais e Baixas Temperaturas (LMBT), cujo objetivo era investigar, sob o contexto da magnônica de cavidades, a interação de microondas com microfios de CoFeSiB. O foco é na caracterização da ressonância ferromagnética e a natureza do acoplamento. O caráter metálico dos fios impõe um desafio na descrição dessa ressonância, devido ao efeito pelicular, mas também permite a ressonância ser induzida pelos fortes campos magnéticos das correntes geradas por um campo elétrico incidente, realizando um acoplamento mediado eletricamente. É este acoplamento que é discutido e estudado nesse trabalho.

Primeiramente, a física da ressonância ferromagnética, incluindo sob a presença de materiais metálicos é apresentada, junto com a descrição do acoplamento fóton-magnon como dois osciladores harmônicos acoplados. As duas descrições são relacionadas pela dissipação no regime de acoplamento fraco. Os microfios são apresentados e, logo após, as técnicas e os aparatos experimentais; por fim, os resultados dos experimentos são mostrados e analisados.

Os resultados principais são que, devido ao efeito pelicular, a ressonância ferromagnética acontece na condição de ressonância de Kittel para o plano e que o acoplamento com o campo elétrico não é apenas realizável, mas muito mais forte que o magnético. Acoplamentos acima de 50 MHz foram alcançados, porém a dissipação no sistema magnético era muito grande ($>$ 800 MHz) impossibilitando alcançar o regime de acoplamento forte, e portanto de acoplamento coerente.

A possibilidade de usar o caráter metálico para realizar esse acoplamento elétrico ainda não foi explorada em magnônica de cavidades, embora materiais metálicos, como permalloy, tenham sido estudados. Este trabalho deve levantar a importância de se considerar o caráter metálico das amostras ao estudar magnônica de cavidades, incluindo sua geometria e ambiente electromagnético.

Palavras-chave: Magnônica de Cavidades; Spintrônica; Ressonância Ferromagnética; Microfios; Materiais Magnéticos

Contents

Introduction

The recent technological advancements and foundational studies in quantum mechanics, in which single quantum systems are being measured and controlled, are inserted in the so-called second quantum revolution (DOWLING; MILBURN, 2002). In contrast to the first that saw the creation of the theory in the early 20th century and, later, the blooming of based technologies like transistors and lasers, now the technology of this second revolution has quantum mechanics as an essential *modus operandi*, harnessing superposition, entanglement and coherence for applications in communication, metrology and information processing. One of its landmarks was the development of Cavity Quantum Electrodynamics (cavity QED), where the quantum states of Rydberg atoms in microwave cavities and photons were directly measured and controlled (HAROCHE; RAIMOND, 2006), realizing several achievements in quantum optics that were once inconceivable. Later, a team in Yale developed a platform using superconducting circuits to perform experiments of cavity QED and achieve coupling regimes impossible with natural atoms (WALLRAFF et al., 2004) and with a high potential of scalability that is nowdays the leading technology towards the development of a quantum computer (HUANG et al., 2020)

Hybrid quantum systems leverage the physical properties of different platforms and are an innate source of interest due to combined functionalities that are useful to engineer different quantum devices and allow the study of these systems in the quantum regime. Cavity Magnonics (RAMESHTI et al., 2022) study one of such systems, namely the hybrids of confined photons in cavities with magnetic orderly systems that have magnons as a fundamental collective excitation. The study of the interaction of magnets with microwaves is not new and has been extensively explored in ferromagnetic resonance experiments for decades (GRIFFITHS, 1946; KITTEL, 1947). Though the focus was usually on the characterization of the material or of the spin waves, and not on the interaction itself or coherence. In 2010, Soykal and Flatté (SOYKAL; FLATTÉ, 2010) predicted that strong coupling could be achievable between a cavity and a nanomagnet with the formation of photon-spin entangled states. In 2013, Huebl (HUEBL et al., 2013) achieved strong coupling between a Yttrium Iron Garnet (YIG) crystal and a superconducting resonator. Different coupling regimes were explored by Zhang (ZHANG et al., 2014) at room temperature, and the coherent coupling of a YIG sphere with a 3D cavity was used by Nakamura's group to realize an effective interaction with a superconducting qubit, allowing the detection, in the dispersive regime, of single magnons (LACHANCE-QUIRION et al., 2017), opening the avenue of quantum magnonics (YUAN et al., 2022).

The common material used for these experiments is YIG, as it have a high spin density that collectively increases the coupling and extremely low magnetic dissipation.

Other materials like permalloy (PY) films in specifically engineered resonators have been studied (HOU; LIU, 2019). In this work, a different material is explored: amorphous CoFeSiB metallic microwires. They have been the focus of many studies due to their Giant Magneto Impedance and other useful magnetic properties (CHIRIAC; ÓVáRI, 1996) . Ferromagnetic resonance in those wires is challenging due to their metallic character that makes their response highly dependent on the electromagnetic environment and skin-depth. For instance, in 1959, Rodbell performed ferromagnetic resonance measurements in iron whiskers (RODBELL, 1959a) and showed that a resonance could be driven by the circular magnetic field induced by the electric field in the whisker. This configuration is sometimes used to study thin wires, and here we use it to study their cavity-magnetic coupling. No strong coupling was achieved due to high dissipation, but the interaction was analysed using cavity electrodynamics, yielding interesting results.

1 Theory of the Interaction of Microwaves with Magnets and Wires

This chapter presents the theory of magnets coupled with microwave photons in a cavity and ferromagnetic resonance in metallic wires. These concepts form the basis used for interpreting the experiments discussed in subsequent chapters.

1.1 Microwave Cavity

A three-dimensional microwave cavity is a metallic shell on the order of a few centimetres, enclosing a hollow or dielectric-filled region of space that supports resonant microwaves. In this work, we employed nearly rectangular cavities, machined from metal blocks with polished inner surfaces to maximize the cavity's quality factor. Small apertures allow antennas to be inserted, which can be used to inject and detect microwaves by coupling to the fields inside the cavity. Figure 1 shows an example of one of the cavities used (Cavity A).

Figure 1 – Open aluminium cavity. The two parts fit over each other, enclosing a prismatic hollow space with an almost rectangular cross-section. SMA pins (circled in red) serve as antennas connecting the cavity to external waveguides. Different pin sizes lead to different coupling strengths for each port. The dimensions of this cavity are: 26 mm × 8 mm × 36 mm.

The highly conductive walls of the cavity impose boundary conditions on the electromagnetic fields, resulting in a discrete spectrum of resonant modes. An estimation of the first resonant modes of a rectangular cavity can be made considering a rectangular box of perfectly conducting surfaces. This system is the same as a rectangular waveguide shorted by planes at the ends. The task is to solve Maxwell equations inside the waveguide with the boundary conditions: $\mathbf{E}_{\parallel} = \mathbf{B}_{\perp} = 0$ on the walls of the waveguide and then short the ends (JACKSON, 1962; GRIFFITHS, 2013).

The coordinates are defined such that the z direction is along the longest length – the axis of the waveguide – and y is along shortest. It is convenient to separate the z and t dependence of the fields with the ansatz:

$$\begin{aligned} \mathbf{E}(\mathbf{r},t) &= \widetilde{\mathbf{E}}(x,y)e^{i(k_z z-\omega t)}, \\ \mathbf{B}(\mathbf{r},t) &= \widetilde{\mathbf{B}}(x,y)e^{i(k_z z-\omega t)}, \end{aligned} \tag{1.1}$$

where ω is the frequency of the wave, k_z is the z-direction wavenumber. The Maxwell equations then turn into the waveguide Maxwell equations:

$$\begin{aligned} \boldsymbol{\nabla}\cdot\mathbf{B} &= 0 & \boldsymbol{\nabla}\cdot\mathbf{E} &= 0 \\ \boldsymbol{\nabla}\times\mathbf{E} &= i\omega\mathbf{B} & \boldsymbol{\nabla}\times\mathbf{B} &= -\frac{i\omega}{c^2}\mathbf{E} \end{aligned} \tag{1.2}$$

Because of the boundary conditions of the hollow waveguide, waves with $E_z = B_z = 0$, the so-called transverse electric magnetic (TEM) waves, cannot exist. The possible modes are then either transverse electric (TE) $E_z = 0$ or transverse magnetic (TM) $B_z = 0$. For the TE modes, Equations 1.1 and 1.2 yield:

$$\begin{aligned} \widetilde{B_x} &= \frac{ik_z}{(\omega/c)^2 - k_z^2}\frac{\partial\widetilde{B_z}}{\partial x}, & \widetilde{E_x} &= \frac{i\omega}{(\omega/c)^2 - k_z^2}\frac{\partial\widetilde{B_z}}{\partial y}, \\ \widetilde{B_y} &= \frac{ik_z}{(\omega/c)^2 - k_z^2}\frac{\partial\widetilde{B_z}}{\partial y}, & \widetilde{E_y} &= -\frac{i\omega}{(\omega/c)^2 - k_z^2}\frac{\partial\widetilde{B_z}}{\partial x}, \\ & \left(\frac{\partial^2}{\partial x^2} + \frac{\partial^2}{\partial y^2} + (\omega/c)^2 - k_z^2\right)\widetilde{B_z} = 0. \end{aligned} \tag{1.3}$$

Solving for these waves in a rectangular waveguide with dimensions L_x and L_y the magnetic field in the z direction is given by $\widetilde{B_z} = B_{z0}\cos(k_x x)\cos(k_y y)$, where $k_x = n\pi/L_x$ and $k_y = m\pi/L_y$ are the wave vectors that meet the boundary condition and are constrained by $(\omega/c)^2 = k_z^2 + k_x^2 + k_y^2$. Closing this waveguide with rectangular planes creates a cavity, where the propagating and reflected fields sum to create a standing wave: $\mathbf{B} = (\widetilde{\mathbf{B}}(x,y,k_z)e^{ik_z z} - \widetilde{\mathbf{B}}(x,y,-k_z)e^{-ik_z z})e^{-i\omega t}$. The z wavevector with this new boundary condition becomes $k_z = l\pi/L_z$, leading to the field configuration:

$$\begin{aligned}
B_x &= B_{x0}\sin(k_x x)\cos(k_y y)\cos(k_z z),\\
B_y &= B_{y0}\cos(k_x x)\sin(k_y y)\cos(k_z z),\\
B_z &= B_{z0}\cos(k_x x)\cos(k_y y)\sin(k_z z),\\
E_x &= E_{x0}\cos(k_x x)\sin(k_y y)\sin(k_z z),\\
E_y &= E_{y0}\sin(k_x x)\cos(k_y y)\sin(k_z z).
\end{aligned} \tag{1.4}$$

Similarly, the TM waves can be solved. The resonance frequency for both mode types are given by:

$$f_{nkl} = \frac{c}{2}\sqrt{\left(\frac{n}{L_x}\right)^2 + \left(\frac{k}{L_y}\right)^2 + \left(\frac{l}{L_z}\right)^2}. \tag{1.5}$$

The possible TE$_{nkl}$ modes have $l \neq 0$ and at least one, n or k, different than zero as well. For TM modes, both n and k have to be different to zero, so the dominant (lowest frequency) TE mode is TE$_{101}$ and the dominant TM mode is TM$_{110}$. Because of these conditions, in rectangular cavities, several TE modes will have lower frequencies than TM modes.

An important property of a cavity mode is the quality factor which is an expression of the total losses of that mode and it is defined as $Q = 2\pi\times$energy stored/energy lost per cycle. It is related to the width at half height of the transmission peak at resonance by:

$$Q = \frac{f_c}{\Delta f_{3dB}}; \tag{1.6}$$

that is also related to the dissipation rate $\kappa = 2\pi\Delta f_{3dB}$ (see Section 4.1 and Appendix C). The total loss of a cavity mode is a sum of its coupling with the exterior $\kappa_{ex} = \kappa_{1ex} + \kappa_{2ex}$, where κ_{iex} refer to the coupling with port i, and the internal losses κ_{int} that arises from finite conductivity, surface imperfections, impurities, etc.

The quantization of the electromagnetic field involves associating a harmonic oscillator to each field mode (STECK, 2012). Considering a one-mode cavity, its Hamiltonian is thus given by:

$$\mathcal{H}_c = \hbar\omega_c a^\dagger a. \tag{1.7}$$

The electric and magnetic fields are promoted to operator fields and have a distribution given by the mode functions (the spatial solution of Maxwell's Equation, like the configurations given by 1.4). For example, the magnetic field has the form:

$$\mathbf{B} = \mathbf{B}_{ZPF}(\mathbf{r})(ae^{-i\omega_c t} + a^\dagger e^{i\omega_c t}), \tag{1.8}$$

where $\mathbf{B}_{ZPF}$ refers to the zero-point fluctuation of the field ($\sqrt{\langle 0|\,\Delta B^2\,|0\rangle}$) that is proportional to the normalized mode distribution of the magnetic field $\mathbf{f}_B$:

$$\mathbf{B}_{ZPF} = \sqrt{\frac{\hbar}{2\omega\epsilon_0}}\mathbf{f}_B. \tag{1.9}$$

1.2 Micromagnetics

Ferromagnetism can be explained by the Heisenberg model where the Coulomb force between electrons and the Pauli exclusion principle give rise to an effective interaction between neighboring spins called exchange interaction. This interaction has the form:

$$\mathcal{H} = -J \sum_{<i,j>} \mathbf{S}_i \cdot \mathbf{S}_j, \tag{1.10}$$

where the sum is taken over neighboring spins. As a consequence, when $J > 0$, the ground state of this Hamiltonian has all spins aligned in the same direction, resulting in the spontaneous magnetization characteristic of ferromagnetism.

Besides the exchange interaction, there are other competing energies that influences the static configuration of mesoscopic magnetization, such as long-range dipole-dipole interaction, spin-orbit coupling, external and internal fields. Mesoscopically, these effects can be phenomenologically accounted for by a magnetic free energy functional $F[\mathbf{M}(\mathbf{r})]$. The approach of micromagnetics minimizes this functional with the constraint $\mathbf{M}^2 = M_s^2$, where M_s refers to the saturation magnetization – where all spins are aligned, except for thermal fluctuations – determining the equilibrium configuration of $\mathbf{M}(\mathbf{r})$ in the material, allowing one to calculate, for example, the formation of magnetic domains (LANDAU; LIFSHITZ, 1935; HUBERT; SCHäFER, 1998; CALDEIRA, 2014; BROWN, 1963).

The exchange interaction (Equation 1.10) is responsible for a magnetic stiffness term in the free energy density proportional to $(\nabla\mathbf{M})^2$ that is a minimum when the magnetization is uniform. Usually, in a crystalline material there will also be an anisotropy term that comes from the spin-orbit coupling of the electrons, where the orbital part is affected by the electric field of the spatially ordered ions (REZENDE, 2020). In our case, the microwires are amorphous, so there is no crystalline anisotropy. Instead, there is an anisotropy that comes from stresses ($\sigma_{i,j}$) through the magnetoelastic energy $u_{me}(\mathbf{M}, \sigma)$. This energy is related to elastic deformations caused by changes in magnetization – magnetostriction – and vice-versa. This energy will depend on the magnetostriction constant λ.

Finally, there are the energies of dipoles immersed in a magnetic field. There is a self-dipolar energy associated to the interaction of the dipoles with the field $\mathbf{H}_D$ produced by the magnet itself (see Appendix A), and there is the interaction with an external field $\mathbf{H}_0$. Combining all these energies, the free energy becomes:

$$F[\mathbf{M}(\mathbf{r})] = \int dV \left[\frac{A}{M_s^2} (\nabla\mathbf{M})^2 + u_{me}(\mathbf{M}, \sigma) - \frac{\mu_0}{2} \mathbf{H}_D \cdot \mathbf{M} - \mu_0 \mathbf{H}_0 \cdot \mathbf{M} \right] \tag{1.11}$$

1.3 Basic Theory of Ferromagnetic Resonance

1.3.1 Electron Precession

The relationship between the electron magnetic moment and spin angular momentum is given by its gyromagnetic ratio γ:

$$\boldsymbol{\mu} = -\gamma \mathbf{S}, \tag{1.12}$$

that equals:

$$\gamma = \frac{g_e e}{2m_e} \approx 2\pi \times 28 \text{ GHz/T}, \tag{1.13}$$

where m_e and e are, respectively, its mass and charge, and $g_e \approx 2$ is the g-factor that is approximately obtained by the non-relativistic limit of Dirac equation.

When a magnetic dipole is placed in a magnetic field $\mathbf{B}$, it experience a torque:

$$\tau = \boldsymbol{\mu} \times \mathbf{B}, \tag{1.14}$$

and because the magnetic dipole is related to the angular momentum, the effect is not actually a rotation of dipole – as it happens in the electric case – but a precession (Figure 2a) around the direction of the field given by:

$$\dot{\boldsymbol{\mu}} = -\gamma \boldsymbol{\mu} \times \mathbf{B} \tag{1.15}$$

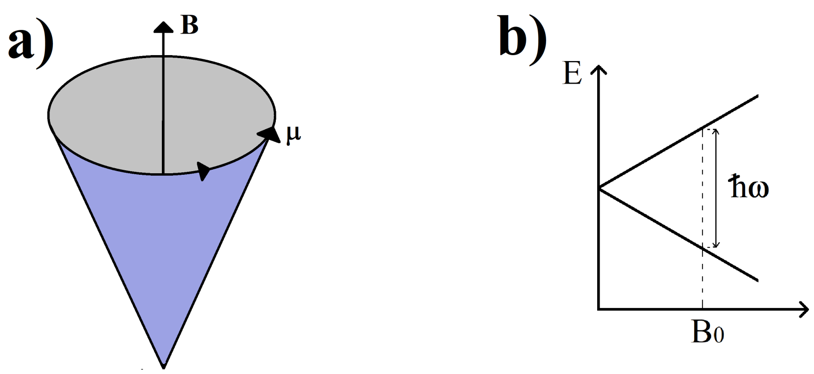

Figure 2 – a) Illustration of the precession of the electron dipole moment around a magnetic field. b) Splitting of the electron spin energy degeneracy by application of a field. The transition between the levels is realized by a photon of energy $\hbar\omega = 2\mu_B B_0$

This is called Larmor precession, and its angular frequency is given by the Larmor formula:

$$\omega_0 = \gamma B. \tag{1.16}$$

One can see that for an applied field on the order of ~ 0.1 T, the constant (1.13) gives for the electron a frequency precession on the order of ~ 3 GHz which is in the microwave range.

Applying a small magnetic field $\mathbf{B}_{AC} = be^{-i\omega t}\hat{\mathbf{x}}$ oscillating near the Larmor frequency, perpendicular to the static field, one obtains the following linear response function for small angles of precession:

$$\frac{\mu_x}{b} = \frac{\omega_0 \gamma \mu}{\omega_0^2 - \omega^2}, \tag{1.17}$$

on which one observes a resonance at ω_0. This resonance is realized experimentally and it is called Electron Spin Resonance (ESR) or Electron Paramagnetic Resonance (EPR).

Another way to understand this resonance is to start with the Zeeman energy (Equation 1.18), and realize that when an electron is subject to a magnetic field, its spin degeneracy is lifted. The transition from one level to another (Figure 2b) involves a microwave photon of frequency $2\mu_B B/\hbar$ – where μ_B is the Bohr magneton – which is the value given by Equation (1.16).

$$E = -\boldsymbol{\mu} \cdot \mathbf{B} \tag{1.18}$$

1.3.2 Magnetization Dynamics

As explained by Brown, (BROWN, 1963), the equilibrium configuration of the magnetization, reached by the minimization of the functional (Equation 1.11) with the constraint of $\mathbf{M}^2 = M_s^2$ can be seen as a problem of finding the configuration that nullifies the torque caused by an effective field $\mathbf{H}_{eff}$ in the magnetization at each point. That is, the equilibrium condition $\partial_t \mathbf{M} = 0$ in the precession equation:

$$\frac{\partial \mathbf{M}}{\partial t} = \gamma \mu_0 \mathbf{H}_{eff} \times \mathbf{M} \tag{1.19}$$

results in the parallelism: $\mathbf{M} = \lambda \mathbf{H}_{eff}$, where λ is a Lagrange multiplier of the minimization of F and the effective field is:

$$\mathbf{H}_{eff} \equiv -\frac{1}{\mu_0}\frac{\delta F}{\delta \mathbf{M}} \tag{1.20}$$

Equation 1.19 is named after Landau and Lifshitz and can be used to analyze the dynamics of magnetization that leads to ferromagnetic resonance (FMR). Another version of this equation includes phenomenologically a damping term due to Gilbert (GILBERT, 2004):

$$\frac{\partial \mathbf{M}}{\partial t} = \gamma \mu_0 \mathbf{H}_{eff} \times \mathbf{M} + \frac{\alpha}{M_s}\mathbf{M} \times \frac{\partial \mathbf{M}}{\partial t}, \tag{1.21}$$

that represents a tendency of the magnetization to curl up in the equilibrium direction due to relaxation mechanisms of the coupling of the movement with a bath of other modes. There are other types of relaxation terms more appropriate to different descriptions (REZENDE, 2020). The relaxation also implies that for the precession continue, a perpendicular pumping field needs to be added. This is analogous to the ESR case.

For a uniform precession of resonance frequency ω_0, driven by a RF field of frequency ω, the AC susceptibility tensor is calculated from (Equation 1.21) and its component in the pumping direction (REZENDE, 2020) has real and imaginary components:

$$\begin{aligned}\mathrm{Re}(\chi) &= \frac{\gamma\mu_0 M_s(\omega_0-\omega)/2}{(\omega_0-\omega)^2+(\eta/2)^2},\\ \mathrm{Im}(\chi) &= \frac{\gamma\mu_0 M_s\eta/4}{(\omega_0-\omega)^2+(\eta/2)^2},\end{aligned} \tag{1.22}$$

where $\eta \equiv 2\omega_0\alpha$. Plotting these components – corresponding respectively to the reactive and dissipative parts of the susceptibility (GIRVIN, 2019) – one obtains the Figure 3. The dissipative part is proportional to the absorbed power and the reactive to the dispersion. Ferromagnetic resonance experiments are usually performed with a phase-locked loop that measures the derivative of the absorbed power (REZENDE, 2020).

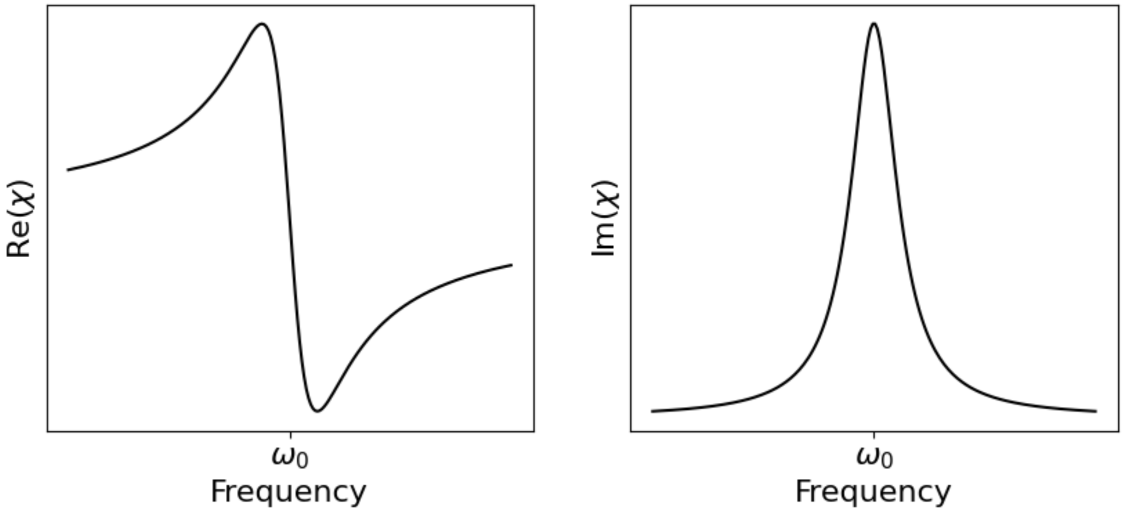

Figure 3 – Dispersive and dissipative responses of ferromagnetic resonance.

1.3.3 Kittel Formula

Writing the density of the free energy (1.11) as a function of the angles of the magnetization in spherical coordinates: $f = f(\theta(\mathbf{r},t),\varphi(\mathbf{r},t))$, Equation (1.19) holds:

$$\begin{aligned}\partial_t\theta &= \gamma H_\varphi,\\ (\partial_t\varphi)\sin\theta &= -\gamma H_\theta,\end{aligned} \tag{1.23}$$

where $H_\varphi = -\partial_\varphi f/(M\sin\theta)$ and $H_\theta = -\partial_\theta f/M$ are the spherical components of the effective field. Now, for small deviations $\delta\theta$ and $\delta\varphi$ around the equilibrium direction (θ_0,φ_0) caused by a small pumping field :

$$\begin{aligned}\partial_\varphi f &= (\partial^2_{\varphi\theta}f)\delta\theta + (\partial^2_{\varphi\varphi}f)\delta\varphi\\ \partial_\theta f &= (\partial^2_{\varphi\theta}f)\delta\varphi + (\partial^2_{\theta\theta}f)\delta\theta.\end{aligned} \tag{1.24}$$

Plugging this into Equation (1.23), one finds in first order a system of coupled linear differential equations (SLE). The *ansatz* $\delta\theta = \delta\theta_0 e^{i\omega t}$, $\delta\varphi = \delta\varphi_0 e^{i\omega t}$ leads to a system of linear equations, that has nontrivial solutions when its determinant is zero, leading to the resonant frequency:

$$\omega_0^2 = \frac{\gamma^2}{M_s^2 \sin^2\theta_0}[(\partial_\phi^2 f)(\partial_\theta^2 f) - (\partial_{\theta\phi}^2 f)^2] \tag{1.25}$$

Considering an ellipsoidal specimen, with principal axis along $\hat{x}, \hat{y}$ and $\hat{z}$, submitted to a uniform field H_0 in the $\hat{z}$ direction, the demagnetization tensor will be diagonal (Appendix A) and the uniform magnetization will nullify the exchange energy term in the free energy (1.11). If the substance if soft enough for its anisotropy be neglected, the free energy density will be in this case:

$$f = -\mu_0 M_z H_0 + \frac{\mu_0}{2}(N_x M_x^2 + N_y M_y^2 + N_z M_z^2). \tag{1.26}$$

From this density and Equation (1.25) one obtains the Kittel Resonance condition (KITTEL, 1947):

$$\omega_0^2 = \gamma^2\mu_0^2[H_0 + (N_y - N_z)M_s][H_0 + (N_x - N_z)M_s]. \tag{1.27}$$

For a sphere, the demagnetization factors are equal, and (1.27) satisfies the Larmor formula. Although the cylinder and the plane have non-uniform demagnetization fields, the degenerate cases of a very long cylinder (length >> radius) and a flat plane (radius >> thickness) can be approximated, giving the demagnetization factors of $(N_x, N_y, N_z) = (1/2, 1/2, 0)$ for the cylinder and $(N_x, N_y, N_z) = (0, 0, 1)$ for the plane, assuming the $\hat{z}$ direction is along the cylinder and parallel to the plane. Thus, for a field H_0 applied in this z direction Equation (1.27) holds the Kittel Formula for a Infinite Cylinder (1.28) and Kittel Formula for a Plane (1.29) :

$$\omega_0 = \gamma\mu_0(H_0 + M/2), \tag{1.28}$$

$$\omega_0^2 = \gamma^2\mu_0^2 H_0(H_0 + M). \tag{1.29}$$

1.4 Spin Waves and Magnons

The ground state of a spin lattice given by the ferromagnetic Hamiltonian 1.10 has all spins aligned in the same direction. The low-lying energy eigenstates are given by collective excitations involving non-localized deviations in all spins. For example, in spin 1/2 system, the first excited eigenstate is not states with one localized spin flip, as the interaction of this spin with neighbours would make this spin flip propagate through the lattice. Instead, the eigenstates are superpositions of individual spin-flips, constituting spin waves (KRANENDONK; VLECK, 1958). A semi-classical view is given considering the effective field that each spin feels due to its neighbours and also external fields: their equations of precession (Equation 1.15) are coupled and form a linear system and the system eigenmodes are precessions with a varying phase given by a certain wavelength

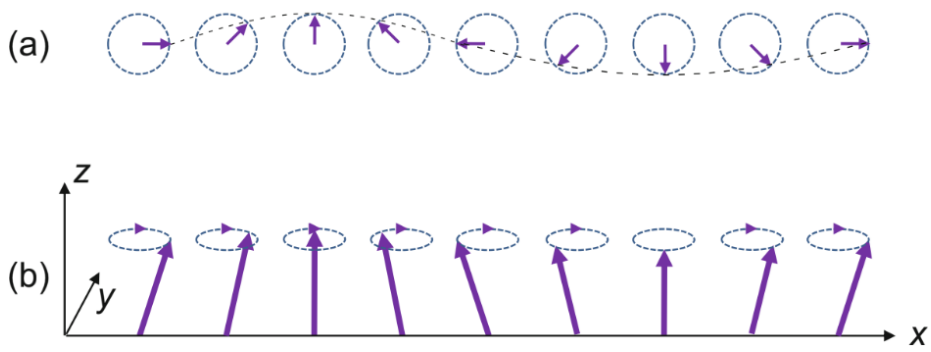

Figure 4 – Illustration of a spin wave in a linear lattice of spins. a) gives an image from above showing the different phase of precession of the spins that is shown in (b). This image was taken from (REZENDE, 2020)

(REZENDE, 2020), strongly remembering a wave (Figure 4). The picture of all spins precessing uniformly as given in the last section hence corresponds to a particular spin wave with $k = 0$. Exchange spin waves that arise from the exchange interaction have smaller wavelengths than those that arise from dipolar interaction (magnetostatic spin waves), and are usually measured in magnonics experiments.

The quantization of spin waves leads to the concept of magnons, their quantum quasiparticle. When the total spin deviation of the material is not so big (small number of magnons), the spin waves can essentially be thought of independent or not interacting, so the energy of the system is essentially the sum of the number of magnons for each mode. The Holstein-Primakoff transformation associates spin operators with bosonic operators helping the quantization of spin waves (REZENDE, 2020):

$$\begin{aligned} S_i^+ &= \hbar\sqrt{2S}\left(1 - \frac{m_i^\dagger m_i}{2S}\right)^{1/2} m_i, \\ S_i^- &= \hbar\sqrt{2S} m_i^\dagger \left(1 - \frac{m_i^\dagger m_i}{2S}\right)^{1/2}, \\ S_i^z &= \hbar(S - m_i^\dagger m_i), \end{aligned} \tag{1.30}$$

where 2S refers to the spin value and m_i are the bosonic operators associated to each site. A Fourier transformation of these operators leads to the magnonic operators $m_{\mathbf{k}}$. When the number of magnons in each site is low $\langle m_i^\dagger m_i \rangle << 2S$ the spin operators are essentially proportional to the bosonic operators and there is no interaction. The Hamiltonian is then:

$$\mathcal{H}_m = \sum_{\mathbf{k}} \hbar\omega_{\mathbf{k}} m_{\mathbf{k}}^\dagger m_{\mathbf{k}}, \tag{1.31}$$

where $\omega_{\mathbf{k}}$ is the corresponding frequency of the magnon and, given the nature of the spin waves, naturally depends on external applied fields.

1.5 Cavity Magnonics

1.5.1 Cavity-Magnon Polaritons

When an insulating magnetic material is placed in a microwave cavity, the interaction with the oscillating magnetic field can excite spin waves and ferromagnetic resonance, especially in the presence of a static magnetic field that tunes these excitations. The Hamiltonian of this coupled system is of the form:

$$\mathcal{H} = \mathcal{H}_c + \mathcal{H}_m - \int \mathbf{B} \cdot \mathbf{M} dV, \tag{1.32}$$

where $\mathcal{H}_c$ refers to the energy of the cavity, and $\mathcal{H}_m$ to the energy of the magnetic system and the Zeeman energy that realizes the interaction between the two.

A first approach to study this interaction is to consider the magnet as a macrospin $\mathbf{M} = -\gamma \mathbf{S}/V$ (SOYKAL; FLATTÉ, 2010) submitted to a uniform AC field of the cavity in the x direction and a DC field B_0 in the z direction. The Hamiltonian is then given by:

$$\mathcal{H} = \hbar\omega_c a^\dagger a + \gamma B_0 S_z + \frac{\gamma B_{ZPF}}{2}(a + a^\dagger)(S_+ + S_-). \tag{1.33}$$

Taking a perturbative approach – coupling much smaller than the energies of the individual systems alone –, the operators have in the Heisenberg picture essentially an oscillatory time dependence of $e^{\pm i\omega_e t}$ – where ω_e is the frequency of the corresponding excitation – ; the plus sign $(+)$ happens for the rising operators and the $(-)$ for the lowering. This motivates the rotating wave approximation (RWA), in which terms with fast evolution $\sim e^{\pm i(\omega_c + \omega_m)}$ are neglected close to resonance as their effects average out on the slower dynamics of interest. Doing so yields the following Hamiltonian:

$$\mathcal{H} = \hbar\omega_c a^\dagger a + \gamma B_0 S_z + \frac{\gamma B_{ZPF}}{2}(a S_+ + a^\dagger S_-). \tag{1.34}$$

Now, assuming the linear approximation, the Holstein-Primakoff transformation 1.30 for this spin gives:

$$\mathcal{H} = \hbar\omega_c a^\dagger a + \hbar\omega_m(B_0) + \hbar g(a m^\dagger + a^\dagger m), \tag{1.35}$$

where the coupling g is given by:

$$g = g_e \gamma B_{ZPF}\sqrt{N}/2, \tag{1.36}$$

where N is the number of spins.

Considering variations of the precession phase of the material, which lead to spin waves, the integral in Equation 1.32 is replaced by the sum over the interaction of individual spins in the sample, and these spins expanded in the zeroth order of the Holstein-Primakoff transformation, resulting in a sum of different magnon modes and their individual coupling with the cavity mode. The intensity of this coupling depends on the

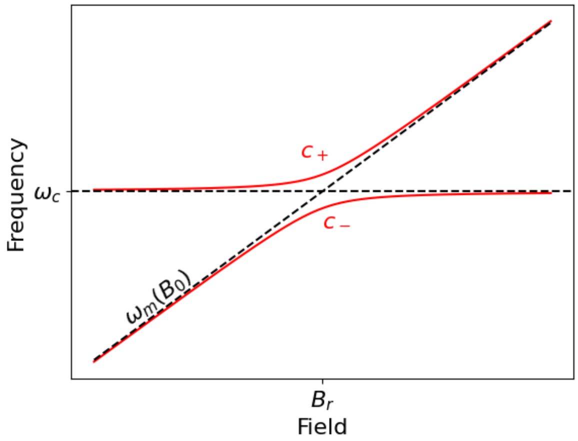

Figure 5 – Illustration of the eigenfrequencies of the coupled system as a function of an applied field that changes the frequency of the magnetic mode (detuning). Far from resonance, the two systems are essentially separated; close to resonance, they strongly hybridize, forming two polaritons, and the energy levels avoid crossing.

overlapping of the AC magnetic field and the spatial profile of the magnonic mode (AL., 2019); for a uniform field distribution, only the FMR mode survives, holding Equation (1.35), that we consider.

The Hamiltonian 1.35 is a system of two coupled quantum harmonic oscillators. As in the classic case, they have as normal modes of oscillation the symmetric and antisymmetric modes that are linear combinations of the individual motion of each resonator. The Hamiltonian in Equation (1.35) is diagonal in these two independent hybrid modes given by:

$$c_\pm = \left[ga + \left(\frac{\Delta}{2} \pm \frac{1}{2}\sqrt{\Delta^2 + 4g^2} \right) m \right] / N_\pm, \tag{1.37}$$

where $N_\pm$ are normalization constants to maintain the canonical commutation relations $[c_\pm^\dagger, c_\pm] = 1$, and $\Delta = \omega_m - \omega_c$. The corresponding eigenfrequencies are given by:

$$\omega_\pm = \omega_c + \frac{\Delta}{2} \pm \frac{1}{2}\sqrt{\Delta^2 + 4g^2}. \tag{1.38}$$

Figure 5 shows how these frequencies usually vary with the field. Far from resonance $\Delta \to +\infty$, the eigenmodes in Equation 1.37 tend to decouple $c_+ \to m$ and $c_- \to a$, as one would normally expect. Close to $\Delta = 0$, however, the hybridization is strong and the modes cannot be seen separately anymore, forming what is known as cavity-magnon polaritons. In the resonance, the polaritons are a totally symmetric/antisymmetric combination of photon and magnon modes: $c_\pm = (a \pm m)/\sqrt{2}$ and their energy separation is $2\hbar g$. This pattern of hybridization at the resonance of two interacting systems called anticrossing is very common in nature.

The coupling g, given by Equation 1.36 is proportional to the zero-point fluctuations of the field (Equation 1.9), hence, in experiments on cavity magnonics and

FMR, the magnet is usually placed in the position corresponding to maximum magnetic field of the cavity. The dependence of the coupling on the number of spins $\sqrt{N}$ also means that samples with higher spin density have stronger coupling.

1.5.2 Input-Output and Coupling Regimes

Both the cavity and the magnet interact with several other environmental systems that make them lose coherence and also eventually decay. This is summarized in their dissipation constants κ_i and η. The cavity-magnet system will also be externally driven and dissipate energy into the measurement apparatus. To analyse this open response of the cavity-magnet system, we use the input-output formalism (WALLS, 2008; RAMESHTI et al., 2022). The typical experimental situation is depicted in Figure 6, where the cavity with the magnet inside is coupled to transmission lines that send/receive signals. The transmission lines can be thought of as an ensemble of harmonic oscillators, having a continuous spectrum; the coupling of the system with this bath of oscillators makes its dynamics dissipative, but also allow for driving by signals coming down the line and, ultimately, probing of the system. The equations of motion that govern the intra-cavity field a and the magnetic mode m are a modification of the Heisenberg equations of motion that include dissipation; those are the quantum Langevin equations:

$$\dot{a}(t) = \frac{i}{\hbar}[\widetilde{\mathcal{H}}, a(t)] - \frac{\kappa}{2}a(t) - \sqrt{\kappa_{1,ex}}b_{1,in}(t) - \sqrt{\kappa_{2,ex}}b_{2,in}(t), \tag{1.39}$$

$$\dot{m}(t) = \frac{i}{\hbar}[\widetilde{\mathcal{H}}, m] - \frac{\eta}{2}m(t), \tag{1.40}$$

where $\widetilde{\mathcal{H}}$ is the Hamiltonian 1.35 in the rotating frame of the driving frequency ω, $\kappa = \kappa_{1,ex} + \kappa_{2,ex} + \kappa_i$ is the total cavity loss rate, given by the sum of the loss in the first port, the second port and internal losses, and $b_{1,in}$ and $b_{2,in}$ are the operators related to the fields that are entering the cavity by port 1 and 2. The outgoing fields of the ports are related to the other fields by the boundary condition:

$$b_{1/2,out} = b_{1/2,in} + \sqrt{\kappa_{1/2,ex}}a. \tag{1.41}$$

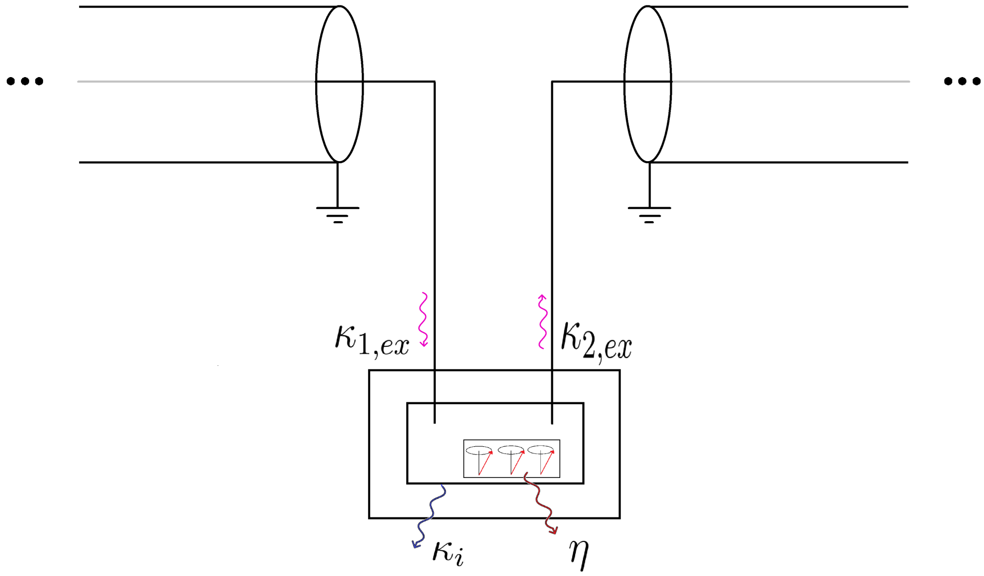

Figure 6 – Illustration of the typical experimental situation in Cavity Magnonics. A cavity with internal losses κ_i coupled to a magnet with losses η is externally coupled to an exterior measurement system by transmission lines. The coupling with ports 1 and 2 are given by $\kappa_{1,ex}$ and $\kappa_{2,ex}$.

With this, the scattering parameters $S_{i,j}$ which are measured in experiments can be calculated. In the steady regime, $\langle \dot{m} \rangle = \langle \dot{a} \rangle = 0$[1], the transmission parameter is given by:

$$S_{21} = \left(\frac{\langle b_{2,out} \rangle}{\langle b_{1,in} \rangle} \right)_{\langle b_{2,in} \rangle = 0} = \frac{\sqrt{\kappa_{1,ex}\kappa_{2,ex}}}{i(\omega - \omega_c) - \frac{\kappa}{2} + \frac{g^2}{i(\omega - \omega_m) - \eta/2}}, \tag{1.42}$$

and the reflection parameter in port 1 by:

$$S_{11} = \left(\frac{\langle b_{1,out} \rangle}{\langle b_{1,in} \rangle} \right)_{\langle b_{2,in} \rangle = 0} = 1 + \frac{\kappa_{1,ex}}{i(\omega - \omega_c) - \frac{\kappa}{2} + \frac{g^2}{i(\omega - \omega_m) - \eta/2}}. \tag{1.43}$$

The picture with dissipation provides a more complete and accurate description of experimental data. It also bridges the quantum description with the classical one. Different regimes can be realized in cavity-magnet coupling depending on the strength of the interaction relative to dissipation. The situation where $g > \eta, \kappa$ is called the strong coupling regime, where the anticrossing (Figure 5) will be clearly visible and the interaction between the magnetic system and photon coherent. This interaction was and still is extensively studied with YIG crystals (HUEBL et al., 2013; TABUCHI et al., 2014; BOVENTER, 2019), that have low dissipation rates η of few MHz.

As the dissipations increases, it becomes harder to observe signatures of coherence. For instance, the anticrossing changes and become too faint. Still, interesting features can still be observed and have been studied (ZHANG et al., 2014). In figures 7,8

[1] A more serious calculation is performed taking the Fourier transform of equations 1.39 and 1.40

and 9, numerical simulations of the transmission response 1.42 for different values of η are presented, showing the transition from the strong coupling regime to the so called Purcell regime.

The weak coupling regime given by $\eta >> g$ and $g > \kappa$ is called the Purcell regime. Only the Lorentzian of the cavity resonance can be seen (Figure 9) for all field values, with only a slight bend of its frequency and a substantial loss of quality at the resonance – hence decrease in photon lifetime, giving the name Purcell effect in analogy to the atomic physics effect. These cavity perturbation effects follow the linear response of a Lorentzian oscillator, as shown in Figure 10. This is the FMR susceptibility given by Equation 1.22 and Figure 3. The measured cavity dispersion and dissipation is given by equations 1.44 and 1.45 (ABE et al., 2011).

$$\omega_{\text{cav}} = \omega_c - \frac{g^2(\omega_m - \omega_c)}{(\omega_m - \omega_c)^2 + (\eta/2)^2} \tag{1.44}$$

$$\kappa_{\text{cav}} = \kappa_c + \frac{g^2\eta}{(\omega_m - \omega_c)^2 + (\eta/2)^2} \tag{1.45}$$

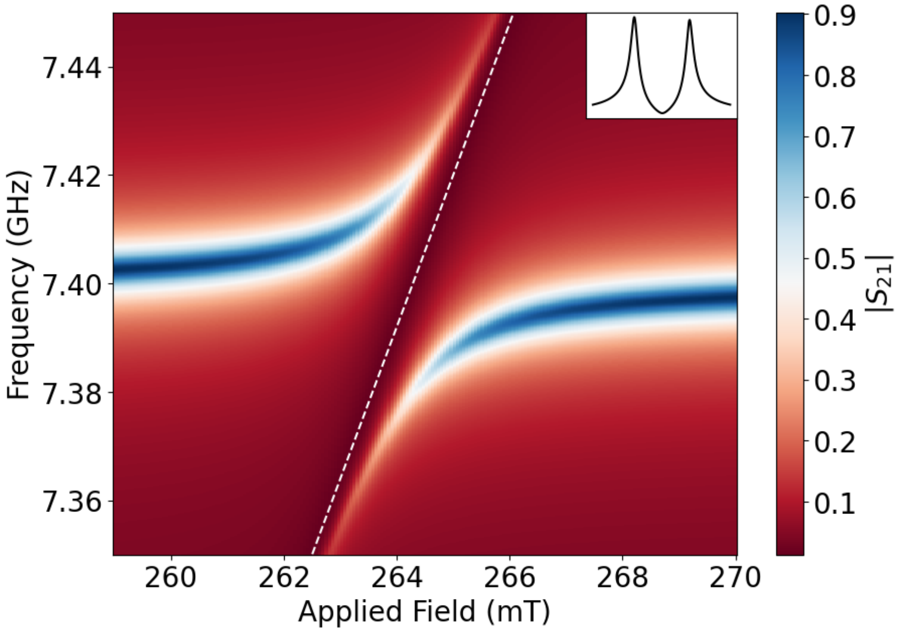

Figure 7 – Numerical simulation of the transmission given by Equation 1.42 using the parameters: $g/(2\pi) = 20\,\text{MHz}$, $\eta/(2\pi) = 5\,\text{MHz}$, $\kappa/(2\pi) = 5$ MHz, $\kappa_{1,ex} = 0.7\kappa$ and $\kappa_{2,ex} = 0.3\kappa$. The dashed white line shows $\omega_m/(2\pi) = \gamma B_0/(2\pi)$. The system is in the strong coupling regime and the anticrossing is clearly visible. The inset shows the line shape of transmission at the resonance, where the two eigenfrequencies are clearly distinguished.

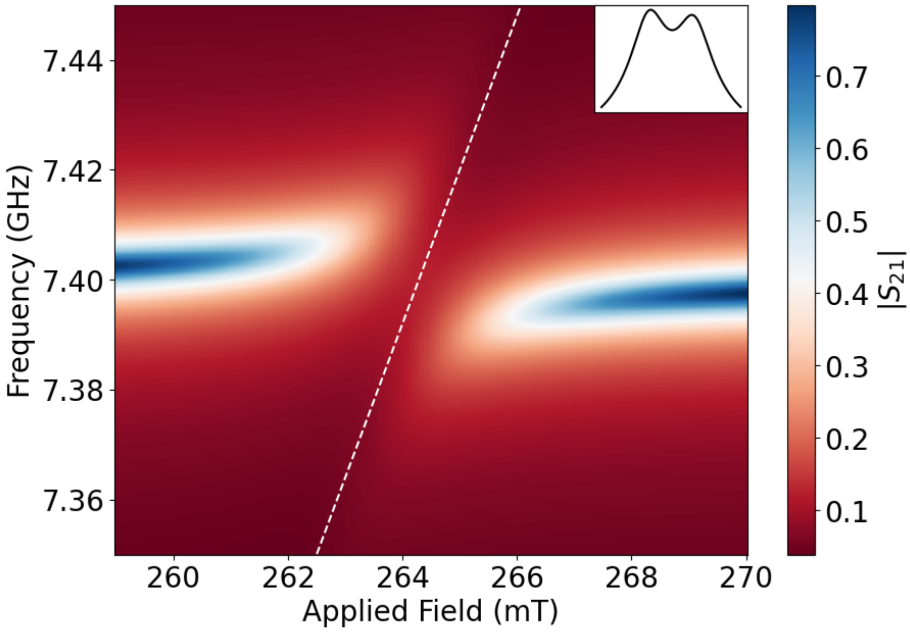

Figure 8 – Numerical simulation of the transmission given by Equation 1.42 using the same parameters as in Figure 7 but with $\eta/(2\pi) = 30\,\mathrm{MHz}$, instead. As $g > \eta$, the system is no longer on the strong coupling regime. The inset shows the line shape of transmission at the resonance, where two resonances can still be distinguished.

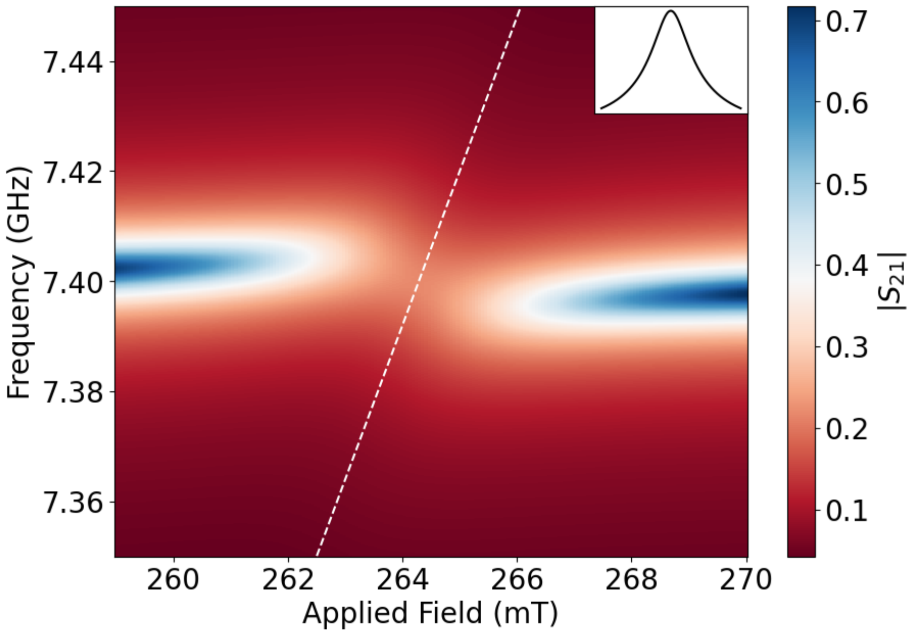

Figure 9 – Numerical simulation of the transmission given by Equation 1.42 using the same parameters as in Figure 7 but with $\eta/(2\pi) = 100\,\mathrm{MHz}$, instead. Deep into the Purcell Regime. The dashed white line shows $\omega_m/(2\pi) = \gamma B_0/(2\pi)$. The inset shows the line shape of transmission at the resonance where just a broadened cavity peak can be seen.

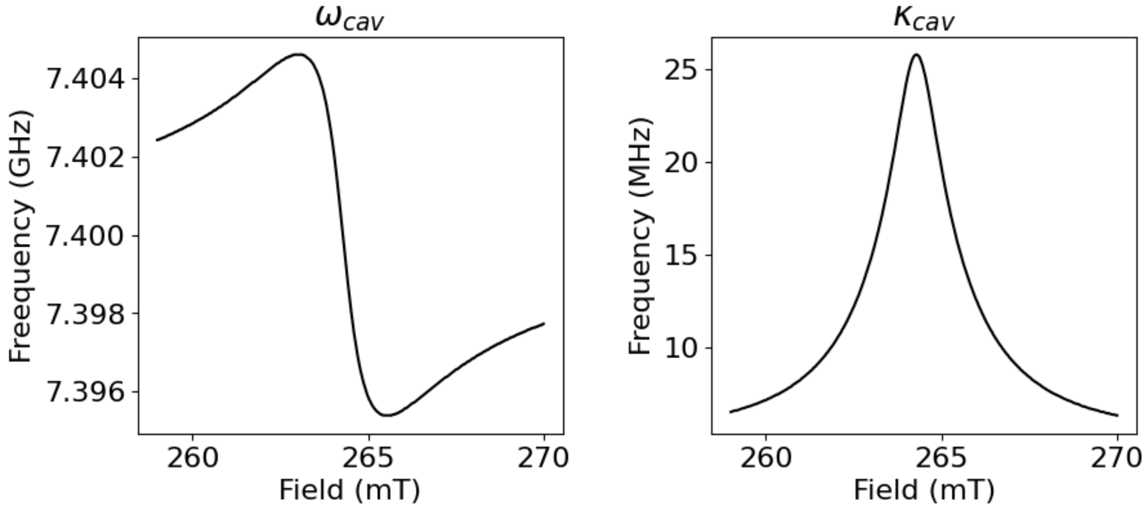

Figure 10 – Resonance frequency and widths of the peaks of the simulation with $g/(2\pi) = 20\,\mathrm{MHz}$, $\eta/(2\pi) = 100\,\mathrm{MHz}$

1.6 Ferromagnetic Resonance in Metals

The metallic character of a material imposes challenges in the description of ferromagnetic resonance due to skin effect. In a non-magnetic conductor, the current density $\mathbf{j}$ is related to the electric field by Ohm's law: $\mathbf{j} = \sigma\mathbf{E}$ that when applied to Maxwell's equations give for the fields:

$$\begin{aligned} \nabla^2\mathbf{E} &= \mu_0\epsilon_0\partial_t^2\mathbf{E} + \mu_0\sigma\partial_t\mathbf{E}, \\ \nabla^2\mathbf{B} &= \mu_0\epsilon_0\partial_t^2\mathbf{B} + \mu_0\sigma\partial_t\mathbf{B}. \end{aligned} \tag{1.46}$$

The first order time derivative introduced on these equations give rise to a damping of the waves as they penetrate the conductor, distributing them more intensely close to the surface. A plane wave solution for the electric field has the form $\mathbf{E} = \widetilde{\mathbf{E}}e^{i(kz-\omega t)}$, where the imaginary part of the propagation constants k determines the damping. The skin depth δ is then defined as the length the wave is attenuated by a factor of e^{-1}:

$$\delta \equiv \frac{1}{\mathrm{Im}(k)}. \tag{1.47}$$

The nonmagnetic skin depth for good conductors[2], $\sigma >> \omega\epsilon_0$, is given by:

$$\delta_0 = \sqrt{\frac{2\rho}{\mu_0\omega}}. \tag{1.48}$$

In a magnetic material, besides the conducting current caused by the electric field, there are the circulating currents of the quantum angular momentum of charges,

[2] Note that for $\omega \sim 10\,\mathrm{GHz}, 1/(\omega\epsilon_0) \sim 2\,\Omega\mathrm{m}$, whereas, the resistivity of most metals are in the order of $10^{-8}\,\Omega\mathrm{m}$, allowing the displacement current be neglected

summarized by the magnetization: $\mathbf{\nabla} \times \mathbf{M} = \mathbf{j_m}$. Considering the time varying parts of the fields to be represented by small letters, Maxwell's equations for a magnetic conductor gives:

$$\nabla^2\mathbf{h} - \nabla(\nabla \cdot \mathbf{h}) = \frac{2i}{\mu_0\delta_0^2}\mathbf{b}. \tag{1.49}$$

By (1.49) the field dynamics depends on the magnetization, the dynamics of which is field dependent by (1.21). Thus it is necessary to simultaneously solve both equations inside the material. In 1940 Ament and Rado (AMENT; RADO, 1955) provided a theory of ferromagnetic resonance for normal incident waves in tangentially magnetized metal planes. They noted that due to the skin effect, $\mathbf{M}$ is not uniform, causing exchange effects to be observable as a consequence of the effective field term: $\dfrac{2A}{\mu_0 M_s}\nabla^2\mathbf{m}$. The exchange field also introduces a new set of boundary conditions related to the vanishing of its total torque that are used together with the equations to solve the problem.

In a first approach, ignoring the exchange effect, considering a uniformly magnetized sample in the z direction by a static effective field H_z, one calculates from Equation 1.21 the AC susceptibility: $\mathbf{m} = \chi\mathbf{h}$ and the Polder permeability tensor $\mu = 1+\chi$ given by (KRAUS et al., 2011):

$$\mu \equiv \begin{bmatrix} \mu_1 & -i\mu' \\ i\mu' & \mu_1 \end{bmatrix} = \mu_0\mathbb{1} + \frac{\mu_0 M_s}{\left(H_z + \frac{i\alpha\omega}{\gamma\mu_0}\right)^2 - \left(\frac{\omega}{\gamma\mu_0}\right)^2} \begin{bmatrix} H_z + \dfrac{i\alpha\omega}{\gamma\mu_0} & \dfrac{-i\omega}{\gamma\mu_0} \\ \dfrac{i\omega}{\gamma\mu_0} & H_z + \dfrac{i\alpha\omega}{\gamma\mu_0} \end{bmatrix}. \tag{1.50}$$

Now substituting $\mathbf{b} = \mu\mathbf{h}$ in Equation 1.49, assuming a plane wave incident perpendicular to the plane, one gets an SLE, whose vanishing determinant gives the propagation constant of the wave inside the material:

$$k^2 = -\frac{2i}{\delta_0^2}\frac{\mu_{eff}}{\mu_0}, \tag{1.51}$$

where the effective permeability is given by:

$$\mu_{eff} = \frac{\mu_1^2 - \mu'^2}{\mu'} \tag{1.52}$$

The interaction with the spins changes the wavelength and the skin depth, which now presents a minimum at the resonance, as shown in a numerical calculation of Figure 18. This resonance frequency remains the one given by Kittel formula (1.29).

When the exchange interaction is taken into account and the effective field $2A/(\mu_0 M_s)\nabla^2\mathbf{m}$ added, the resultant SLE will lead to a secular cubic equation for k^2. Thus for a given direction of propagation, there will be three roots (wave branches); one of which is a long-wavelength excitation, with similar features to the solution with $A = 0$, where the imaginary part is a maximum at the resonance (minimum of skin depth), and the other two are related to spin waves and may lead to spin wave resonances (KRAUS, 1982; LIU; BARKER, 1975).

1.7 Theory of Ferromagnetic Resonance in Metallic Wires

The theory of ferromagnetic resonance in metallic micro- and nanowires was extensively investigated and reviewed by Kraus (KRAUS et al., 2011; KRAUS, 1982). The situation considered here is a wire magnetized along its axis (z direction) and subjected to transverse microwaves that add a time varying part $\mathbf{m}$ to the magnetization. Due to the geometry, this time-varying part is decomposed into cylindrical waves (Equation 1.53) – where the z dependence is ignored assuming a small wire in comparison to the radiation wavelength. The absorption of energy is related to the real part of the surface impedance, but also, for longer wires, to scattering moments (see Appendix B). Overall the excitation of each azimuthal mode of ac magnetization will depend on the symmetry of the incident radiation, making their response sensitive to the measuring circuit/setup. The modes that are generally excited are $n = 0$ and $n = 1$. Figure 11 illustrates the spatial distribution of ac magnetization for these modes. Mode $n = 0$ is circularly symmetric and couples with circular ac magnetic fields, like the ones produced by axial currents; while $n = 1$ has a dipolar character and couples with a perpendicular field on the wire.

$$\mathbf{m}(r, \phi, t) = e^{i\omega t} \sum_n \mathbf{m}_n e^{in\phi} J_n(kr) \tag{1.53}$$

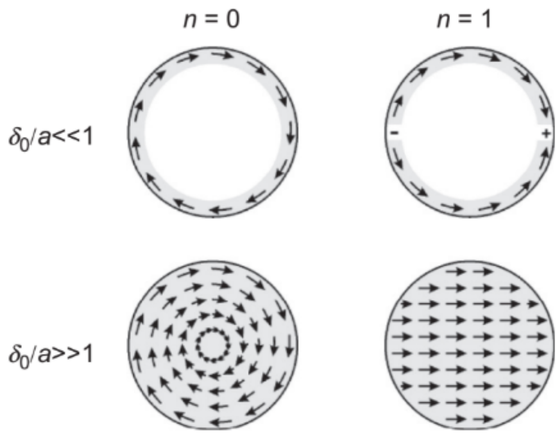

Figure 11 – Illustration of the ac magnetization modes $n = 0$ and $n = 1$ for two limits of the ratio δ_0/R. When the skin depth is much smaller than the radius, the resonance happens only at a thin shell of wire; in the other case, the resonance happens throughout the entire wire and the dipolar mode $n = 1$ have its resonance condition shifted from Kittel Plane (Equation 1.29) to Kittel Cylinder (Equation 1.28) (see Appendix B). This image is from Kraus (KRAUS, 2015)

Substituting this cylindrical decomposition into Maxwell's and Landau's equations, as in the planar case, the propagation constant k is given by Equation 1.51 when $A \to 0$, and by the bicubic equation otherwise. Considering the former case, and writing the susceptibility in the circularly polarized base: $\mu_\pm = \mu_1 \mp \mu'$, the surface impedance for each mode n is given by (KRAUS et al., 2011):

$$\eta_n = \frac{e_{n,z}(r=R)}{h_{n,\phi}(r=R)} = \rho \frac{2kJ_n(kR)}{\mu_{eff}[J_{n+1}(kR)/\mu_+ - J_{n-1}(kR)/\mu_-]}, \tag{1.54}$$

where R is the radius of the wire, ρ its resistivity. The surface impedance for the case considering exchange is given by Equation B.1 in the Appendix. For $n = 0$, the surface impedance 1.54 reduces to:

$$\eta_0 = \rho k \frac{J_0(kR)}{J_1(kR)}, \tag{1.55}$$

that is the formula for the giant magneto impedance effect (CHRISCHON, 2012).

When the skin depth is much less than the radius of the cylinder, $|kR| >> 1$, the wave is restricted to a small layer close to the surface, that unrolled is equivalent to a planar surface (Figure 12), thus the situation is the same as in the last section and the resonance frequency is given by Kittel's Formula 1.29. For wires of smaller radii $R \sim \delta$, the curvature becomes important; the response broadens and becomes asymmetric. As $R >> \delta$ the resonance condition for the dipolar mode shifts to the uniform magnetized cylinder Kittel condition (Equation 1.28) as expected in this regime, but the mode $n = 0$ keeps the Kittel plane condition (besides shifts due to exchange effect) and actually presents anti-absorbance or transparency at the resonance. These regimes are explored by Kraus ((KRAUS et al., 2011)) and we reproduce his calculations and example in the Appendix B.

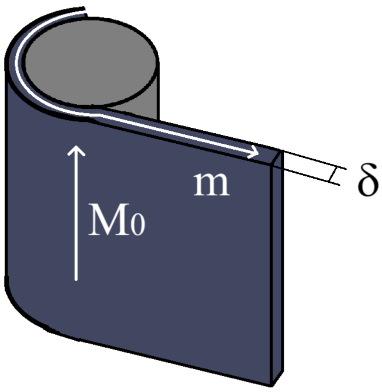

Figure 12 – Illustration of an axially magnetized cylinder with a time varying magnetization at a shell (given by the skin depth) close to the surface. The topology is the same as ferromagnetic resonance in a tangentially magnetized plane, being given by Kittel Plane resonance condition (Equation 1.29)

As it was mentioned the symmetry of mode $n = 0$ couple it strongly with axial currents on the wire. This can be performed by placing the wire as part of centre conductor of a transmission line or by placing it along the rf electric field of a 3D cavity, working as an antenna. Rodbell reported ferromagnetic resonance in Iron Whiskers using this last method (RODBELL, 1959a). He also reported in another paper (RODBELL, 1959b) that this absorption could be orders of magnitude higher than the conventional measurement setup. This makes mode $n = 0$ dominant in almost all experimental situations and mode $n = 1$ relevant only at the node of the electric field (KRAUS et al., 2011). We follow other authors and call the wire positioned at the electric anti-node of the cavity Rodbell configuration.

It is hard to determine precisely the value of magnetic field achievable by this electrically driven resonance, and it would require one to know the value of electric field inside the wire. That probably depends on the wire geometry and the frequency of the wave. Here I present an argument that the induced magnetic field in the wire at Rodbell position of a rectangular cavity have a higher value than the maximum magnetic field of the unperturbed cavity. The most important assumption is that the electric field on the surface of the wire is on the order or bigger than the unperturbed field intensity e_y at this position. The induced curled magnetic field at the surface is, by Ampère law, then :

$$h_{in} > \frac{1}{2\pi\rho R}\int e_{y0}e^{-r/\delta}dS, \tag{1.56}$$

where the integration is taken on the cross section of the wire, and the exponential factor gives the decaying of the skin effect. Assuming $R >> \delta$, this leads to:

$$h_{in} > \frac{\delta^2}{\rho R}e_{y0}. \tag{1.57}$$

Now, the field e_{y0} at the cavity anti-node for mode TE_{101} is related to the field h_{z0} of the cavity node by (POZAR, 2012):

$$h_{z0} = \frac{\pi e_{y0}}{k\sqrt{\mu_0/\epsilon_0}L_x}, \tag{1.58}$$

thus:

$$\frac{h_{in}}{h_{z_0}} > \frac{L_x}{R}, \tag{1.59}$$

which is easily on the order of 10^3. Of course, the first assumption of the intensity of the field on the wire is dubious, but even if not true, and e_y is smaller by some factor, the size ratio will likely still be strong enough to ensure the higher value of the induced field, as this is shown in several experiments, including this thesis.

2 CoFeSiB Microwire

This chapter presents the microwires studied. These wires have been extensively studied because of their magnetic properties, such as magnetic softness, a pronounced Barkhausen effect, and giant magnetoimpedance (GMI), which enable potential applications. The vast body of literature on magnetic amorphous microwires cannot be fully reviewed or discussed here. Instead, this chapter provides a brief overview, accompanied by images and measurements that offer relevant information about the material.

2.1 Introduction

The magnetic system studied in this dissertation consists of glass-covered amorphous microwires with a nominal composition of $Co_{68.15}Fe_{4.35}Si_{12.5}B_{15}$. These microwires have an overall diameter of approximately 16 µm and an inner metal core of 8 µm. They were manufactured by Manuel Vázquez's group at ICMM/CSIC in Madrid, Spain, and provided through a collaboration with the institute's Materials and Low-Temperature Laboratory (LMBT). Glass-covered microwires are produced by rapid cooling of molten metal while it is continuously drawn with softened glass, forming a long strand of wire. This process is known as Taylor-Ulytowsky (TAYLOR, 1924; ZHUKOVA et al., 2022). The amorphous structure results in a higher fracture strength and exhibits notable soft magnetic properties (CHIRIAC; ÓVáRI, 1996).

2.2 Material Handling and Microscopy

Depending on the surface they are placed on, the wires are generally visible to the naked eye due to light scattering on their surface, which gives them a gray or slightly shiny appearance, depending on the angle and lighting. For handling purposes, a blank white sheet of paper was usually used as a surface. This not only enhanced their visibility but also made it easier to spot "runaway" pieces. Due to their small size and light weight, the wires can become electrostatically – and sometimes magnetically – attached to various surfaces, making it important to keep track of all pieces to avoid contamination. Although the amorphous nature of the metallic core provides higher fracture strength and the glass coating adds mechanical robustness and some flexibility, the microwires are still delicate and can break easily. Care must be taken handling them. Luckily, as they are produced in long strands, plenty of material was available.

Figure 13 shows an image of the microwires taken with an optical microscope. On the left, the metallic core is visible shining through the glass cover. On the right, where

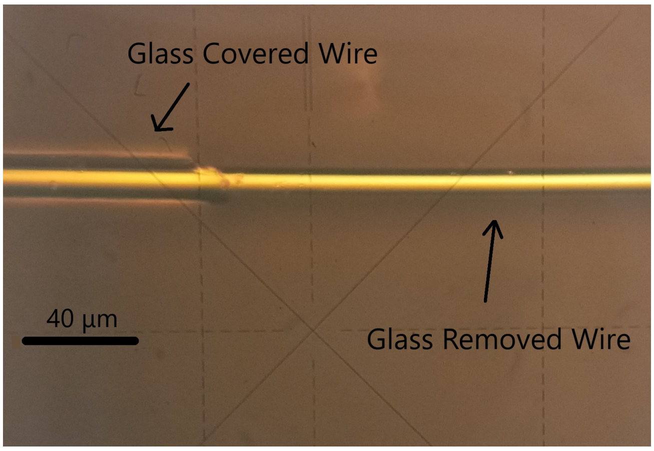

Figure 13 – Microscope image of a wire. On the right side, the wire had the glass coating removed as evidenced by the absence of glass distortion

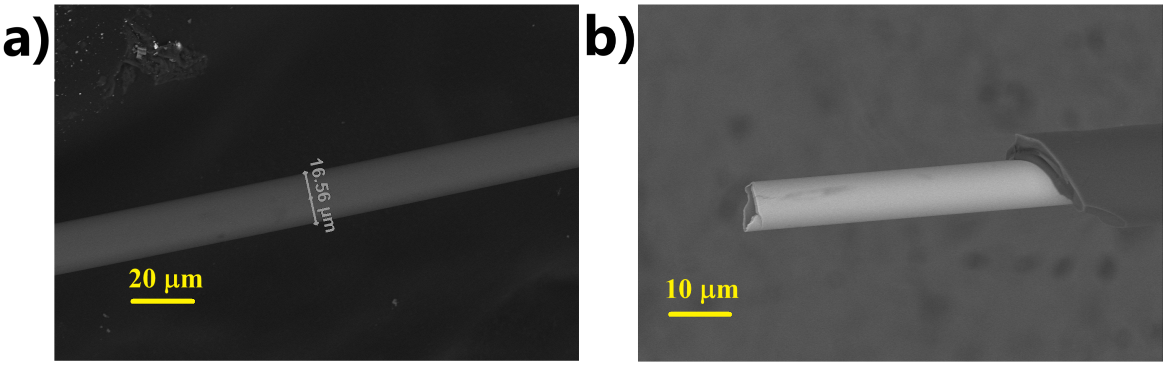

Figure 14 – FEG-SEM images of a piece of wire made at the chemistry institute (IQ). An accelerating voltage of 10 kV was used. (a) Image of the glass covered wire and measured diameter. (b) Image of the tip of the wire showing the metal exposed. It is brighter than the glass as it does not get charged with the electrons of the microscope.

the glass was mechanically removed by shattering of the glass and gently brushing it with a scalpel, the bare metal is visible. Figure 14 presents two Scanning Electron Microscopy (SEM) images of the wires; the measured diameter of the microwire with the glass sleeve is 17 µm and the diameter of the metallic core is 8 µm. In Figure 14 (a), we present the micrography of the wire covered with glass and in Figure 14(b), the metallic core and the glass cover. The apparent hollowness observed on the tip of the wire in the Figure 14(b), is probably due to how the wire was cut.

To further investigate the morphology of the microwires, Figure 15 presents SEM images of vertical cross-sections of a couple of wires prepared using Focused Ion Beam (FIB) and platinum deposition. Figure 15(a) shows a metal disk cut from the wire, where platinum was deposited on top to increase contrast. Carbon paint was applied to secure the microwires onto the aluminum stub and so it is present around all samples. Figure 15(b) presents a piece of wire cut exposing the metallic inner core surrounded by

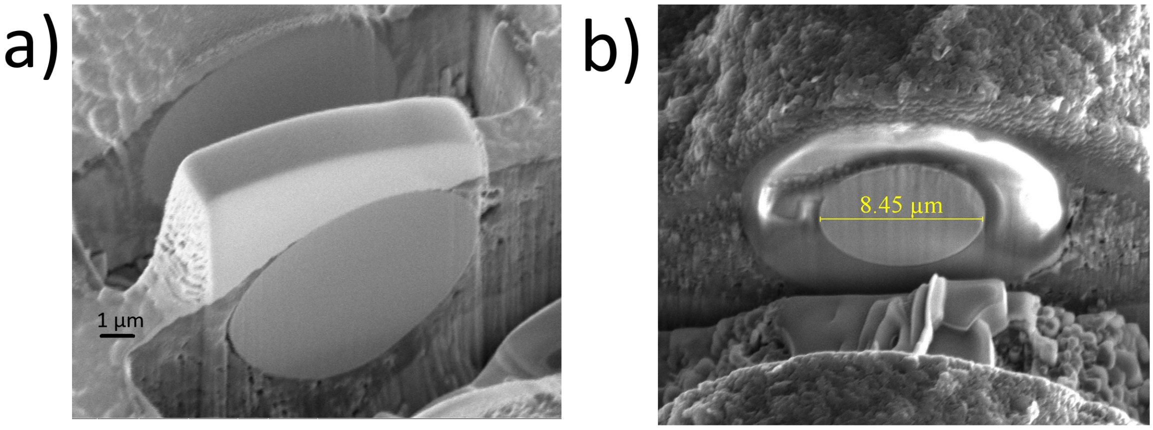

Figure 15 – FEG-SEM images of two wires cut with FIB. They were made on the Dual Beam FIB-SEM of the center of semiconductors and nanotechnology at Unicamp (CCSnano). Tilt Angle: 30°. (a) A piece of a wire without glass (grey cylinder) immersed in carbon cut from both sides forming a disk. Platinum (in bright, above the disk) was deposited on top to increase contrast. (b) Cross section of a wire immersed in carbon that was cut exposing the metal core with 8.5 µm of diameter surrounded by the glass cover.

Metal		Glass	
Element	Atomic Percentage (%)	Element	Atomic Percentage (%)
Co	81	Si	25
Fe	5	O	75
Si	11		
B	3		

Table 1 – Atomic composition of the metal and the glass of the wires obtained from an EDS measurement

the glass sleeve. These images of the cross-section confirm that they are solid cylinders[1].

An EDS map was obtained (Figure 16) to analyse the elemental composition of the metallic core, confirming the presence of the expected elements: Co, Fe, Si and B. Table 1 summarizes the EDS results for both the metallic core and the glass. The atomic percentages, however, deviate from the nominal composition. A possible explanation for this is the difficulty of EDS to accurately detect elements with low atomic number, like boron, giving a wrong percentage composition. Variations in the composition of the material are also possible. The composition of the glass cladding was also analysed.

2.3 Magnetic and Electric Properties

A Lakeshore Vibrating Sample Magnetometer was used to measure the room-temperature M-H curve of a microwire sample. The wire was oriented parallel to the

[1] We performed the FIB due to the suspicion of hollowness observed from the microscopy of Figure 14b. But thankfully this was not the case.

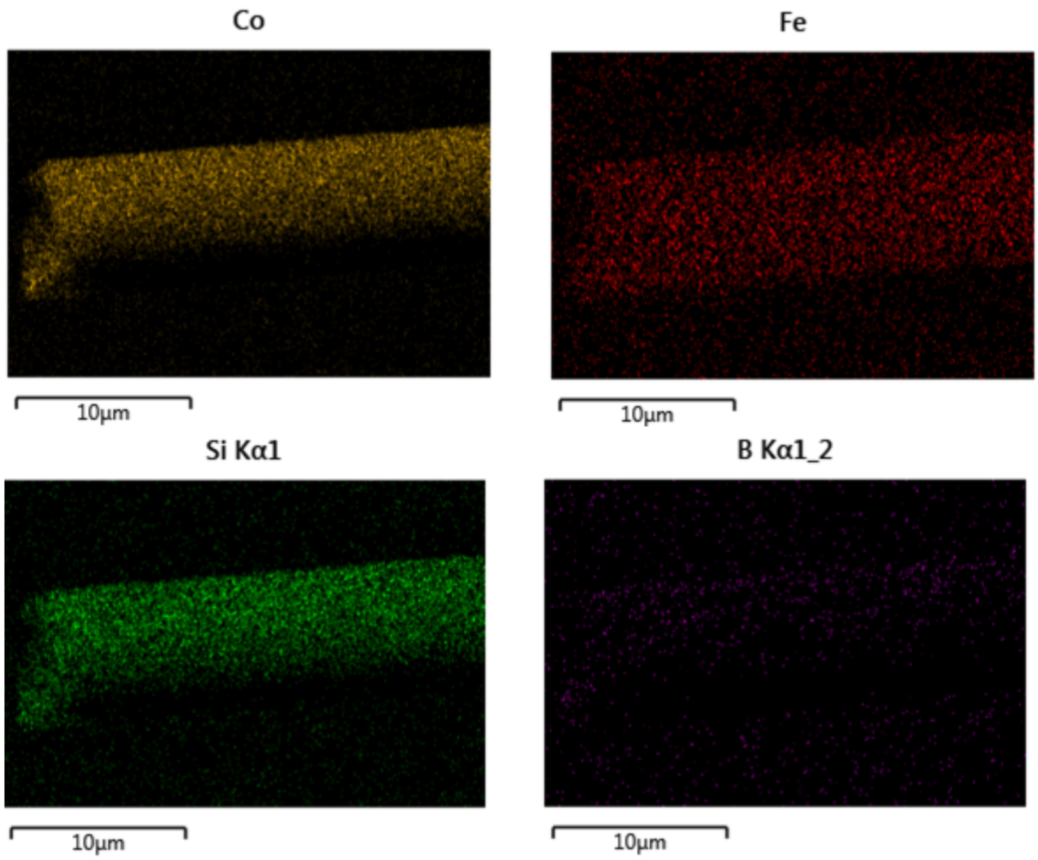

Figure 16 – EDS map of the exposed metal part of a CoFeSiB wire indicating the presence of the elements in the composition: Cobalt in yellow, iron in red, silicon in green and boron in purple. The boron signal is very weak and only slightly bigger than the background

applied field and glued onto the VSM quartz rod with silicone wax. Figure 17 shows the obtained hysteresis curve. The microwires exhibit great magnetic softness, having a coercive field of a few 10^{-4} T. Additionally, the hysteresis curve does not fully close, as observed by comparing the initial magnetization value (indicated by the orange dot in Figure 17) with the final magnetization value. This could be an effect of the field sweeping too fast. The noise is due to a bad setting of the sensor sensitivity. There could also be dielectric effects of the glass.

The saturation magnetization of the wire was calculated by dividing the measured moment by the estimated mean volume. The measured piece was 5 mm long, yielding an estimated volume of $(2.6 \pm 0.3) \times 10^{-7}\,\mathrm{cm}^3$. The primary sources of uncertainty are the length measurement and possible variations in the wire diameter. Assuming a linear approach to magnetization saturation as a function of 1/H, a value of $\mu_0 M_s = (0.8 \pm 0.1)\,\mathrm{T}$ was estimated. This result aligns with the literature value of 0.85 T reported by Chiriac et al. (CHIRIAC et al., 1999) and agrees well with the experimental data presented in subsequent sections. However, the uncertainty in volume estimation and noise observed in the hysteresis measurements limit the overall precision of this value. The estimated spin density for this material considering its magnetization to be 0.85 T is $\sim 7.3 \times 10^{22}\,\mathrm{cm}^{-3}$

The magnetic structure of glass-covered amorphous microwires strongly depends on internal stresses and the sign of the magnetostriction constant, as the absence of crystalline anisotropy makes the magnetoelastic term a significant factor in their magnetic free energy (CHIRIAC; ÓVáRI, 1996). There are essentially three main sources of stresses during wire formation: solidification of the metal core, differences in thermal expansion coefficients between the metal and glass, and the tensile drawing stress applied during wire forming.

Calculations of these stresses performed by (CHIRIAC; ÓVáRI, 1996) predict that microwires with negative magnetostrion constant, such as $Co_{68.15}Fe_{4.35}Si_{12.5}B_{15}$, exhibit an axially oriented magnetic domain inner core and large circularly oriented outer domains. This structure leads to a smoother change in axial magnetization, as observed in Figure 17. Applied stresses and thermal treatment can alter these domain structures changing their RF response at low fields as observed in Giant Magnetoimpedance experiments (PIROTA et al., 2000). The DC fields applied in our studies of ferromagnetic resonance are much higher than the coercive field of the wires, so we ignore anisotropy effects and always assume the wire is uniformly magnetized along its axis at saturation.

Regarding their electrical properties, the metallic core of the wire makes the skin effect important in their FMR behaviour as described in Section 1.7. Their resistivity is on the order of thousands of nΩ, and we use $1100\,\mathrm{n\Omega m}$ (CHIRIAC; ÓVáRI, 1996) as a reference. This gives for the applied frequencies $\sim 7\,\mathrm{GHz}$ a nonmagnetic skin depth of $\sim 6\,\mu\mathrm{m}$, that is in the order of the wire radius. In Figure 18, the skin depth based on Equation 1.51 for the typical wire parameters and a frequency of 7.2 GHz is plotted.

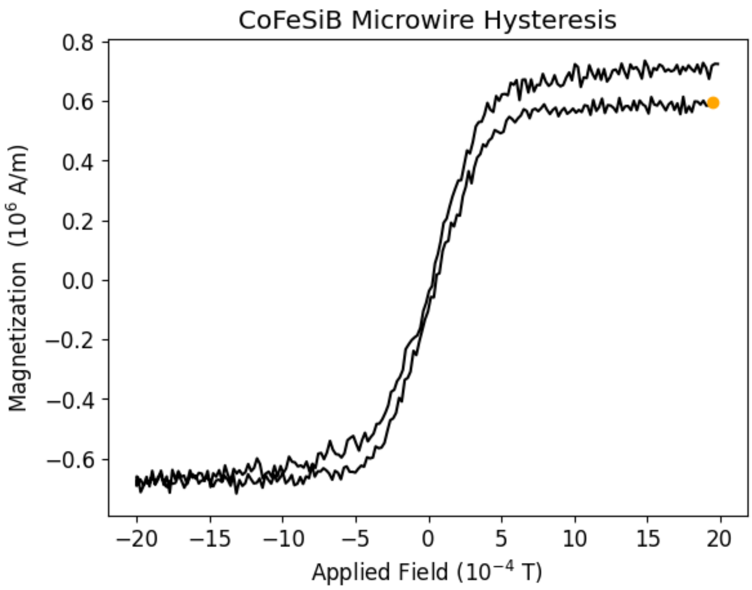

Figure 17 – 300 K M-H curve of the $Co_{68.15}Fe_{4.35}Si_{12.5}B_{15}$ microwire measured by VSM. The magnetization was obtained by dividing the measured moment by the calculated volume of $(2.6 \pm 0.3) \times 10^{-7}\,\mathrm{cm}^3$. The orange dot indicates the starting point of the curve, where the magnetization was saturated. Probable ionization of the air around the sample caused the curve to not close.

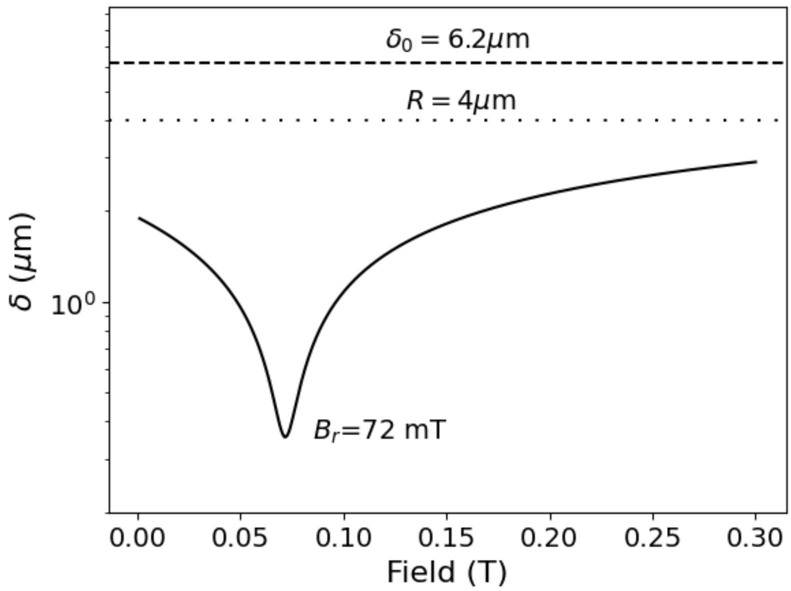

Figure 18 – Magnetic skin depth as a function of the field for a frequency $\omega/(2\pi) = 7.2$ GHz, $\rho = 11 \times 10^{-7}\,\Omega\mathrm{m}$ and $\mu_0 M_s = 0.85\,\mathrm{T}$, $\alpha = 0.02$. The resonance field B_r is calculated by the Kittel formula for this frequency. The dashed line is the value of the nonmagnetic skin depth.

3 Experimental Apparatus

This chapter presents the experimental setup used in the FMR measurements of the next chapter and explains some of their working principles.

3.1 Vector Network Analyser

When dealing with a system composed of several passive and active microwave components, most of the time the interest lies only on a few parameters which determines the engineering properties of system, without the need to solve the whole electromagnetic field problem. A set of parameters of this kind are the scattering parameters S_{ij} of a component. The device is regarded as a linear black box connected in multiple ports, through which RF signals can flow. The scattering parameters S_{ij} are then defined (POZAR, 2012) as the ratio of the voltage[1] reflected at port i to the voltage incident on port j, when the incident voltages on the other ports are zero (match terminated):

$$S_{ij} = \left.\frac{V_i^-}{V_j^+}\right|_{V_k^+=0, k\neq j}, \tag{3.1}$$

thus determining a scattering matrix of the device. Diagonal terms represent reflection coefficients at each port and the off-diagonal terms represent the different relative transmission coefficients. For a two port system, with an excitation on the port 1, the reflection and transmission parameters correspond respectively to S_{11} and S_{21}. As waves are being considered, the scattering parameters are actually complex, having a magnitude and a phase. The first describes the relation between the amplitudes of the waves, and the second, phase shifts. In this work, when the magnitude is referred in dB units, it is calculated by the usual expression:

$$|S_{ij}|^2 \ \ (\mathrm{dB}) = 20 \log_{10} |S_{ij}|. \tag{3.2}$$

The Vector Network Analyzer (VNA) is an instrument capable of measuring the scattering parameters of a device. Figure 19 shows a schematic exhibiting the working principles of this equipment (POZAR, 2012). It has a controllable RF generator which sends a signal to a reference line and to a directional coupler that is connected to one of the ports. The directional coupler is a component that is built so that signals coming back the line are coupled to the second line, thus allowing the analysis of reflected signals. The ports are connected to coaxial cables that connect to the device under test (DUT). A switch can change the excitation from the first port to the second. The signals are

[1] In (POZAR, 2012) the concept of voltage for a electromagnetic wave or a voltage wave is discussed. The scattering parameters can also be defined in terms of so called power waves.

sent to a heterodyne system, where mixers multiply them by a fixed-frequency RF signal, called the local oscillator (LO) to produce intermediate frequency (IF) waves through downconversion. These IF signals are easier to process electronically as they have lower frequency. After passing through a filter, they are digitized and processed by a computer.

In a typical measurement using the VNA, the frequency range is selected along with the number of points, the IF bandwidth, the RF power and the measurement type to be performed. The frequency is sweeped and the parameter measured. For absolute measurements, the VNA must be calibrated to account for impedance mismatches and phase shifts caused by connectors and coaxial cables. In this work, two VNAs were used, a E8362C by Agilent Technologies, for the room temperature measurements and a E5063A from Keysight, for the cryogenic measurements. Two different VNAs were used simply because they are from different labs.

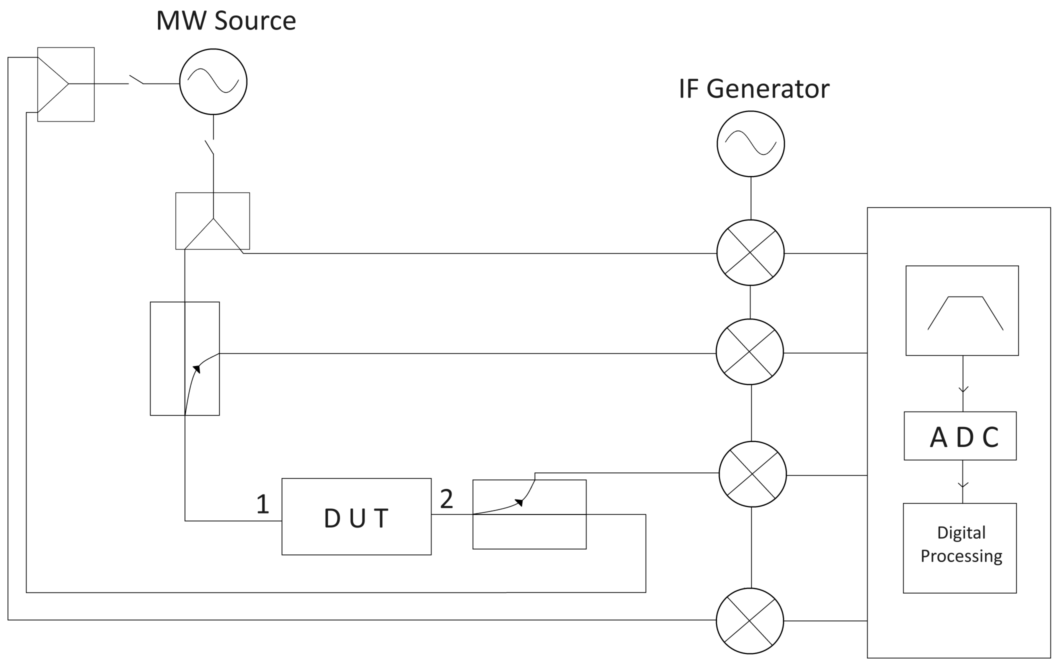

Figure 19 – Schematic of the working principles of a VNA

3.2 Cavity VNA-FMR Setup

The schematic of the experimental apparatus used for the room temperature VNA ferromagnetic resonances is presented in Figure 20b. It consists of a microwave cavity connected to a VNA submitted to the field of a Helmholtz coil that is fed by a current source. A hall probe is used to measure the intensity of the field on the region of the cavity. Figure 20a shows a photo of the setup. The RF magnetic field of the cavity is oriented in the x direction of the cavity and the static field in the y direction. The gaussimeter, VNA and power supply communicated through a IEEE488 bus (GPIB) with a computer where a GPIB-USB-HS adapter was used with the correct drivers. The communication then is followed by the VISA protocol using as a wrapper the Python package PyVISA. In this way, the measurement is automated following a Python program that is presented in Appendix D.

Usually VNA-FMR are performed using broadband microstrip or coplanar waveguides (CPW) (KRAUS, 2015), while 3D cavity VNA is commonly performed in measuring circuits that includes a phase-locked loop. We use the high quality of our cavity and the sensitivity of the VNA to measure the absorption directly, in a Cavity-VNA setup (LO; LAI; CHENG, 2011). We vary both the applied magnetic field and the frequency, allowing us to take a map. These measurements are of the same type as those performed in other Cavity Magnonics experiments (TABUCHI et al., 2014; ZHANG et al., 2014).

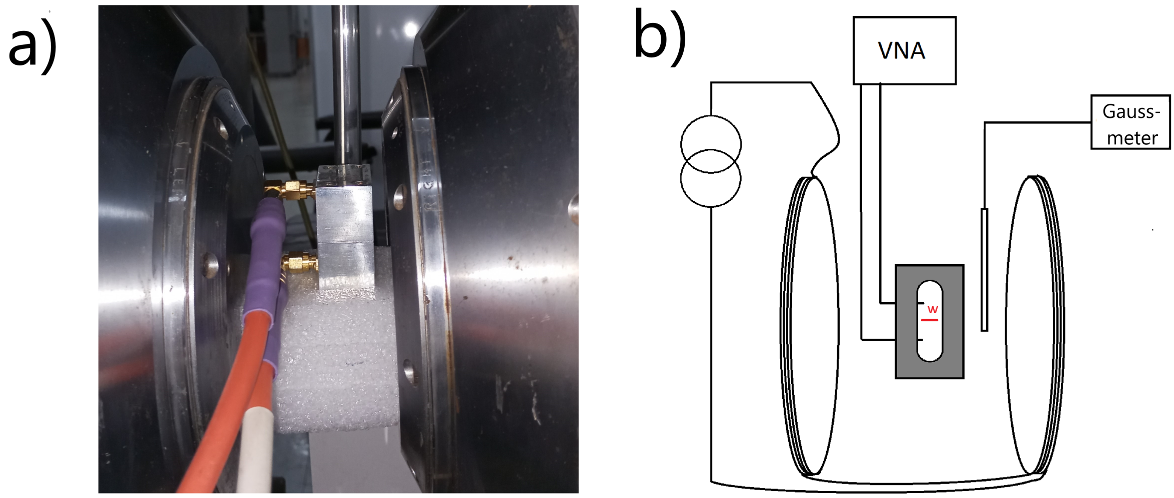

Figure 20 – a) Photo of the measurement setup. The cavity connected to the VNA via the coaxial cables is placed above a foam that is hold by the two poles of the coil. The hall probe can be seen behint it. b) Schematic of the setup

3.3 Cryogenic Setup

3.3.1 Dilution Refrigerator and Superconducting Magnet

To cool the samples down to 7 mK, a commercial *Blue Fors* XLD dry dilution refrigerator was used (Figure 22a). A dilution refrigerator (DR) is a closed-cycle cryogenic system designed to provide continuous cooling below 1 K. It works based on the heat of mixing of ^{3}He and ^{4}He. Below the temperature of 0.87 K the mixture of ^{3}He and ^{4}He separates into two phases of different concentrations; at 0 K, the concentrated phase becomes pure ^{3}He, but the dilute one remains with 6.6% of ^{4}He (POBELL, 2007). This finite solubility allows for cooling at very low temperatures, until few mK. Basically, cooled ^{3}He is pumped into a chamber (mixing chamber) that contains the mixture, with ^{3}He

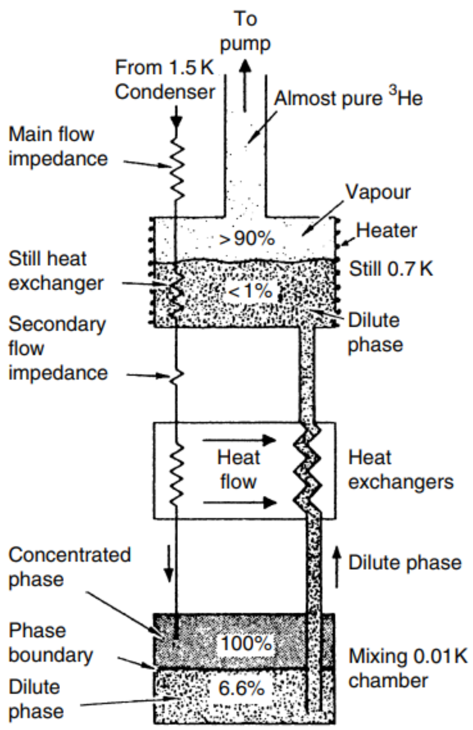

Figure 21 – schematic of the lowest stage of a dilution refrigerator, where the cooling to mK happens. Image from Pobell (POBELL, 2007)

floating on top of the dilute phase. A wide pipe (Figure 21) that goes into the dilute phase connect it with the Still that is kept at 0.7 K by a heater and evaporates ^{3}He that is continuously pumped, resulting in an osmotic pressure that keeps the flow of ^{3}He and its crossing at the interphase boundary (dilution). This mixing is an endothermic process that is responsible for the cooling down to temperatures of mK with a cooling power of hundredths of μW.

A superconducting coil by *American Magnetics* designed to be used with our dilution refrigerator was used to supply the static magnetic field to the sample. At low temperatures the generation of magnetic field by current has to be done by superconducting lines, as ohmic dissipation would heat the system. This also allows for the production of strong magnetic fields. Our commercial coil can produce fields up to 8 T, with a control of 5×10^{-4} T or less depending on the stability. The field is produced in the upward direction along the DR and the coil is thermally anchored on the 4 K stage (Figures 23a,b). The coil wires connect at the exterior with the current leads that are fed by a quadrupolar power supply which by itself is controlled by the power supply programmer. From this programmer, one can set field targets, ramp rates, give a start and a pause, among other things. The programmer was connected via ethernet to a network switch, along with other instruments, so that they comunicate with a computer. Using the *socket* library in python, a connection is established with a python script to control the magnet. The program that was written to control it is presented in Appendix E.

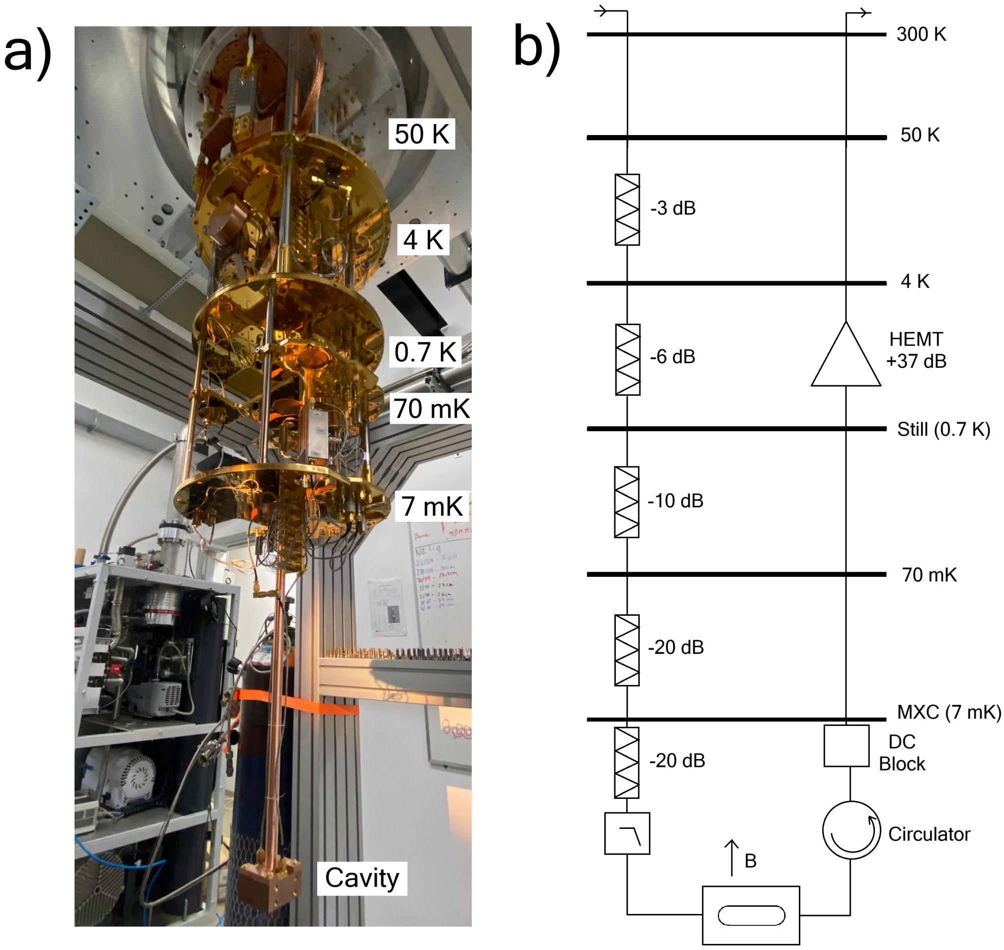

Figure 22 – a) Image of the open dilution refrigerator. The different temperature stages are marked. The cavity is anchored at the 7 mK stage with the sample holder built to be positioned at centre of the magnetic field of the superconducting coil. b) Schematic of the microwave circuit of the dilution refrigerator that the sample was connected with. Descending from the room temperature the microwave signals are attenuated until they reach the lowest stage. After passing through the sample it comes back from a circulator that prevents noise from the upper stages to heat the mK stage, it is amplified a goes out the DR.

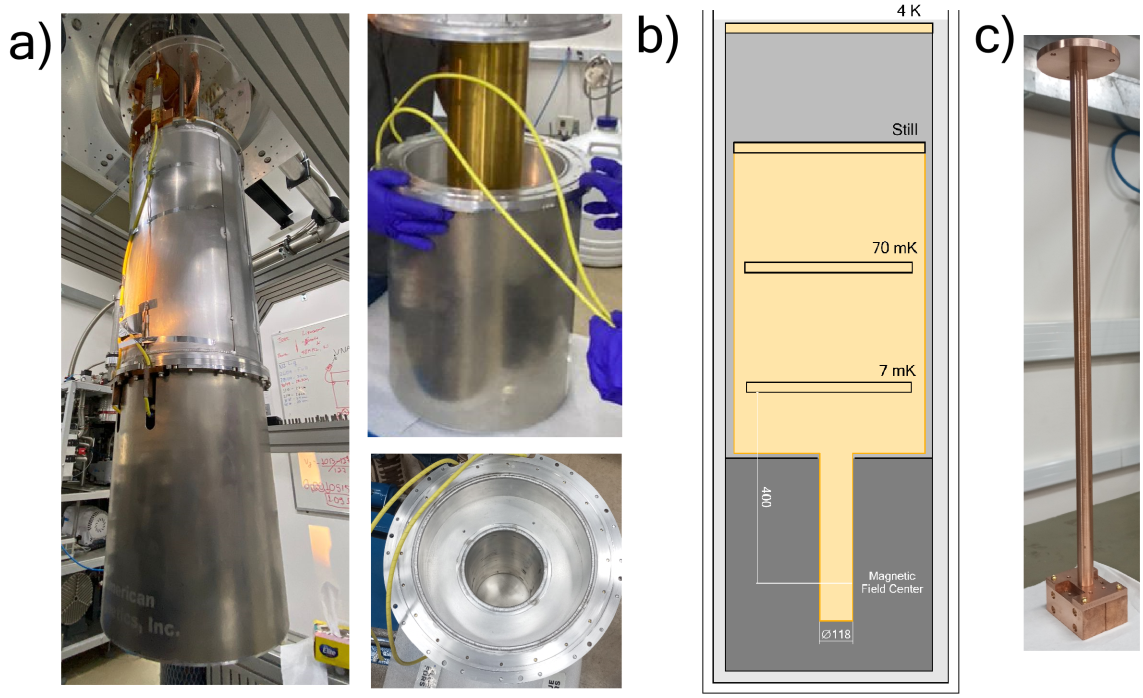

Figure 23 – a) On the left is a picture of the DR with its aluminium shield and the superconducting magnet at the bottom. The magnet is connected to the 4K stage. Aluminium thermal shields are still to be added before the vacuum can that closes all. On the upper right, the magnet is being installed. On the bottom right, an overhead image of the magnet is shown b) An schematic of the lowest temperature stages, showing the mounting. There is the vacuum can at the outside, a thermal aluminium shield, then another aluminium at the top and the magnet at the bottom, both connected at the 4K stage. There is then the innermost shield of OFHC copper coated in gold. c) Sample holder designed to anchor the cavity at the MXC and position it at the center of superconducting coil.

3.3.2 Sample Holder

In order to thermally anchor the cavity with the sample to the MXC flange and also position it at the magnetic field centre of the coil – that is 400 mm down from the MXC –, a sample holder was designed (Figure 23c). Firstly, as Cavity A (see 2), that was mostly used in the experiments at room temperature, is made of aluminium, that is a superconductor, another cavity had to be designed made out of copper. This is Cavity C, that have the same inner dimensions as Cavity A, but the metallic box was made bigger in order to pass screw holes through its y direction. Then a connector was developed to fix the cavity to a copper rod by these holes, positioning the cavity y direction along the magnetic field direction (vertical). It was also thought about the possibility – for future experiments, not related to this thesis – to align the cavity in the z direction, so the conector have four additional holes to attach the cavity by its backside. Finally the copper rod is mounted in the MXC flange with a rod holder. The schematics of all these pieces are presented on Appendix F.

3.3.3 Cavity Ringdown Setup

Spectroscopic measurements at cryogenic temperatures were essentially taken like the ones at room temperature: the magnetic field was varied and a spectrum from the VNA recorded. Taking advantage of the advanced microwave measurement systems of the LFDQ that were built to measure superconducting qubits, we performed a cavity ringdown measurement that used a heterodyne downconversion setup and a broadband fast oscilloscope with 20 GSa/s (giga sample per second). Figure 24 show the heterodyne circuit. It uses two mixers and three rf generators. Figure 25 show the complete schematic of the measurement system. One of the generators was modulated by a Arbitrary Wave Generator that created pulses of 200 µs, this signal was then combined with 240 MHz to have the frequency of the cavity; this was sent to the sample. The transmission was then down-converted with the use of another microwave generator, producing again a signal of 240 MHz, which was recorded on the fast oscilloscope. This way, we could send pulses to the cavity and read its transmission; in particular, analyse the end part of the transmitted pulse that have the exponential decay given by the photon lifetime (related to the cavity quality). This type of measurement is called cavity ringdown spectroscopy.

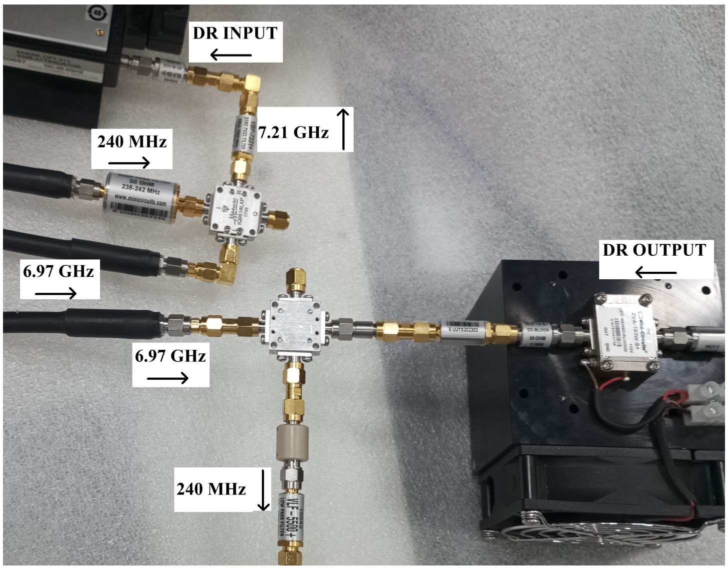

Figure 24 – Image of the heterodyne microwave circuit assemble. A signal of 6.97 of a generator is combined with another of 240 MHz to send a signal of 7.21 GHz to the cavity. The return signal is down-converted to 240 MHz

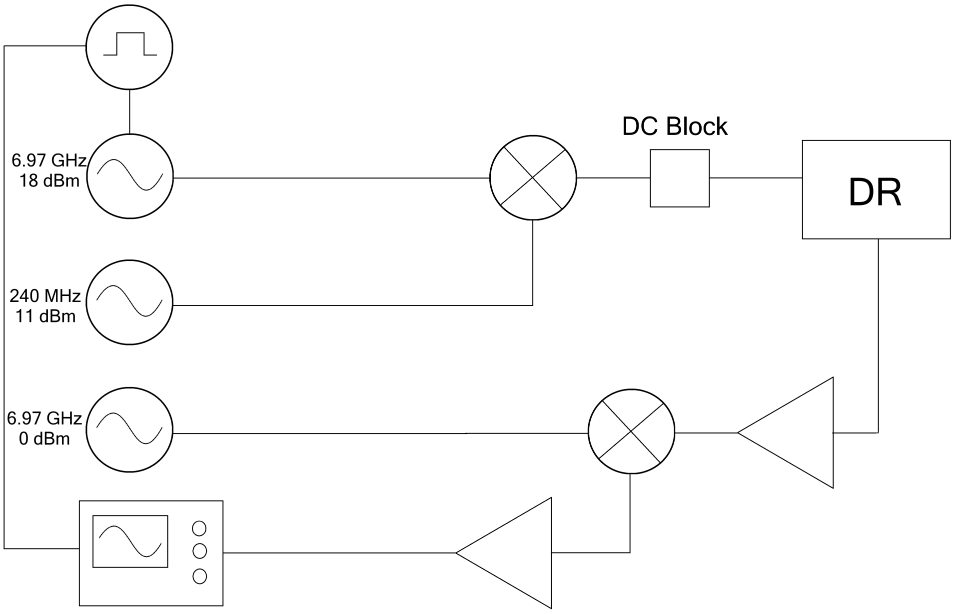

Figure 25 – Schematic of the circuit used for the cavity ringdown spectroscopy. A microwave generator was modulated by an arbitrary wave generator (AWG) that created pulses. This signal was later combined to 240 MHz to send a pulsed signal of 7.21 GHz to the sample. The transmitted signal after amplification was down-converted using another microwave generator to 240 MHz that was recorded on a fast oscilloscope. The oscilloscope trigger was set at the rising of AWG.

4 Measurements and Analysis

This chapter presents the results of the measurements realized and analyse them under the light of the presented theory.

4.1 Microwave Cavities Characterization

For the experiments, three microwave cavities, denoted A, B and C were used. The first two were made of aluminium and used at the room temperature experiments – for instance, cavity B was only used in the FMR with multiple wires (described in the next section). Cavity C was made of copper and used at the mK experiments. It had the same dimensions of cavity A, but with different couplings κ_1 and κ_2.

To characterize the cavity modes, the S parameters as a function of frequency were measured with the VNA. At the resonance, the transmission (reflection) is a maximum (minimum) and its width is related to the quality of the mode by Equation 1.6. The transmission parameter around a resonant mode have the form given by Equation C.2 when the VNA is not calibrated but follows Equation C.1 as the ideal response, where the magnitude is Lorentzian.

Figure 26 presents a transmission spectroscopy of Cavity A, where 3 resonant peaks are observed. Using the dimensions of this cavity (26 mm $\times$ 8 mm $\times$ 36 mm), the fundamental mode TE_{101} estimation based in the Equation 1.5 for rectangular cavities gives 7.1 GHz, which is close to the measured value. The same happen for the other modes. A simulation of the scattering parameters using software that solves Maxwell's equations with Finite Element methods, incorporating the input geometry and real properties like finite conductivity, provides a more precise prediction. The resulting response (black curve of Figure 26) closely matches the measurement.

By measuring around each prominent peak of each cavity with the VNA calibrated and using the fitting procedure in Appendix C (when applicable), the mode frequencies and qualities of the three cavities are determined, as shown in Table 2.

The field configuration of the cavity can also be estimated using the Expressions 1.4 of the rectangular box, but to precisely determine the mode distributions for a cavity, simulations give better results, especially for complicated geometries. Figures 27 and 28 show the field configurations for the fundamental mode TE_{101} of the cavity A and C. Knowing the fields configurations is important to determine where to place the sample on the cavity, considering direction of the RF fields and mode function distribution – which are related to the intensity of vacuum fluctuations by Equation 1.9. Assuming the same

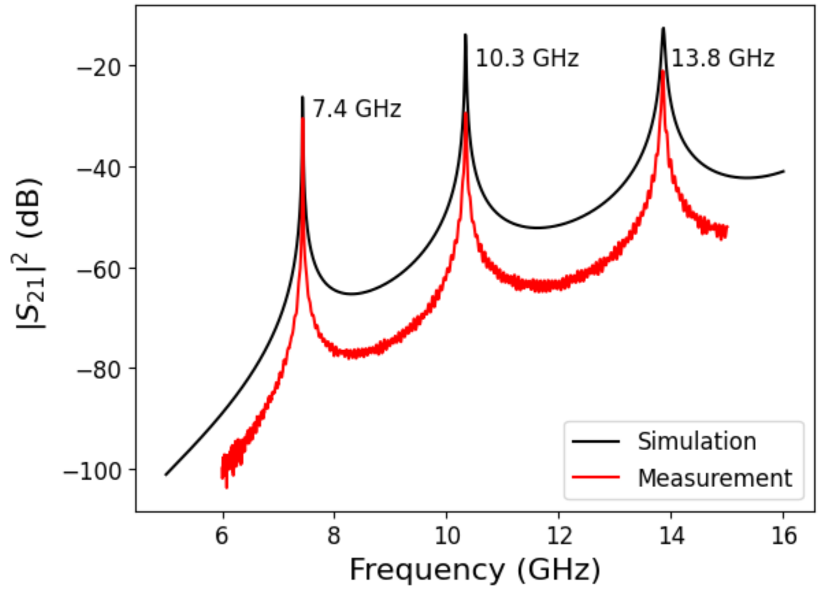

Figure 26 – Measured broadband transmission response of Cavity A in red showing three resonance peaks. In black, the simulated response performed on *CST Studio Suite*. The first peak corresponds to the resonant mode TE_{101} and the second to TE_{102}; the third contains the modes TE_{103} and TE_{201} superimposed

Peak	Frequency	Quality
Cavity A (TE_{101})	7.435 GHz	3000
Cavity A (TE_{102})	10.328 GHz	1300
Cavity A (3rd peak)	13.8 GHz	-
Cavity B (TE_{101})	5.605 GHz	400
Cavity B (2nd peak)	8.7 GHz	-
Cavity C (TE_{101})	7.406 GHz	2200
Cavity C (TE_{102})	10.280 GHz	500

Table 2 – Characterization at room temperature of the peaks of the three cavities, showing the peak frequency and quality. The peaks in that the quality are not displayed are formed by the superposition of two different modes and were not fitted.

convention of coordinate system as in Chapter 1, where the z direction is taken along the largest side, y along the smallest, and the origin in a corner, for this mode there are four magnetic field antinodes: $(x = 0, z = L_z/2)$, $(x = L_x, z = L_z/2)$, $(x = L_x/2, z = 0)$ and $(x = L_x/2, z = L_z)$; and one electric field antinode: $(x = L_x/2, z = L_z/2)$. Also note that the field is approximately uniform in the y direction

As a reference, an FMR experiment was performed in empty cavity A to record its background. There is, in fact, a broad resonance, that for the 7.43 GHz mode happens at 0.92 mT, with a signal amplitude of $\Delta S_{21} \sim 8 \times 10^{-4}$ (see Appendix G). Only signals bigger than this value was then considered.

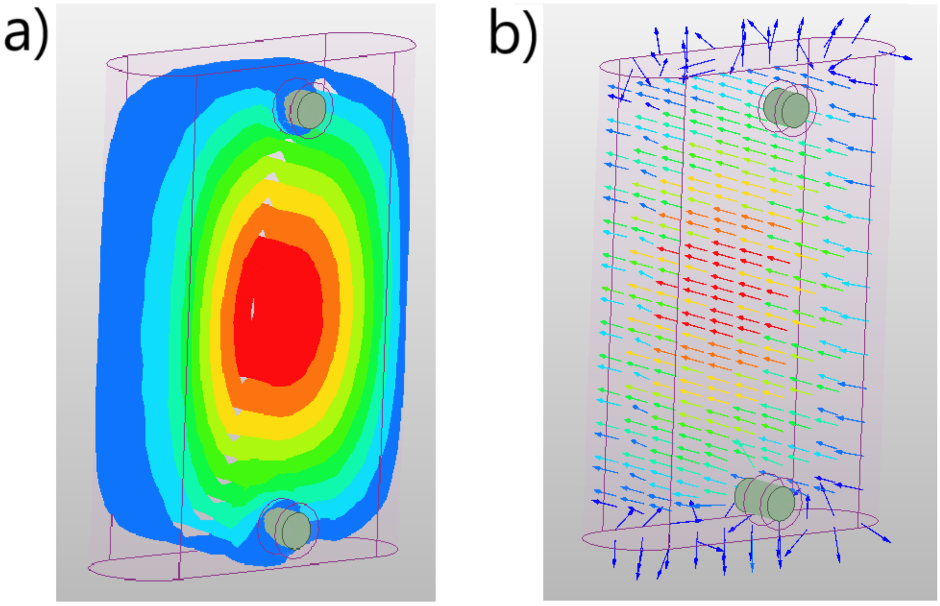

Figure 27 – Electric field configuration for the TE_{101} mode of Cavity A. In a) the variation of the intensity is shown, from cold to hot. In b) the direction of the field is shown. Note that this qualitatively agrees with equations 1.4. This was simulated on *Ansys HFSS*

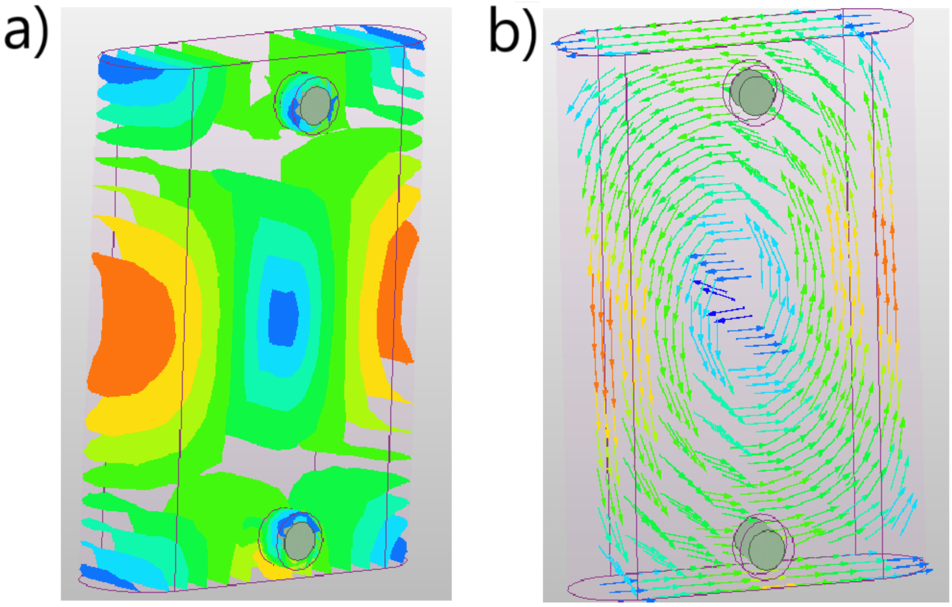

Figure 28 – Magnetic field configuration for the TE_{101} mode of Cavity A. In a) the variation of the intensity is shown, from cold to hot. In b) the direction of the field is shown. Note that this qualitatively agrees with equations 1.4 . This was simulated on *Ansys HFSS*

4.2 Room Temperature FMR at the Magnetic Antinode

Due to the small size of the wires, measuring the signal from a single wire at the magnetic field antinode is too difficult with our setup. Attempts were made, but the signal was indistinguishable from the background. To measure the signal from a single wire in this position, a Phase Locked Loop FMR (PLL-FMR) was performed at the Laboratory of Metals and Alloys (GLM) using a conventional ESR setup. The wire was fixed at the bottom of a small paper reel and inserted in a quartz tube designed for this setup; the tube was installed into a TE_{102}, 9.131 GHz cavity at the magnetic field antinode. The wire was aligned with the static field. Figure 29 show the result of the measurement. The curve is proportional to the derivative of the FMR absorption (REZENDE, 2020). The resonance occurs on the passage from the positive to the negative sign, that is estimated to happen at the applied field of 110 mT . This agrees with the Kittel plane formula for the cavity frequency. The low signal-to-noise ratio for even such sensible technique shows how low is the strength of the interaction in this position.

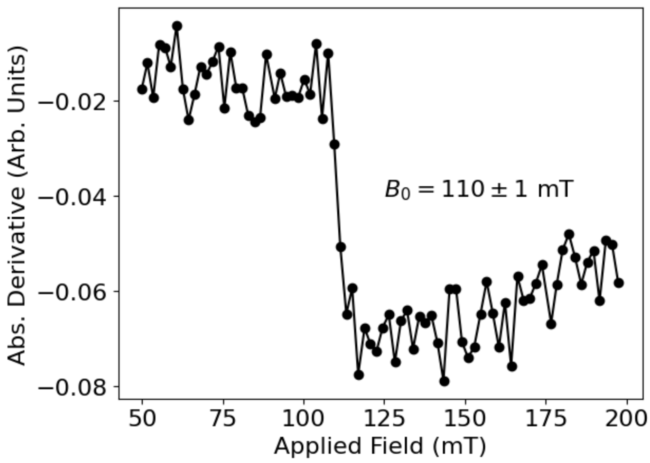

Figure 29 – Phase Locked Loop FMR of one wire performed in a ESR setup showing the signal that is proportional to the derivative of absorption. The resonance happens at the field of 110 mT.

To increase their interaction, a sample containing 67 microwires was prepared. The microwires were manually inserted into a glass capillary with 6 mm length and 0.1 mm of internal diameter. This sample was positioned at $z = L_z$ and $x = L_x/2$, as shown in Figure 30a, in the cavities A and B, corresponding to a magnetic field antinode for the first two modes: TE_{101} and TE_{102}. The transmission spectrum S_{21} was recorded as a function of the applied field up to 0.32 T for each mode and each cavity, corresponding to four different resonance frequencies: 5.6 GHz, 7.4 GHz, 8.7 GHz, and 10.3 GHz (Figure 54, S_{21}).

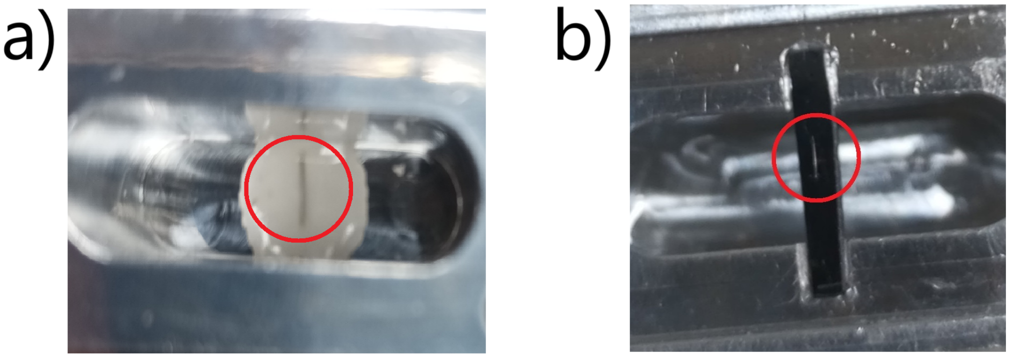

Figure 30 – a) A tube containing 67 microwires is secured with paraffin wax parallel to the y-axis at the bottom of the cavity at a position corresponding to a magnetic field antinode for modes TE_{101} and TE_{102}; b) A single wire, affixed with cryo varnish to a silicon die, is positioned at the center of the cavity, aligning with an antinode of the electric field.

The four measurements display a dip in transmission intensity at certain field values. To highlight these dips, Figure 32 presents the background-subtracted spectra, where the spectrum of each field value was subtracted by that of the highest field – far away from the dips. These dips in transmission are interpreted as absorption due to ferromagnetic resonance of the sample. Figure 33a show the absorption lineshape by tracing the middle frequency of the spectra. The fields at the minimum of were plotted against the mode frequencies (Figure 33b) along with the prediction given by the Kittel Plane Formula 1.29 with $\mu_0 M_s = 0.84\,\mathrm{T}$[1]. The agreement suggests that for our wire and this range of frequencies, the resonance condition is captured by this formula, at least for multiple wires in this position.

[1] Initially, the nominal value of 0.85 T was used and also fits well; however, a value of 0.84 T provides an even better fit, and was therefore used in subsequent analyses.

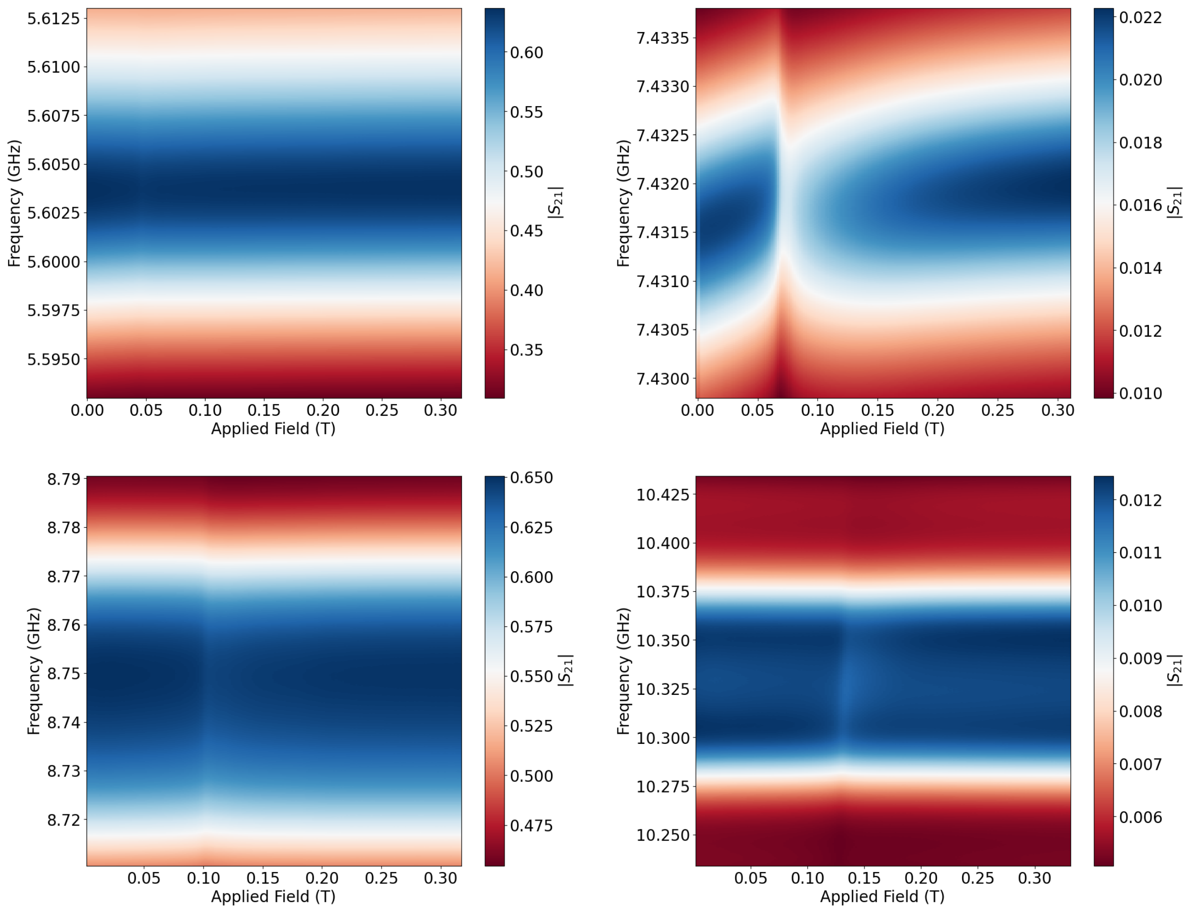

Figure 31 – Data from the field-dependent spectroscopy performed on the sample containing 67 microwires for two modes of two different cavities. The high transmission centres in frequency are the cavities resonant peaks. At certain field values, this transmission diminishes in amplitude. For the 7.4 GHz mode there is also a change in resonance frequency that comes from the coupling and is better explored next section. The spectra of 7.4 GHz and 10.3 GHz are from cavity A, while the other two are from cavity B.

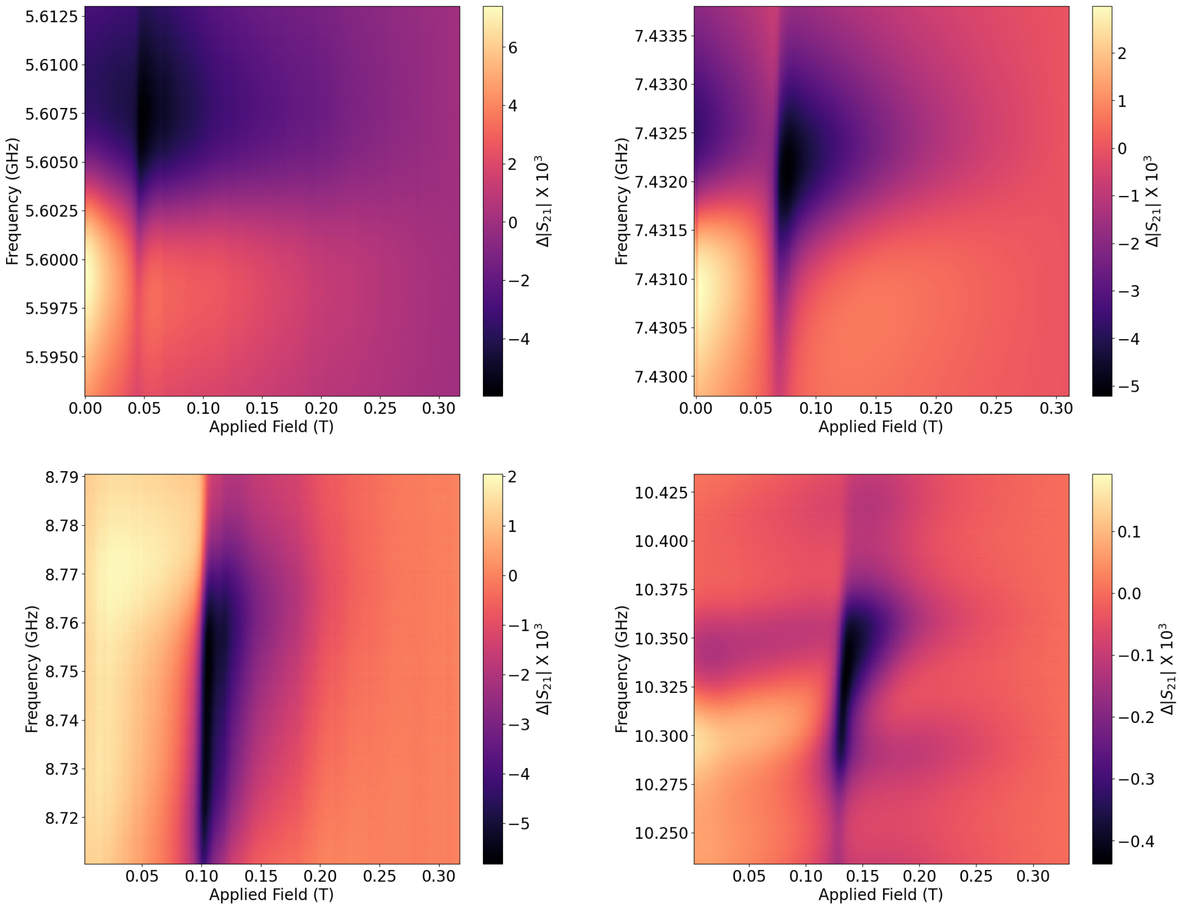

Figure 32 – Background-subtracted data from the field-dependent spectroscopy performed on the sample containing 67 microwires for two modes of two different cavities. Each of the four spectra exhibits a significant drop in transmission at specific field values corresponding to FMR absorption

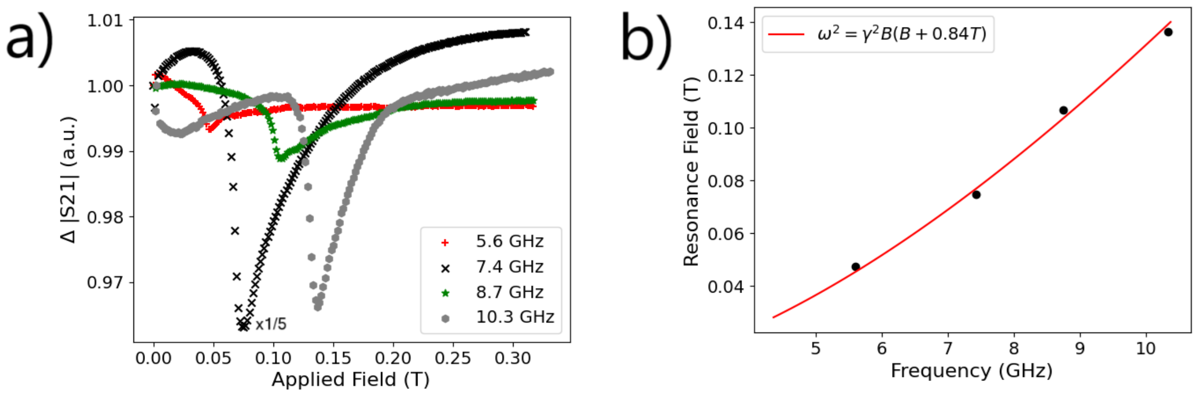

Figure 33 – a) Traces in the middle of the measured spectrum for the four frequencies. The dip in transmission correspond to the resonant absorption. The spectrum of 7.4 GHz was scaled by 0.2, and all curves were normalized b) Plot of the fields corresponding to the minimum of transmission for each frequency compared to the prediction given from Kittel's Plane Formula with $\mu_0 M = 0.84$ T

4.3 Room Temperature FMR at Rodbell Position

The measurement setup described in the previous section, where the sample is located at the magnetic antinode, is the conventional one used in cavity magnonics experiments. As outlined in Section 1.7, metallic microwires can also couple to the microwave cavity through the electric field. This section explores this scenario, where the microwire is positioned at the cavity's electric antinode aligned with the field. When placed in such a position, the wire behaves like an antenna, and the longitudinal electric field that generates an alternating current induces strong circular magnetic fields that significantly couple to the magnetization mode $n = 0$. This gives a strong FMR signal for even just one wire.

The samples were positioned at $z = L_z/2$, $x = L_x/2$ within cavity A, corresponding to a maximum of the electric field and a minimum of the magnetic field for the mode TE_{101} (Figure 27). Two arrangements to hold the microwires were used: in the first, the microwire was affixed to a piece of silicon using cryogenic varnish as shown in Figure 30b; in the second configuration, they were simply attached to a piece of paper using double-sided tape. The transmission and reflection parameters were measured with a calibrated VNA with 0 dBm (1mW) of input power.

4.3.1 FMR Spectrum and Harmonic Model

A measured reflection S_{22} spectrum of an electric field-coupled microwire is shown in Figure 34. The first noticeable effect of positioning the microwire in this location is a significant perturbation of the cavity resonance frequency due to the strong interaction of the metallic wire with the mode TE_{101}. In the measurement shown in Figure 34, the resonance at zero field shifts the cavity frequency from 7.435 GHz to 7.400 GHz. Then, as the magnetic field is varied, a peak in reflection is seen at ± 76 mT,corresponding to the Kittel plane resonant condition for the cavity frequency. The cavity frequency also bends close to the FMR, forming a tail of high reflection that resembles the anti-crossing pattern. Close to zero-field there is also a small resonance that we attribute to magnetization phenomena (CHIRIAC et al., 1999) or giant magneto impedance effects (PIROTA et al., 2000) and we do not investigate further. A measurement was also taken at -15 dBm (0.03 mW) of input power holding a very similar spectrum, indicating linear regime.

Considering the discussion of sections 1.7 and 1.5, the results are interpreted as follows: in this configuration, the magnetization precession mode $n = 0$, with frequency $\omega_m(B)$ as given by the Kittel Plane Formula 1.29, is significantly coupled with the perturbed cavity mode. This coupling is assumed to be linear, as in Equation 1.35, where g depends on the induced magnetic field, and hence on the electric field.

To further investigate the results under this picture, the reflection curves around

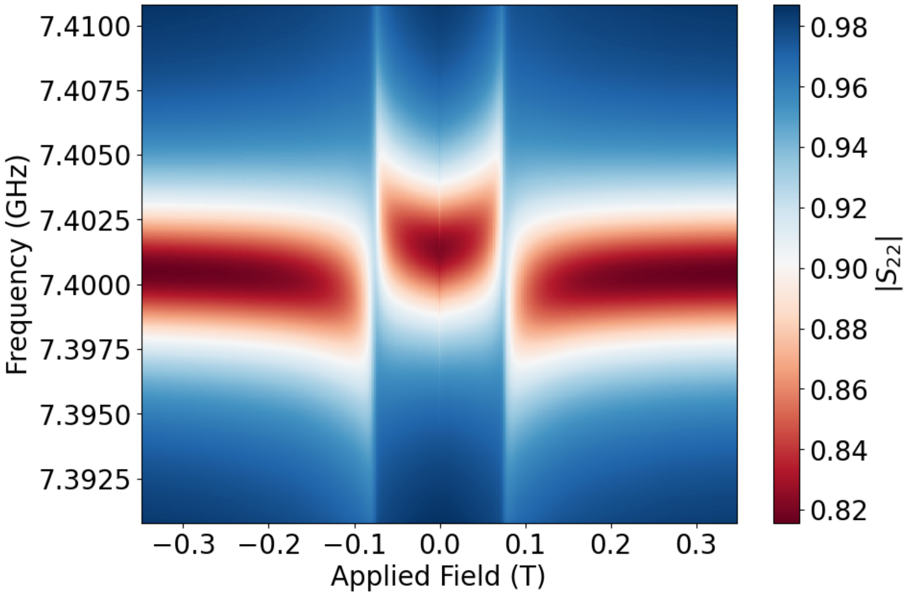

Figure 34 – Field-depedent reflection spectra around cavity resonance for a wire of 4 mm glued in paper at Rodbell position. The cavity resonance was shifted from 7.435 GHz to 7.40 GHz. The "slashes" are the FMR resonance consistent with Kittel Plane condition.

the FMR resonance are plotted in Figure 35. Even at resonance, only one distinct valley is observable, indicating that the system is at the weak coupling regime (Section 1.5). In Figure 35, one sees that the cavity resonance frequency slowly rises with the field until the ferromagnetic resonance (dotted cyan), from where it rapidly shifts to lower fields and starts rising again. The dispersion and the quality of the peaks causes a significant difference in reflection at the tails that creates the "halo" or tails around the resonance. We note that the transmission spectrum similarly shows a dip corresponding to the resonance and the bent 'fingers,' but no strong tails are visible due to the diminished dissipation rate at the other port.

Fitting a Lorentzian curve in the spectrum $|S_{22}(f)|^2$ for each field, this behaviour get more clear. The resonance frequency and the width, corresponding to the dispersion and absorption of the system are plotted in 36. The response has the form of a linear susceptibility, as discussed in section 1.5. Fitting the equations 1.44 and 1.45 on the data gives the red curves (36). The experimental data are asymmetrical and the agreement is only relative. The R^2 values of the fitting are around 0.96 for the data around the resonance [2]

The fitting of the dispersion gives the parameters $\omega_c/(2\pi) = 7.401\,\mathrm{GHz}$, $g/(2\pi) = (42.6 \pm 0.5)\,\mathrm{MHz}$ $\eta/(2\pi) = (0.95 \pm 0.06)\,\mathrm{GHz}$, while the fitting of the absorption

[2] The coefficient of determination R^2 of the Lorentzian fits are all above 0.999, showing a very good agreement with the expected cavity response in this regime, and confirming that the asymmetrical features of the curves are due to deviations of the model described by Equations 1.44 and 1.45.

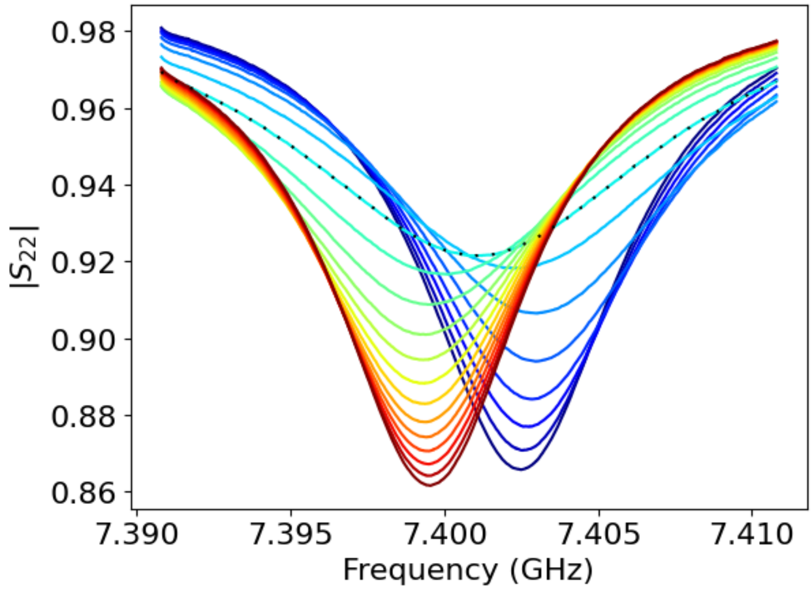

Figure 35 – Plot of 20 reflection curves (vertical cuts of Fig. 34) for progressively different values of magnetic field from dark blue (63.9 mT) to dark red (97.5 mT) passing through the ferromagnetic resonance at 76 mT (dotted cyan)

[3] gives $\kappa/(2\pi) = 6.6\,\mathrm{MHz}$, $g/(2\pi) = (37.5 \pm 0.8)\,\mathrm{MHz}$ and $\eta/(2\pi) = (0.72 \pm 0.04)\,\mathrm{GHz}$. These values are close but do not coincide. Also κ is considerably higher than the actual baseline of the measurement far from resonance. In section 4.6, we discuss the asymmetry and perform a better fitting of the absorption considering the theory of FMR in wires based on the surface impedance (Equation1.54). For the moment, the fitting based in the equations 1.45 and 1.44 serves as a first analysis and provide figures for the important parameters of the cavity-magnet interaction.

To highlight the absorption due to the interaction between the electromagnetic field inside the cavity and the magnetic microwire, the background-subtracted spectrum – given by $|S_{22}(B)| - |S_{22}(0.35\mathrm{T})|)$ – of the positive-field measurement of Figure 34 was taken , essentially removing the bare cavity response (BOVENTER, 2019; SMITH et al., 2024) . Using $g/(2\pi) = 40\,\mathrm{MHz}$[4], we also plot the eigenfrequencies predicted from Equation 1.38 in comparison with this background subtracted data. The splitting due to the resonant interaction is apparent, and the spectrum agrees well with the predicted polariton frequencies, corroborating the model of two coupled harmonic oscillators for this coupling.

Finally, to strengthen the comparisons with the model even further, using the

3 The value of ω_c obtained from the dispersion fit was fixed in the absorption function to avoid over fitting. There are other ways of obtaining ω_c, like from the lorentzian fit for a distant field and the results do not change much, but allowing ω_c as a free parameter in κ_{cav} usually gave a wrong value that did not agreed with the data

4 The mean value obtained from the ω_{cav} and κ_{cav} fitting

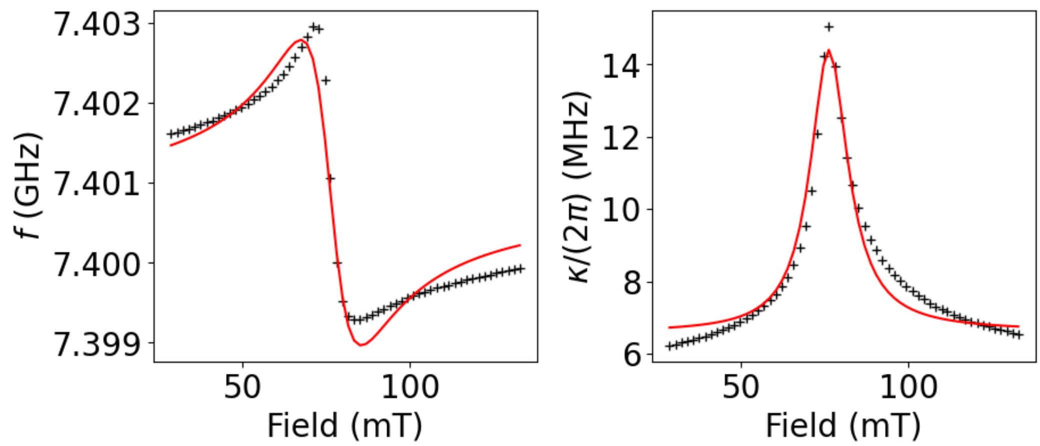

Figure 36 – Cavity frequency and width as a function of the field for the measurement of Figure 34, corresponding respectively to the dispersion and absorption of the response. In red, the fit based in the equations 1.44 and 1.45 are displayed, showing that the data is asymmetrical.

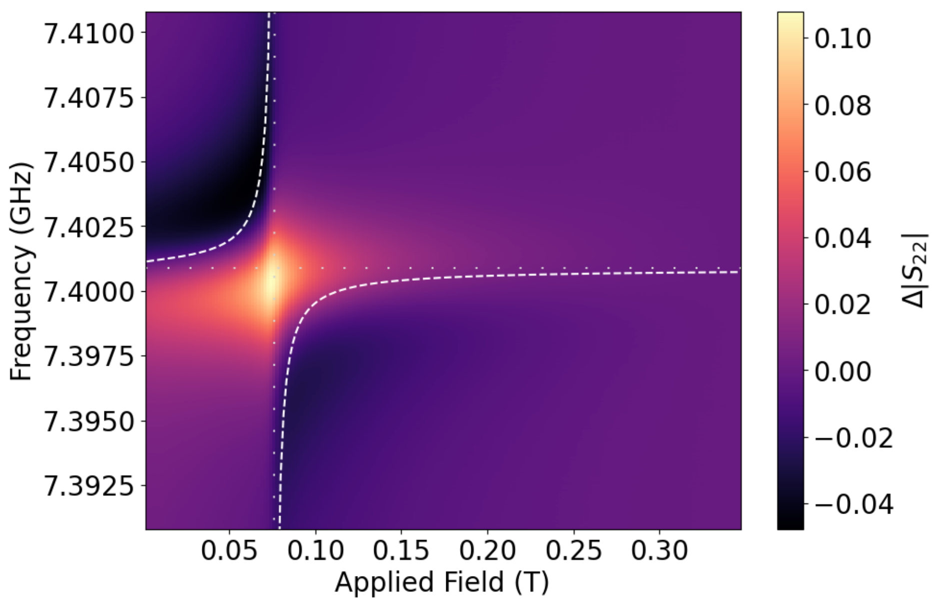

Figure 37 – Background subtracted data of Figure 34, showing that the absorption structure close to resonance is approximately guided by the predicted polariton eigenfrequencies in dashed lines. The dotted lines are the frequencies of the bare perturbed cavity frequency $\omega_c/(2\pi)$ and Kittel $\omega_m/(2\pi)$.

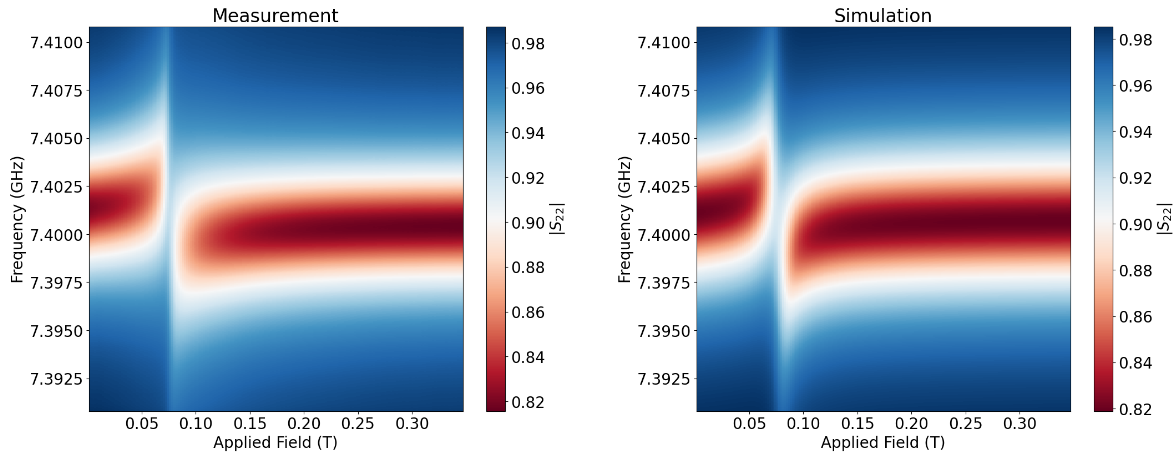

Figure 38 – Positive-field part of the measured spectrum of Figure 34 sided by the numerical simulation of the model expressed by Equation 4.1 with the parameters: $\kappa/(2\pi) = 6.61\,\text{MHz}$, $\eta/(2\pi) = 840\,\text{MHz}$, $\kappa_{2,ex}/(2\pi) = 0.6\,\text{MHz}$, $\omega_c/(2\pi) = 7.40\,\text{GHz}$, $g/(2\pi) = 40\,\text{MHz}$

microwave reflection coefficient obtained from input-output theory, described by:

$$S_{22} = 1 + \frac{\kappa_{2,ex}}{i(\omega - \omega_c) - \frac{\kappa}{2} + \frac{g^2}{i(\omega-\omega_m)-\eta/2}}, \tag{4.1}$$

we simulate in Figure 38 the spectrum of $|S_{22}|$, using the mean values of parameters obtained from the fitting of the curves of Figure 36 and the coupling port value $\kappa_{2,ex} = 0.6\text{MHz}$. The resemblance is high, showing that the description given by section 1.5 can be used to explain and analyse the data.

4.3.2 Coupling Dependence on Wire Position

To further explore the electrically induced cavity-magnet coupling, an experiment was conducted where the position of the wire along the x-axis was varied. In the measurement discussed in the previous section, the magnetic microwire was placed at the center of the cavity ($x = L_x/2$) and had an estimated coupling strength of $g/(2\pi) = 40\,\text{MHz}$. In this new set, the wire was shifted off-center by 5 mm and 8 mm. The reflection spectra, shown in Figure 39, demonstrate a reduction of the dispersion amplitude, representing a reduction of the cavity-magnet coupling, with fitted values of $g/(2\pi) = 33\,\text{MHz}$ and 21 MHz, respectively.

From the electromagnetic field distribution for the mode TE_{101}, depicted in Figure 27, it is evident that the electric field diminishes outward from the center, which supports the claim that the coupling grows with the amplitude of the electric field mode function, or E_{ZPF}, of the unperturbed cavity. Not only that, but the magnetic field increases in this direction, evidencing that the coupling with the electric field is much more dominant. Taking the coupling at the center $x = L_x/2$ as a reference, the two couplings

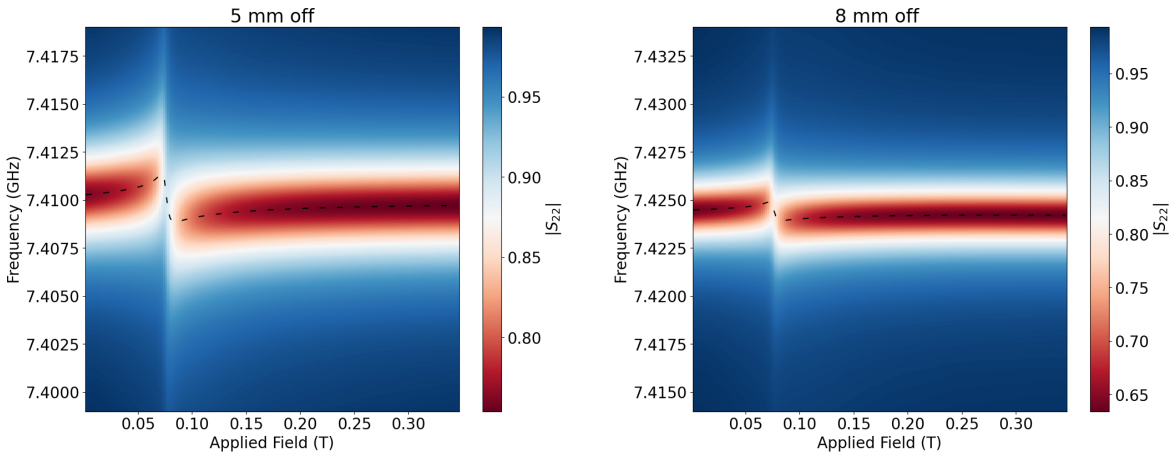

Figure 39 – Spectra for two dislocations off center of the wire: 5 and 8 mm. The dashed lines show the dispersion. The amplitude variation for the 5 mm shifted wire is smaller than the center wire (Figure 36) and bigger than the 8 mm shifted wire. The perturbation of the cavity also diminishes as expected.

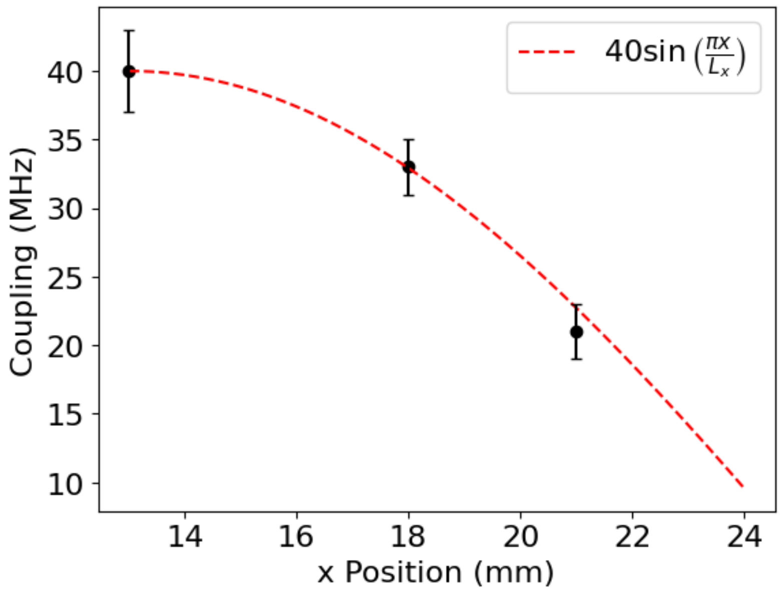

Figure 40 – Dependence of the coupling with the x position of the sample, compared with the sine dependence of electric field normalized by the coupling at $x = L_x/2$ (40 MHz). The error bars were taken as the distance between the g's obtained from the fitting of the dispersion and absorption, and g by the mean.

were plotted in comparison with the electric field sine dependence in x of the rectangular box cavity (Figure 40). Although there are just two points, the good agreement suggests a proportional relationship $g \sim E_{ZPF}$.

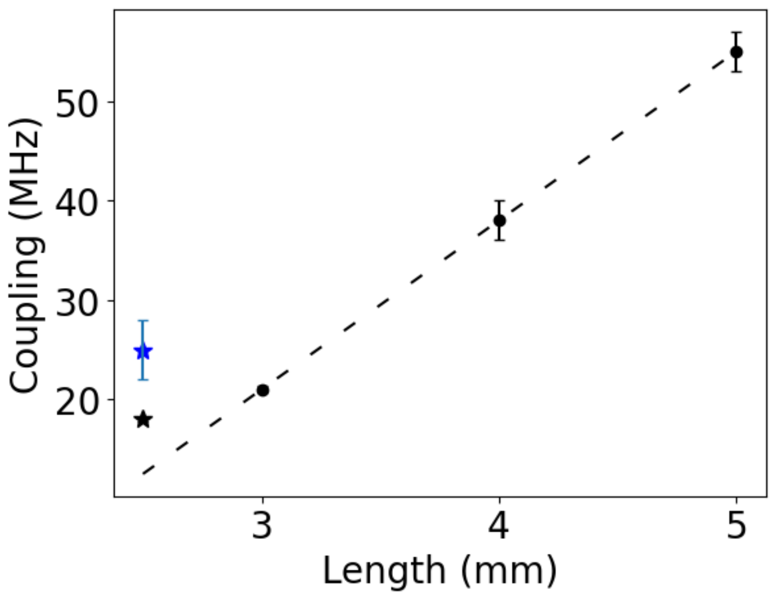

Figure 41 – Dependence of the coupling with the length of the wire. The black star is the coupling for the sample in silicon measured by cavity A, and the blue star is the coupling for the same sample but measured by cavity C.

4.3.3 Coupling Dependence on Wire Length

A separate set of experiments examined the effect of varying the length of the wires on the coupling strength. Different wire lengths of 3 mm, 4 mm, and 5 mm were tested by affixing them to paper. Additionally, a microwire of 2.5 mm was prepared and affixed to silicon die for comparative analysis in a cryogenic setup.

Figure 41 shows the coupling strength as a function of the microwire length. The data demonstrate a linear relationship between wire length and coupling strength, described by $g/(2\pi) = 17L - 30$ MHz. The nonzero intercept of the linear relationship suggests a potential nonlinearity close to zero length. Additionally, this linear dependence on L differs from the expectations of the coupling (Equation 1.36), where it should scale with the square root of the number of spins $\sqrt{N}$, hence with $\sqrt{L}$. For the range of lengths measure here, the observed linear dependence supports the model of electric dipole coupling $g \sim LE$ for this electrically induced cavity-magnet interaction studied here. This difference must be caused by the relationship of the induced magnetic field with the electric field and the geometry of the sample. We note that the length dependences found are different than the ones measured by Rodbell (RODBELL, 1959b).

The sample on silicon with a length of 2.5 mm, show disagreement with the linear dependence. This could be associated with a effect dielectric effect of the silicon that changes the electromagnetic environment felt by the wire. Similarly, when measured in a different cavity (blue star in Figure 41), that has different electromagnetic characteristics, like the different couplings, the coupling constant also changes for the same sample.

4.3.4 Comparisons

The measurement of the wire in the Rodbell position gives a signal much stronger than the wire at the magnetic antinode. This is evidenced by the fact that the signal of the wire in this position could not even be measured, being lower than the cavity magnetic background response $\Delta S_{21} < 10^{-4}$. The strongest signal with 67 microwires had an amplitude of $\Delta S_{21} \sim 4.8 \times 10^{-3}$. A single microwire of 4 mm at Rodbell position had an amplitude signal of $\Delta S_{21} \sim 1.3 \times 10^{-2}$. This is at least two orders of magnitude bigger than the signal of a single wire, meaning that the coupling is more than 10 times bigger.

The values of coupling obtained are common in Cavity Magnonics experiments (Table 3). A figure normally used to compare the efficiency of the microwave setup is the coupling per spin g_s that is calculated by $g/\sqrt{N}$. Estimating the density of spins in the wire to be $\sim 7.3 \times 10^{28}\,\mathrm{m}^{-3}$, this gives for the wire of 4 mm – as our g also varies with L – $g_s \sim 2\pi \times 300\,\mathrm{mHz}$. For our cavity, it is estimated a $g_s = \gamma\sqrt{\mu_0 \hbar\omega/V} \sim 2\pi \times 25\,\mathrm{mHz}$, giving four our setup more than 10 times the coupling – in agreement with the estimation above. Our dissipation is considerably higher than other experiments, though.

Parameters	PY on CPW and LE[5]	YIG 3D Cavity[6]	CoFeSiB 3D Rodbell
$g/(2\pi)$	8 - 172 MHz	47 MHz	40 MHz
$g_s/(2\pi)$	18 Hz (CPW)/ 263 Hz (CPW)	38 mHz	300 mHz
$\eta/(2\pi)$	120 MHz	1.1 MHz	840 MHz

Table 3 – Comparison of parameters find in the literature with the estimated parameters of our system. The first column refers to permalloy (PY) films of different thickness on coplanar waveguide resonators and lumped element cavities. These planar systems have a more concentrated field distribution that substantially increases the coupling per spin compared to 3D cavities. The dissipation of PY films are also substantially big. The coupling g_s at Rodbell position is approximately 10 times bigger than the conventional one using 3D cavities of typical dimensions.

4.4 Cryogenic Spectroscopies

In this section, we present our measurements of the cavity-microwire system at ultra-low temperatures ($\leq 10\,\mathrm{mK}$). The cavity with the sample on silicon at the Rodbell position was anchored to the mixing chamber of a dilution refrigerator equipped with an 8 T superconducting magnet coil, as illustrated in Figure 22. With the reduction of temperature, it was expected a reduction in dissipation of the magnetic system, implicating an improvement in the effective cavity-magnetic system coupling.

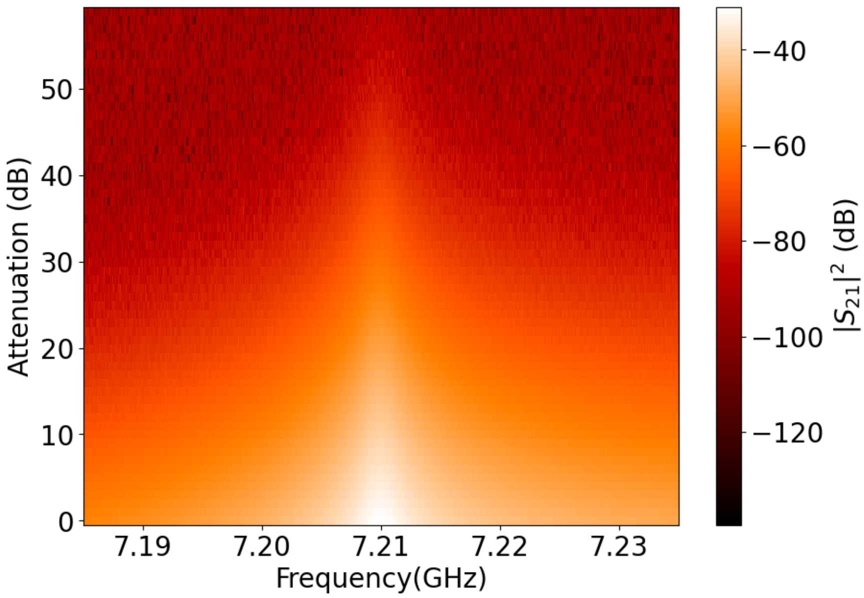

Figure 42 – Power Sweep performed on the cavity at zero field. The power used on the VNA was -5 dBm, and there were a base total att. of -59 dB descending toward the cavity, added to that is the att. of the attunator that is swept. The power range thus goes from -64 dBm to -123 dBm

4.4.1 Cavity Power Sweep

We initiated the measurements by identifying the resonance of the cavity using the VNA. Based on the measurements at room temperature, the resonance of the coupled system at zero field $\omega/2\pi = 7.210$GHz is observed to increase by 32 MHz relative to room temperature measurements.

To examine the effect of drive strength, we conducted a power sweep cavity spectroscopy without any external magnetic field. Figure 42 displays the cavity's transmission spectrum as a function of applied attenuation ranging from -64 dBm (approximately 10^6 photons) to -123 dBm (approximately 10 photons). The analysis of the quality factor of the cavity as a function of the drive strength shows negligible change until about -100 dBm, after which its value begins to increase, reaching up to approximately 4600 at -123 dBm. This decrease of loss could be an effect of the wire or the cavity itself. The internal losses of the cavity depend on its surface quality, including imperfections, microfractures and oxide layers. It also depends on the surface resistivity of the metal that decreases with temperature. In superconducting planar resonators the quality factor varies with power due to the dominant contribution of a bath of two level systems (TLS) in their dissipation (MCRAE et al., 2020; KIM et al., 2014), while superconducting 3D cavities made of aluminium do not have such variation (KIM et al., 2014; REAGOR et al., 2013). Assuming the situation with a resistive metal like copper would be similar, the observed variation is probably due to the wire; a power sweep of the empty copper cavity – maybe with a piece of silicon inside too – could confirm this. No studies were found performing

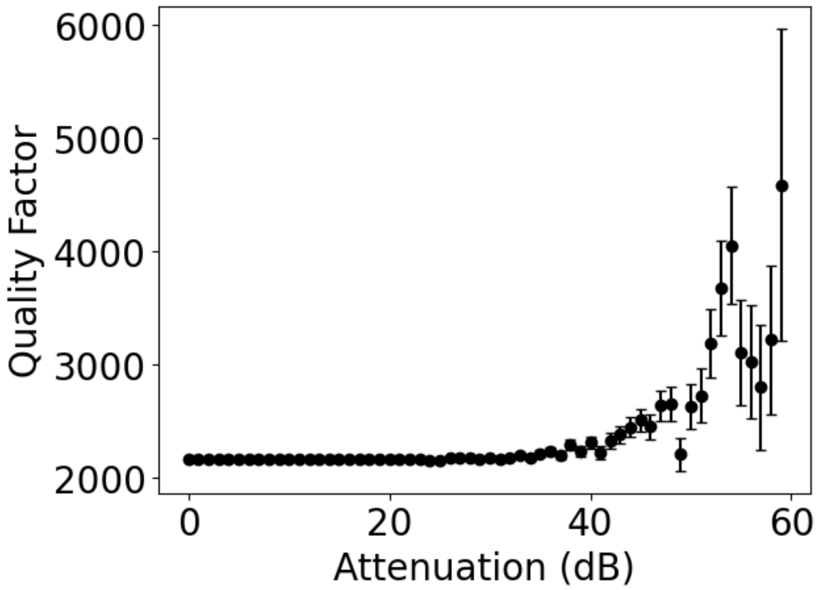

Figure 43 – Cavity quality as a function of the attenuation

such measurements in a copper cavity. No further investigations were conducted on this matter.

4.4.2 Cryogenic FMR at Rodbell Position

The field dependent spectroscopy was performed using the superconducting coil. The current in the coil was controlled by a power supply and the field was calculated using the coil conversion factor specified in its manual. Because of the non-reciprocal nature of the DR circuit (Figure 22b), only the transmission parameter S_{21} parameter was measured, without calibration. The power on the cavity was -99 dBm.

The measured transmission spectrum (Figure 44) displayed a pattern similar to that observed at room temperature, featuring a strong fall in quality at the resonance, and slight bend around it, but no anti-crossing pattern, indicating that the reduction of temperature did not brought the system to the strong coupling regime. It is noted that the resonance now occurs at a lower external magnetic field of 53 mT, consistent with an increase in the saturation magnetization due to decreased thermal fluctuations.

Considering the fact the $|S_{21}|$ was taken without calibration, the curves were now fitted at the skewed Lorentzian C.4. The resulting dispersion and absorption as a function of field are presented in Figure 45. Once again, the FMR data exhibit an asymmetry that makes it deviates from the model given by equations 1.44 and 1.45. We extracted a coupling strength of $g/(2\pi) = 41\,\text{MHz}$ and a dissipation rate of $\gamma/(2\pi) = 860\,\text{MHz}$. The relatively minor changes in the dissipation parameter, compared to those measured at room temperature, suggest that the dissipation mechanism is not substantially affected

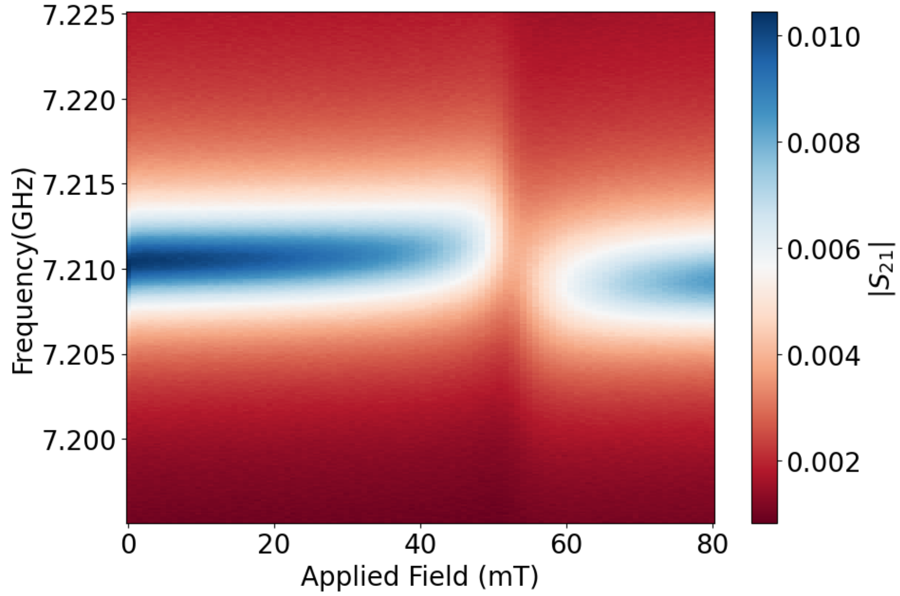

Figure 44 – Measured spectrum at 7 mK. For this measurement the attenuator was set at 35 dB showing the typical anti-crossing features at 53 mT.

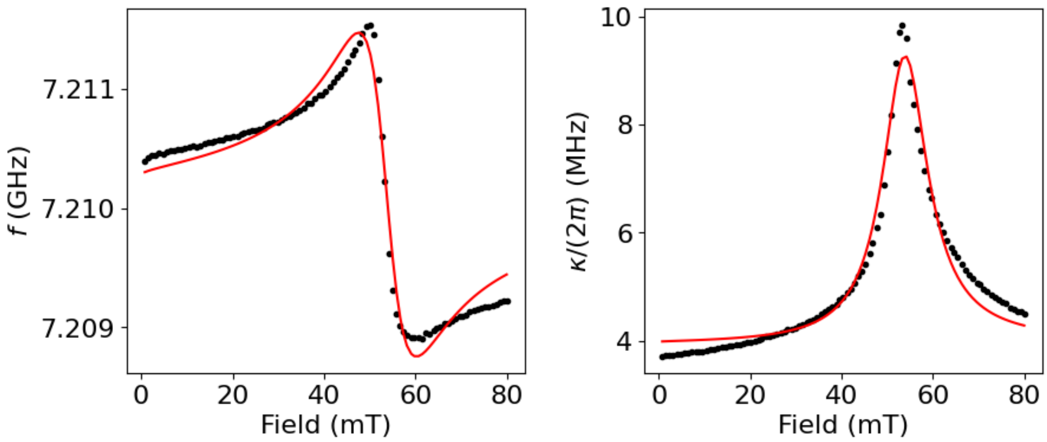

Figure 45 – Measured dispersion and absorption of the cavity-wire system at 7 mK and in red the fit based in equations 1.45, 1.44.

by temperature reduction. The coupling strength had a significant change, from its room temperature value of $g/(2\pi) = 25\,\mathrm{MHz}$, which could be due to a change in the material properties, like conductivity. Additionally, the saturation magnetization was fitted according to the Kittel formula (1.29), yielding a value of $\mu_0 M = 1.18\,\mathrm{T}$, which is an increase from $0.84\,\mathrm{T}$.

4.5 Purcell Effect and Cavity Ringdown

Despite the magnetic system's high dissipation, characterized by $\eta \gg g$, which prevents achieving strong coupling even at low temperatures, the cavity maintains relatively

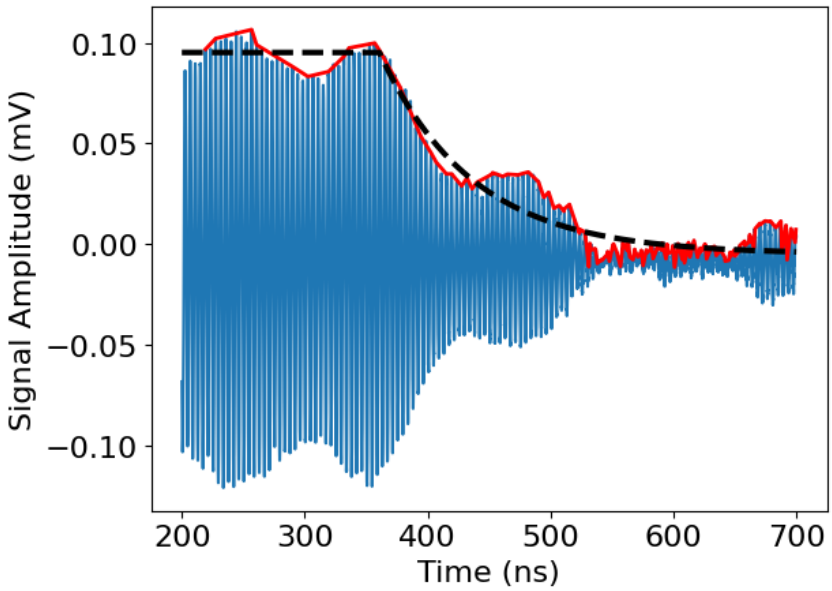

Figure 46 – A cavity ringdown signal snapshot taken at 0 mT in blue. The signal have 240 MHz of frequency. In red the amplitude of this snapshot is highlighted. It is clear that the signal decays with time. A exponential decay was fitted holding the dashed black line.

good quality with $g > \kappa$. These values make possible the observation of the Purcell effect (ZHANG et al., 2014; ZHAO; WANG; QIAN, 2025). The Purcell effect in atomic physics happens when there is an increase of the density of states of photons at an emitter (such an atom) position. This can happen for example by placing an atom in a cavity. From Fermi's Golden Rule, the emission rate of the emitter will be proportional to the density of final states, thus enhancing the decay rate of the emitter. For the case in question, the photon in the cavity, that have a decay rate κ, have an increase in decay rate when the cavity-magnet system is in resonance. The resonance allows efficient transferring of quanta from the cavity to the magnet, increasing the effective interaction with, or making available the decay channels associated with the wire.

The photon lifetime is associated with the ability of the cavity of holding photons. The photons will eventually be lost for internal baths, like the ones associated with resistance, imperfections of the surface and, in the present case, with the lossy magnetic system. Photons also leak out the cavity from the ports that connect it with external measurement circuitry (Figure 6); these photons are a probe of the intra cavity field and, in the case of an initial population of photons in a not driven cavity, the probe will see the exponential decay of the cavity photons. The photon lifetime is given by the characteristic time of this power decay.

To directly see the Purcell effect, a cavity ringdown spectroscopy was performed in the cavity-magnet system. In this measurement technique, an electromagnetic pulse in the cavity's resonance frequency is sent into the cavity and the transmitted pulse is recorded. The end tail of the pulse will have the exponential decay from which the photon lifetime is calculated . In the measurement, a 200 µs long square pulse of 7.21 GHz was sent into the system and the output signal from the cavity was recorded in a fast oscilloscope using a home-made heterodyning circuit. The setup used were presented in figures 25 and 24. Figure 46 shows a typical signal captured by the oscilloscope. The signal is 240 MHz and has a decaying amplitude. For each external magnetic field applied, a snapshot like this was taken 100 times. The amplitude envelope was fitted in Equation 4.2, determining the characteristic decay time τ_{photon} that was then averaged with the other measurements. Figure 47 illustrates the average decay curves against the maximum amplitude of all measurements for 0 mT and at the resonance. The Purcell effect is evident in the difference of the decay rates.

$$s = (A + c) + A \left[\exp\left(-\frac{(t - t_0)}{2\tau_{\text{photon}}}\right) - 1\right] \theta(t - t_0) \tag{4.2}$$

Figure 48 plots τ_{photon} as a function of the external magnetic field. At zero magnetic field, $\tau_{\text{photon}} = (30.6 \pm 0.8)$ ns, from which it decreases monotonically to $\tau_{\text{photon}} = (12 \pm 1)$ ns at the resonance field of 53 mT, increasing again at higher magnetic fields.

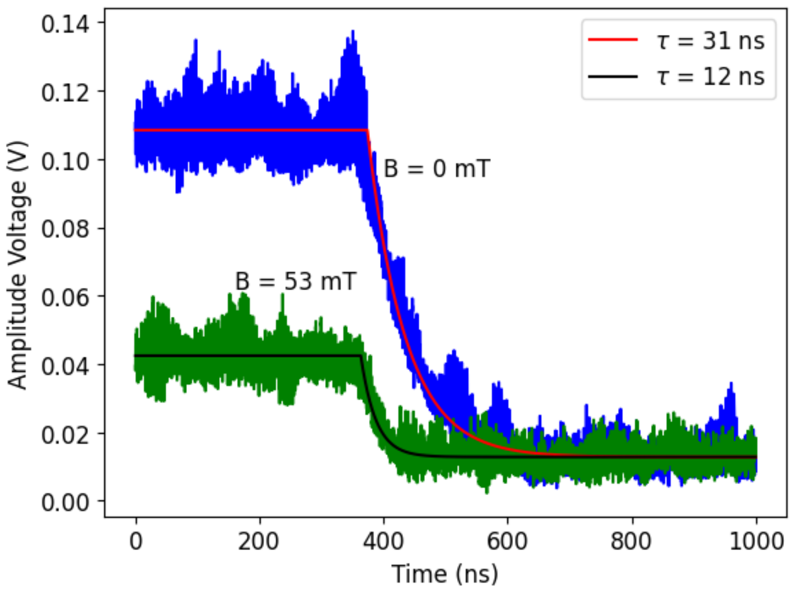

Figure 47 – Maximum of amplitude voltage for 100 measured signals and exponential decay fit at zero field and at resonance, showing the change in the photon lifetime.

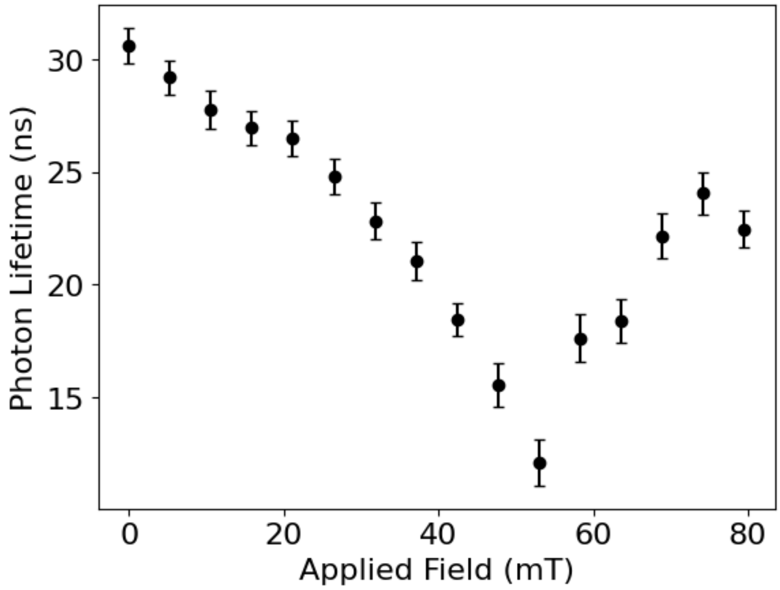

Figure 48 – Photon lifetime as a function of the applied field

4.6 Asymmetries and High Damping

Part of the asymmetry of the absorption and dispersion data (Figure 36) comes from the fact that the radius of the wire is in the order of the skin depth $R \sim \delta_0$, which also causes broadening of the absorption (see section 1.7, appendix B). Fitting the cavity absorption based in (KRAUS et al., 2011):

$$P_{abs} \propto \mathrm{Re}(\eta_0) \frac{8c\sqrt{\epsilon_0/\mu_0}}{\pi R\omega |H_0^{(2)}(\omega R/c) + i\sqrt{\epsilon_0/\mu_0}\eta_0 H_0'^{(2)}(\omega R/c)|^2}, \tag{4.3}$$

where η_0 is the surface impedance of mode $n = 0$ given by Equation1.54 and $H_0^{(2)}$ and $H_0'^{(2)}$ are the second order Hankel function and its derivative, the red curve in Figure 49 is obtained. The parameters fitted were the resistivity $\rho = (4.0 \pm 0.6) \times 10^{-7}\,\Omega\mathrm{m}$[7], the Gilbert constant $\alpha = 0.01$ and the magnetization $\mu_0 M_s = 0.83$ T. The agreement is slightly better than the previous Lorentzian fit, with $R^2 = 0.98$, and the curve accounts for some asymmetry. The improvement on the basis of the Lorentzian was significant as follows for measured data ever far from resonance. Other contributors for the asymmetry may include exchange effects, anisotropy and inhomogeneous dissipation mechanisms.

[7] This value is smaller than the usual resistivity reported in the literature for those wires, for example $\rho = 11 \times 10^{-7}\,\Omega\mathrm{m}$

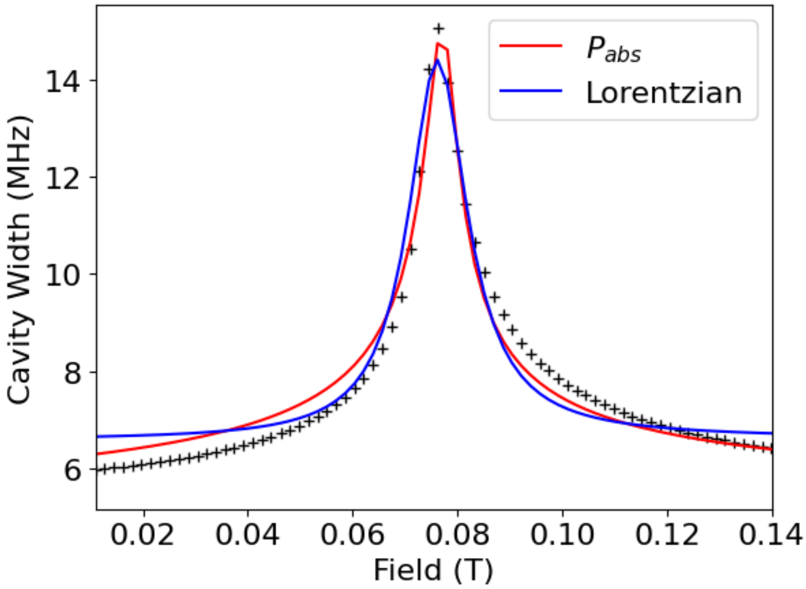

Figure 49 – Fitting of absorption based on the theory of FMR in wires by (KRAUS, 1982) (in red) compared to the Lorentzian fit (blue) of section 4.3.1 on the data of Figure 34.

In regards to the dissipation, it is interesting to first note that, from the Lorentzian fit, the total dissipation of the sample is in the order of 860 MHz. But following the fit of the absorbed power from the FMR theory in the wires, the fitted Gilbert parameter is only 0.01, corresponding to a Gilbert dissipation of 74 MHz. Considering the nature of the absorption by the surface impedance in Equation 4.3, much of this broadening comes from eddy current losses. So from this model, most of the dissipation would be ohmic of origin. An important mechanism of the magnetic dissipation that the model do not addresses is the loss by anisotropy dispersion (SOSSMEIER et al., 2010; de Cos; GARCíA-ARRIBAS; BARANDIARAN, 2008), in that the variation of the magnetic properties of the material along its volume, produce local resonances at shifted frequencies that broaden the curve. This mechanism was seen to be dominant for CoFeSiB for certain field range when the eddy current losses was removed (SOSSMEIER et al., 2010). So we assume it plays a role in our experiment too. A detailed investigation of the dissipation mechanisms and, for example, their dependence with temperature is left for future works. We note that Dyson's theory of ESR in metals (DYSON, 1955), where conduction electron diffuse in and out of the skin, presenting a asymmetric lineshape could probably be used to explain our results. We didn't pursued this approach though.

5 Conclusion

In this monograph the cavity-magnet coupling of metallic microwires in 3D cavities was studied. The metallic character of the wires and their aspect ratio presents the possibility of achieving this coupling using the electric fields of the cavity. This gives in fact a much larger coupling than the conventional setup. This coupling was explored in this work. Ferromagnetic experiments were performed using Vector Network Analyser and varying field, obtaining maps from which both the dispersion and the absorption of the coupled system could be measured. The results were first analysed using the model of two coupled harmonic oscillators, with the passive oscillator possessing high dissipation, causing the driven one to be perturbed according to linear response theory. From this, important parameters of the interaction like the coupling strength and dissipation could be obtained and interesting comparisons with the model made. Coupling strengths around 50 MHz could be reached, which is a good value for Cavity Magnonic experiments using 3D cavities and are impressive for such small magnetic system.

The coupling strength was then studied, and it was found that it is linear with the electric field of the unperturbed cavity and, apparently for our system, linear in the length also. Hence having an electric dipole nature.

The high dissipation is not completely understood, although eddy current losses should have a big impact on it. Also, there is the question of why it does not significantly change with the temperature. There could be competing temperature dependences on different mechanisms or simply there is little change on the main mechanism. A more careful investigation is needed to answer these questions.

Although the large dissipation prevented the system reaching the strong coupling regime, using the advanced measurement setup available to the LFDQ Lab while the sample was in the dilution refrigerator, a cavity ringdown spectrocopy was performed, directly showing the Purcell effect on the cavity photons.

Future works investigating those wires could characterize its dissipation and overall response in the range of frequencies and fields here considered. In regards to the electrically mediated interaction, a more thorough investigation is worthy. One of the problems to be solved is the exact format of the coupling: how g varies with the number of spins, the electric field, the geometry and the frequency. Another question that begs to be addressed given the discussion is if this sort of coupling could be used in Cavity Magnonics experiments to achieve the strong coupling regime. Will the eddy current losses be too big to impend it? Could a specially designed setup be used to easily achieve a controllable coupling a dissipation? These are interesting questions that could potentially lead to powerful applications in the field.

As a consequence of the project, several skills and technical tools were developed in the LFDQ that will form the basis of future endeavors in quantum magnonics.

Bibliography

ABE, E. et al. Electron spin ensemble strongly coupled to a three-dimensional microwave cavity. Applied Physics Letters, v. 98, n. 25, p. 251108, 06 2011. ISSN 0003-6951. Disponível em: <https://doi.org/10.1063/1.3601930>. Citado na página 25.

AL., D. L.-Q. et. Hybrid quantum systems based on magnonics. Appl. Phys. Express, v. 12, p. 070101, 2019. Citado na página 22.

AMENT, W. S.; RADO, G. T. Electromagnetic effects of spin wave resonance in ferromagnetic metals. Phys. Rev., American Physical Society, v. 97, p. 1558–1566, Mar 1955. Disponível em: <https://link.aps.org/doi/10.1103/PhysRev.97.1558>. Citado na página 28.

BOVENTER, I. R. Cavity Magnon-Polariton Spectroscopy. Tese (Doutorado) — Johannes Gutenberg University Mainz, Mainz, 2019. Citado 2 vezes nas páginas 24 and 55.

BROWN, W. F. Micromagnetics. [S.l.]: Interscience Publishers, 1963. Citado 2 vezes nas páginas 15 and 17.

CALDEIRA, A. O. An Introduction to Macroscopic Quantum Phenomena and Quantum Dissipation. [S.l.]: Cambridge University Press, 2014. Citado na página 15.

CHIRIAC, H. et al. In situ investigation of the magnetization processes in amorphous glass-covered wires by ferromagnetic resonance measurements. Journal of Applied Physics, v. 85, n. 8, p. 5453–5455, 04 1999. ISSN 0021-8979. Disponível em: <https://doi.org/10.1063/1.369973>. Citado 2 vezes nas páginas 35 and 53.

CHIRIAC, H.; ÓVáRI, T. Amorphous glass-covered magnetic wires: Preparation, properties, applications. Progress in Materials Science, v. 40, n. 5, p. 333–407, 1996. ISSN 0079-6425. Disponível em: <https://www.sciencedirect.com/science/article/pii/S0079642597000017>. Citado 3 vezes nas páginas 11, 32, and 36.

CHRISCHON, D. da S. Efeito do Tratamento Térmico na Relaxação Magnética de Microfios Amorfos de CoFeSiB Recobertos por Vidro. Dissertação (Mestrado) — Universidade Federal de Santa Maria, 2012. Citado na página 30.

COEY, J. M. D. Magnetism and Magnetic Materials. [S.l.]: Cambridge University Press, 2010. Citado na página 76.

de Cos, D.; GARCíA-ARRIBAS, A.; BARANDIARAN, J. Frequency dependence of the ferromagnetic resonance width in magneto-impedance measurements. Journal of Magnetism and Magnetic Materials, v. 320, n. 20, p. 2513–2516, 2008. ISSN 0304-8853. Proceedings of the 18th International Symposium on Soft Magnetic Materials. Disponível em: <https://www.sciencedirect.com/science/article/pii/S0304885308003958>. Citado na página 67.

DOWLING, J. P.; MILBURN, G. J. Quantum Technology: The Second Quantum Revolution. 2002. Disponível em: <https://arxiv.org/abs/quant-ph/0206091>. Citado na página 10.

DYSON, F. J. Electron spin resonance absorption in metals. ii. theory of electron diffusion and the skin effect. Phys. Rev., American Physical Society, v. 98, p. 349–359, Apr 1955. Disponível em: <https://link.aps.org/doi/10.1103/PhysRev.98.349>. Citado na página 67.

GAO, J. The Physics of Superconducting Microwave Resonators. Tese (Doutorado) — California Institute of Technology, 2008. Citado na página 84.

GILBERT, T. A phenomenological theory of damping in ferromagnetic materials. IEEE Transactions on Magnetics, v. 40, n. 6, p. 3443–3449, 2004. Citado na página 17.

GIRVIN, S. M. Modern Condensed Matter. [S.l.]: Cambridge University Press, 2019. Citado na página 18.

GRIFFITHS, D. J. Introduction to Electrodynamics. [S.l.]: Pearson Education, 2013. Citado na página 13.

GRIFFITHS, J. H. E. Anomalous high-frequency resistance of ferromagnetic metals. Nature, 1946. Citado na página 10.

HAROCHE, S.; RAIMOND, J.-M. Exploring the Quantum: Atoms, Cavities, and Photons. Oxford University Press, 2006. ISBN 9780198509141. Disponível em: <https://doi.org/10.1093/acprof:oso/9780198509141.001.0001>. Citado na página 10.

HOU, J. T.; LIU, L. Strong coupling between microwave photons and nanomagnet magnons. Phys. Rev. Lett., American Physical Society, v. 123, p. 107702, Sep 2019. Disponível em: <https://link.aps.org/doi/10.1103/PhysRevLett.123.107702>. Citado na página 11.

HUANG, H.-L. et al. Superconducting quantum computing: a review. Science China Information Sciences, Springer Science and Business Media LLC, v. 63, n. 8, jul. 2020. ISSN 1869-1919. Disponível em: <http://dx.doi.org/10.1007/s11432-020-2881-9>. Citado na página 10.

HUBERT, A.; SCHäFER, R. Magnetic Domains. [S.l.]: Springer Berlin, Heidelberg, 1998. Citado na página 15.

HUEBL, H. et al. High cooperativity in coupled microwave resonator ferrimagnetic insulator hybrids. Physical Review Letters, American Physical Society (APS), v. 111, n. 12, sep 2013. Disponível em: <https://doi.org/10.1103%2Fphysrevlett.111.127003>. Citado 2 vezes nas páginas 10 and 24.

JACKSON, J. D. Classical Electrodynamics. [S.l.]: John Wiley & Sons, 1962. Citado na página 13.

KIM, S. H. et al. Power-dependence measurement of the quality factor of superconducting microwave resonators at mk temperature. In: 29th Conference on Precision Electromagnetic Measurements (CPEM 2014). [S.l.: s.n.], 2014. p. 174–175. Citado na página 61.

KITTEL, C. On the theory of ferromagnetic resonance absorption. 1947. Citado 2 vezes nas páginas 10 and 19.

KRANENDONK, J. V.; VLECK, J. H. V. Spin waves. Rev. Mod. Phys., American Physical Society, v. 30, p. 1–23, Jan 1958. Disponível em: <https://link.aps.org/doi/10.1103/RevModPhys.30.1>. Citado na página 19.

KRAUS, L. Theory of ferromagnetic resonances in thin wires. Czech J Phys, v. 32, p. 1264–1282, 1982. Citado 4 vezes nas páginas 28, 29, 67, and 78.

______. 15 - ferromagnetic resonance in individual wires: From micro- to nanowires. In: VáZQUEZ, M. (Ed.). Magnetic Nano- and Microwires. Woodhead Publishing, 2015, (Woodhead Publishing Series in Electronic and Optical Materials). p. 449–486. ISBN 978-0-08-100164-6. Disponível em: <https://www.sciencedirect.com/science/article/pii/B9780081001646000151>. Citado 2 vezes nas páginas 29 and 40.

KRAUS, L. et al. Ferromagnetic resonance in microwires and nanowires. Phys. Rev. B, American Physical Society, v. 83, p. 174438, May 2011. Disponível em: <https://link.aps.org/doi/10.1103/PhysRevB.83.174438>. Citado 7 vezes nas páginas 28, 29, 30, 31, 66, 78, and 79.

LACHANCE-QUIRION, D. et al. Resolving quanta of collective spin excitations in a millimeter-sized ferromagnet. Science Advances, v. 3, n. 7, p. e1603150, 2017. Disponível em: <https://www.science.org/doi/abs/10.1126/sciadv.1603150>. Citado na página 10.

LANDAU, L.; LIFSHITZ, E. On the theory of the dispersion of magnetic permeability in ferromagnetic bodies. Phys. Zeitsch. der Sow. 8, pp. 153–169, 1935. Citado na página 15.

LIU, Y. J.; BARKER, R. C. Theory of transmission resonance in ferromagnetic metals. AIP Conference Proceedings, v. 24, n. 1, p. 505–506, 04 1975. ISSN 0094-243X. Disponível em: <https://doi.org/10.1063/1.29982>. Citado na página 28.

LO, C. K.; LAI, W. C.; CHENG, J. C. Note: Vector network analyzer-ferromagnetic resonance spectrometer using high Q-factor cavity. Review of Scientific Instruments, v. 82, n. 8, p. 086114, 08 2011. ISSN 0034-6748. Disponível em: <https://doi.org/10.1063/1.3626216>. Citado na página 40.

MCRAE, C. R. H. et al. Materials loss measurements using superconducting microwave resonators. Review of Scientific Instruments, v. 91, n. 9, p. 091101, 09 2020. ISSN 0034-6748. Disponível em: <https://doi.org/10.1063/5.0017378>. Citado na página 61.

PETERSAN, P. J.; ANLAGE, S. M. Measurement of resonant frequency and quality factor of microwave resonators: Comparison of methods. Journal of Applied Physics, v. 84, n. 6, p. 3392–3402, 09 1998. ISSN 0021-8979. Disponível em: <https://doi.org/10.1063/1.368498>. Citado 2 vezes nas páginas 83 and 84.

PIROTA, K. et al. Magnetic properties and giant magnetoimpedance in a cofesib glass-covered microwire. Journal of Magnetism and Magnetic Materials, v. 221, n. 3, p. L243–L247, 2000. ISSN 0304-8853. Disponível em: <https://www.sciencedirect.com/science/article/pii/S0304885300005540>. Citado 2 vezes nas páginas 36 and 53.

POBELL, F. Matter and Methods at Low Temperatures. [S.l.]: Springer Berlin, Heidelberg, 2007. Citado 2 vezes nas páginas 40 and 41.

POZAR, D. M. Microwave Engineering. [S.l.]: John Wiley & Sons, 2012. Citado 2 vezes nas páginas 31 and 38.

RAMESHTI, B. Z. et al. Cavity magnonics. Physics Reports, Elsevier BV, v. 979, p. 1–61, set. 2022. ISSN 0370-1573. Disponível em: <http://dx.doi.org/10.1016/j.physrep.2022.06.001>. Citado 2 vezes nas páginas 10 and 23.

REAGOR, M. et al. Reaching 10ms single photon lifetimes for superconducting aluminum cavities. Applied Physics Letters, AIP Publishing, v. 102, n. 19, maio 2013. ISSN 1077-3118. Disponível em: <http://dx.doi.org/10.1063/1.4807015>. Citado na página 61.

REZENDE, S. M. Fundamentals of Magnonics. [S.l.]: Springer Cham, 2020. Citado 5 vezes nas páginas 15, 17, 18, 20, and 49.

RODBELL, D. S. Ferromagnetic resonance of iron whisker crystals. Journal of Applied Physics, v. 30, n. 4, p. S187–S188, 04 1959. ISSN 0021-8979. Disponível em: <https://doi.org/10.1063/1.2185880>. Citado 2 vezes nas páginas 11 and 31.

______. Microwave magnetic field near a conducting perturbation. Journal of Applied Physics, v. 30, n. 11, p. 1845–1846, 11 1959. ISSN 0021-8979. Disponível em: <https://doi.org/10.1063/1.1735072>. Citado 2 vezes nas páginas 31 and 59.

SMITH, M. A. et al. Observation of room temperature exchange cavity magnon-polaritons in metallic thin films. Advanced Quantum Technologies, v. 7, n. 8, p. 2300420, 2024. Disponível em: <https://onlinelibrary.wiley.com/doi/abs/10.1002/qute.202300420>. Citado na página 55.

SOSSMEIER, K. D. et al. Ferromagnetic resonance linewidth mechanisms in annealed cofesib glass-covered microwires. Journal of Physics D: Applied Physics, v. 43, n. 5, p. 055003, jan 2010. Disponível em: <https://dx.doi.org/10.1088/0022-3727/43/5/055003>. Citado na página 67.

SOYKAL, O. O.; FLATTÉ, M. E. Strong field interactions between a nanomagnet and a photonic cavity. Phys. Rev. Lett., American Physical Society, v. 104, p. 077202, Feb 2010. Disponível em: <https://link.aps.org/doi/10.1103/PhysRevLett.104.077202>. Citado 2 vezes nas páginas 10 and 21.

STECK, D. A. Quantum and Atom Optics. 2012. Disponível em: <http://steck.us/teaching>. Citado na página 14.

TABUCHI, Y. et al. Hybridizing ferromagnetic magnons and microwave photons in the quantum limit. Phys. Rev. Lett., American Physical Society, v. 113, p. 083603, Aug 2014. Disponível em: <https://link.aps.org/doi/10.1103/PhysRevLett.113.083603>. Citado 2 vezes nas páginas 24 and 40.

TAYLOR, G. F. A method of drawing metallic filaments and a discussion of their properties and uses. Phys. Rev., American Physical Society, v. 23, p. 655–660, May 1924. Disponível em: <https://link.aps.org/doi/10.1103/PhysRev.23.655>. Citado na página 32.

WALLRAFF, A. et al. Strong coupling of a single photon to a superconducting qubit using circuit quantum electrodynamics. Nature, Springer Science and Business Media LLC, v. 431, n. 7005, p. 162–167, set. 2004. ISSN 1476-4687. Disponível em: <http://dx.doi.org/10.1038/nature02851>. Citado na página 10.

WALLS, G. J. M. D. Quantum Optics. [S.l.]: Springer Berlin, Heidelberg, 2008. Citado na página 23.

YUAN, H. et al. Quantum magnonics: When magnon spintronics meets quantum information science. Physics Reports, Elsevier BV, v. 965, p. 1–74, jun. 2022. ISSN 0370-1573. Disponível em: <http://dx.doi.org/10.1016/j.physrep.2022.03.002>. Citado na página 10.

ZHANG, X. et al. Strongly coupled magnons and cavity microwave photons. Physical Review Letters, American Physical Society (APS), v. 113, n. 15, out. 2014. ISSN 1079-7114. Disponível em: <http://dx.doi.org/10.1103/PhysRevLett.113.156401>. Citado 4 vezes nas páginas 10, 24, 40, and 64.

ZHAO, G.; WANG, Y.; QIAN, X. F. Theory of Magnon Purcell Effect in Cavity Magnonic System. 2025. Disponível em: <https://arxiv.org/abs/2501.06026>. Citado na página 64.

ZHUKOVA, V. et al. Development of magnetically soft amorphous microwires for technological applications. Chemosensors, v. 10, n. 1, 2022. ISSN 2227-9040. Disponível em: <https://www.mdpi.com/2227-9040/10/1/26>. Citado na página 32.

Appendix

APPENDIX A – Demagnetization Field

From Helmholtz theorem, the magnetic field $\mathbf{H}$ is decomposed in two vector fields: a solenoidal field $\mathbf{H}_C$ with zero divergence and a irrotational field $\mathbf{H}_D$ with zero curl. The first one is the part of the field produced by free currents, as Amperè law holds: $\boldsymbol{\nabla} \times \mathbf{H} = \boldsymbol{\nabla} \times \mathbf{H}_C = \mathbf{j}$; the other is the part produced by the permanent magnetic moments that makes up the magnetization; as it is curl-less it is the gradient of a potential:

$$\mathbf{H}_D = -\nabla\phi, \tag{A.1}$$

and from Gauss' law $\nabla \cdot \mathbf{B} = 0$, it follows that

$$\nabla \cdot \mathbf{H}_D = -\nabla \cdot \mathbf{M} \tag{A.2}$$

from where one gets the Poisson equation for magnetic potential:

$$\nabla^2\phi = -\nabla \cdot \mathbf{M}. \tag{A.3}$$

The field $\mathbf{H}_D$ is called demagnetization field inside the magnet and stray field outside of it. This Poisson equation can be solved by Green's function, giving the field produced by the magnetization of the magnet. The term $-\nabla \cdot \mathbf{M}$ is called density of magnetic change, in analogy to the Poisson equation of electrostatics.

The magnetostatic energy is the self energy of the magnet given by the energy of the dipoles $\mathbf{M}dV$ immersed in the field $\mathbf{H}_D$ produced by the other dipoles. Thus it is equal to:

$$E_M = -\frac{\mu_0}{2}\int dV \mathbf{H}_D \cdot \mathbf{M}, \tag{A.4}$$

where the factor of 2 comes to eliminate the double counting.

For a uniformly magnetized ellipsoidal specimen, the demagnetization field is related linearly to $\mathbf{M}$ by the demagnetization tensor (COEY, 2010):

$$H_{di} = -\sum_j N_{ij}M_j; \tag{A.5}$$

the tensor N_{ij} has unit trace, and is diagonal on the base of the ellipse's principal axes. For a sphere, $(N_x, N_y, N_z) = (1/3, 1/3, 1/3)$.

For a cylinder of length L and radius R, magnetized along its length (z direction), the magnetic surface charges will be at its extremities. If $L >> R$ this will be like point charges too far from each other and the demagnetization field along the cylinder will be small, so it is possible to see that for this geometry $N_z \to 0$ and due to the symmetry and normalization of the trace $N_x, N_y \to 1/2$. Flatting that cylinder, $R >> L$, now it is a situation like the parallel plates of a capacitor that from Gauss's law: $E \propto \sigma$; hence $H_z = M$, and consequently $N_z \to 1$, $N_x, N_y \to 0$. Although a specific direction of magnetization was chosen to find these factors, they only depend on geometry and could also be obtained from the "needle" (an extreme prolate ellipse) and "dish" (extreme oblate ellipse) limits of the the general demagnetization tensor for the ellipse.

APPENDIX B – Theory of FMR in Metallic Wires With Exchange

As developed by Kraus (KRAUS, 1982).

When the exchange is considered, the equation 1.51 becomes bicubic. The three resulting wave branches are associated with different waves. One of them have the characteristics of nearly uniform precession (FMR), but all three can be excited and should be considered when evaluating the surface impedance with exchange effects. Using the Rado and Weertman boundary of conditions, the surface impedance is given by (KRAUS, 1982):

$$\eta_n = -\rho \frac{\begin{vmatrix} W_{n,U} & W_{n,S} & W_{n,N} \\ X_{n,U} & X_{n,S} & X_{n,N} \\ Y_{n,U} & Y_{n,S} & Y_{n,N} \end{vmatrix}}{\begin{vmatrix} V_{n,U} & V_{n,S} & V_{n,N} \\ X_{n,U} & X_{n,S} & X_{n,N} \\ Y_{n,U} & Y_{n,S} & Y_{n,N} \end{vmatrix}}, \tag{B.1}$$

where U,N, and S refers to the different wave branches, and X, Y, V and W, when there is no anisotropy, are defined by:

$$\begin{aligned} W_{n,j} &= \frac{k_j}{\mu_{eff,j}} J_n(k_j R), \\ V_{n,j} &= \frac{1}{2}\left[\frac{J_{n-1}(k_j R)}{\mu_{-,j}} - \frac{J_{n+1}(k_j R)}{\mu_{+,j}}\right], \\ X_{n,j} &= \left(\frac{1}{\mu_0} - \frac{1}{\mu_{-,j}}\right) k_j J'_{n-1,j}(k_j R) + \left(\frac{1}{\mu_0} - \frac{1}{\mu_{+,j}}\right) k_j J'_{n+1,j}(k_j R), \\ Y_{n,j} &= \left(\frac{1}{\mu_0} - \frac{1}{\mu_{-,j}}\right) k_j J'_{n-1,j}(k_j R) - \left(\frac{1}{\mu_0} - \frac{1}{\mu_{+,j}}\right) k_j J'_{n+1,j}(k_j R). \end{aligned} \tag{B.2}$$

For wires of small length compared to the cavity dimensions, the absorption for a mode is proportional to the real part of the correspondent surface impedance B.1 (KRAUS, 1982); for longer wires it is also proportional to the scattering moments of cylindrical waves that contain η_n in the denominator and produce changes in the absorption character (KRAUS et al., 2011). The expression for the absorption per unit of length for this last case is given by:

$$\frac{P_n}{P_{n,inc}} = \mathrm{Re}(\eta_n) \frac{8c\sqrt{\epsilon_0/\mu_0}}{\pi R \omega |H_n^{(2)}(\omega R/c) + i\sqrt{\epsilon_0/\mu_0}\eta_n H_n'^{(2)}(\omega R/c)|^2}, \tag{B.3}$$

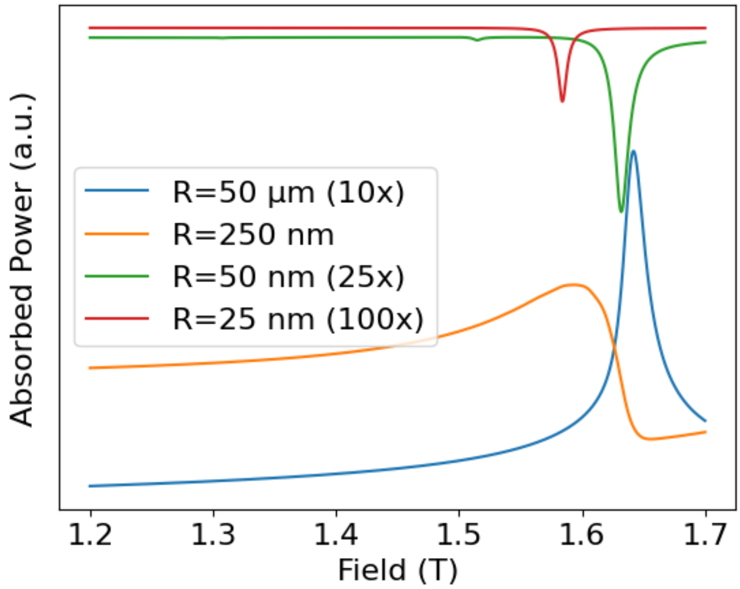

Figure 50 – Absorption curves simulated for magnetization mode $n = 0$ for different wire radius. The curves were escalated for allow comparison, as indicated in the legend. When the wire is bulk $R >> \delta_0$, the resonance happens on the Kittel plane condition. When they are comparable, the curve is asymmetric and broad. When $R << \delta_0$ there is not an absorption, but a transparency instead. The dislocation of the features is an exchange phenomenon. The small dip in the curve of $R = 50\mu$m in 1.51 T is due to spin waves.

where $P_{n,inc}$ is the incident power in that mode and $H_n^{(2)}$ and $H_n'^{(2)}$ are the Hankel function of the second-kind and its derivative, respectively.

Some of the curves presented in the article (KRAUS et al., 2011) were recalculated here using the above equations in *Wolfram Mathematica*. The code is displayed below. The parameters used were the same of the article: $f = 70$ GHz, $A = 2 \times 10^{-11}$ J/m, $\mu_0 M_s = 2.146\,\mathrm{T}$, $\alpha = 1.35 \times 10^{-3}$, $\rho = 97\,\mathrm{n\Omega m}$, which gives $\delta_0 = 592\,\mathrm{nm}$, Kittel Resonance condition for plane $H_{r,P} = 1.65\,\mathrm{T}$, and for cylinder $H_{r,C} = 1.43\,\mathrm{T}$. Figure 50 presents the simulation for mode $n = 0$, and Figure 51 for mode $n = 1$. When the $R >> \delta_0$, both resonances conditions tend happen in the plane condition, as explained in section 1.7. When $R \sim \delta_0$, the resonances broaden and deform. When $R << \delta_0$, the mode $n = 0$ presents a dip in the absorption, a transparency for field values smaller than the resonance condition – this dislocation in resonance is due to exchange effects – , while mode $n = 1$ have now a resonance in the Kittel condition for the cylinder, which is expected.

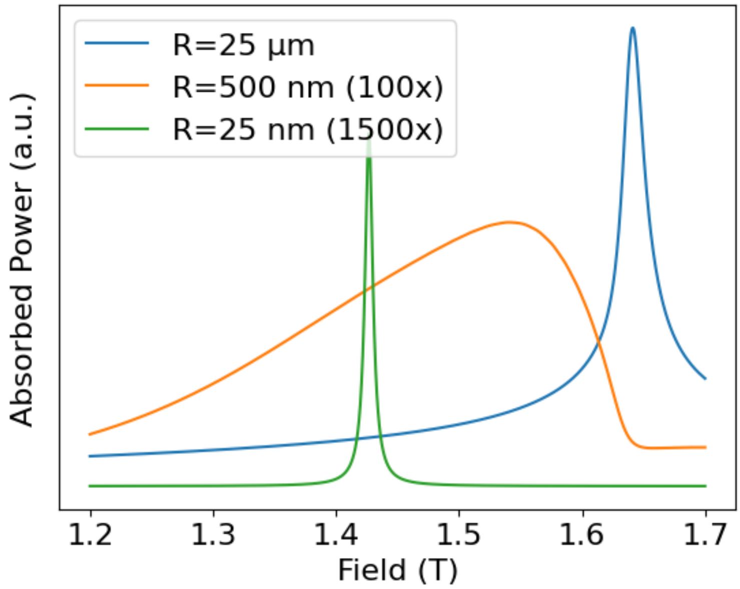

Figure 51 – Absorption curves simulated for magnetization mode $n = 1$ for different wire radius. The curves were escalated for allow comparison, as indicated in the legend. When the wire is bulk $R >> \delta_0$, the resonance happens on the Kittel plane condition. When they are comparable, the curve is asymmetric and broad. When $R << \delta_0$ the resonance condition shifts for the Kittel cylinder. This shows the transition of the dipolar mode from a situation when the skin effect dominates and the resonance only happens close to the surface, to the situation that the whole wire participates in the precession, equivalent to the insulator case.

Mathematica Code

```
rho = 97*10^-9;
alpha = 1.35*10^-3;
omega = 70*10^9;
mu0 = 4*Pi*10^-7;
M = 2.146;
gamma = 28*10^9;
delta0 = (2*rho/(2*Pi*omega*mu0))^0.5;
A = 2*10^-11;
epsilon0 = 8.85*10^-12;
c = 3*10^8;
kappa = 2*Pi*omega/c;
mup[B_, k_] =
  mu0*(B + M + I*alpha*omega/gamma + omega/gamma + mu0*A*k^2/
     M)/(B +
       I*alpha*omega/gamma + omega/gamma + mu0*A*k^2/M);

```

```
mum[B_, k_] =
  mu0*(B + M + I*alpha*omega/gamma - omega/gamma + mu0*A*k^2/
     M)/(B +
      I*alpha*omega/gamma - omega/gamma + mu0*A*k^2/M);
mueff[B_, k_] = 2*(1/mup[B, k] + 1/mum[B, k])^-1;

f[B_, k_] = k^2 + 2*I/delta0^2*mueff[B, k]/mu0;
V[B_, k_, r_, n_] =
  1/2*(1/mum[B, k]*BesselJ[n - 1, k*r] -
     1/mup[B, k]*BesselJ[n + 1, k*r]);
W[B_, k_, r_, n_] = k/mueff[B, k]*BesselJ[n, k*r];
X[B_, k_, r_,
   n_] = (1/mu0 - 1/mum[B, k])*
    k/2*(BesselJ[n - 2, k*r] - BesselJ[n, k*r]) + (1/mu0 -
      1/mup[B, k])*k/2*(BesselJ[n, k*r] - BesselJ[n + 2, k*r
         ]);
Y[B_, k_, r_,
   n_] = (1/mu0 - 1/mum[B, k])*
    k/2*(BesselJ[n - 2, k*r] - BesselJ[n, k*r]) - (1/mu0 -
      1/mup[B, k])*k/2*(BesselJ[n, k*r] - BesselJ[n + 2, k*r
         ]);
M1[B_, k1_, k2_, k3_, r_,
   n_] = {{W[B, k1, r, n], W[B, k2, r, n],
    W[B, k3, r, n]}, {X[B, k1, r, n], X[B, k2, r, n],
    X[B, k3, r, n]}, {Y[B, k1, r, n], Y[B, k2, r, n], Y[B, k3
       , r, n]}};

M2[B_, k1_, k2_, k3_, r_,
   n_] = {{V[B, k1, r, n], V[B, k2, r, n],
    V[B, k3, r, n]}, {X[B, k1, r, n], X[B, k2, r, n],
    X[B, k3, r, n]}, {Y[B, k1, r, n], Y[B, k2, r, n], Y[B, k3
       , r, n]}};
eta[B_, k1_, k2_, k3_, r_, n_] = -rho*
   Det[M1[B, k1, k2, k3, r, n]]/Det[M2[B, k1, k2, k3, r, n]];
P[etav_, r_, n_] =
 Re[etav]*8*(epsilon0/mu0)^0.5/(Pi*r*kappa*
     Abs[HankelH2[n, r*kappa] +
        I*(epsilon0/mu0)^0.5*
         etav*(HankelH2[n - 1, r*kappa] - HankelH2[n + 1, r*
```

```
            kappa])/2]^2);
listB = Range[1.2, 1.7, 0.5/999];
points = {};
Do[
 sol = NSolve[{f[B, k] == 0, Re[k] > 0}, k];
 ksol = k /. sol;
 etasol = eta[B, ##, 50*10^-6, 0] & @@ ksol;
 y = P[etasol, 50*10^-6, 0];
 AppendTo[points, {B, y}],
 {B, listB}
 ];
 ListPlot[points, PlotRange -> All]
```

APPENDIX C – Cavity Fitting

The expression for the transmission parameter can be obtained from Input-Output formalism or microwave circuit theory. It is given with the correct phase convention by Equation C.1, where f_0 standas for the resonance frequency of the cavity. Figure 52a shows a S_{21} in the complex plane, and the magnitude and phase. The plot of S_{21} on the complex plane is a frequency parameterized circle, which touches zero at $f = \pm\infty$ and the real line at $f = f_0$; the magnitude has a lorentzian shape peaked at the resonnace and the phase passes from π to $-\pi$, the circuit passes from a inductive character to a capacitive one.

$$S_{21} = \frac{\sqrt{\kappa_1 \kappa_2}}{i\left(f - f_0\right) + \frac{\kappa}{2}}, \tag{C.1}$$

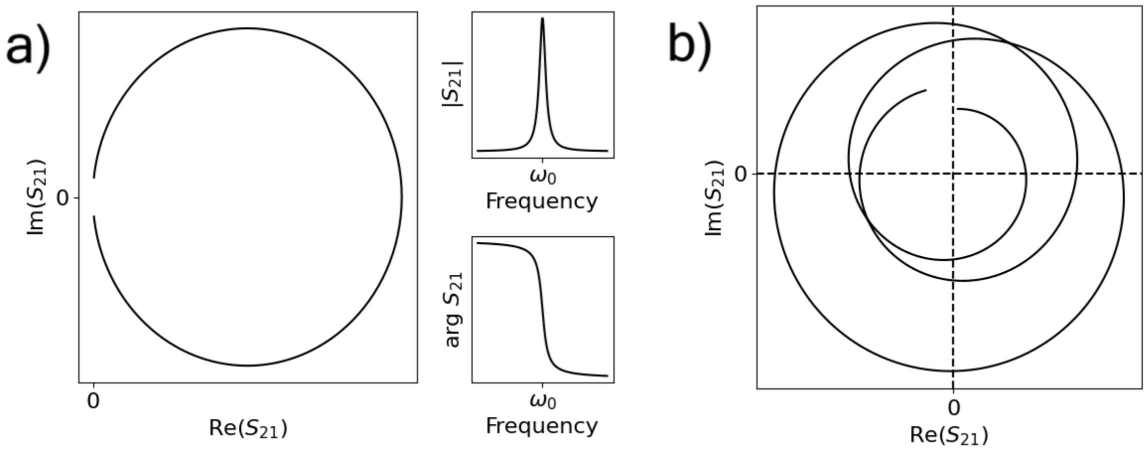

Figure 52 – a) Expected transmission parameter around the resonance of a cavity in the complex plane, in magnitude and phase. b) Transmission parameter in the presence of impedance mismatches and delay

In a real measurement setup, though, there will be changes on Equation C.1, due to impedance mismatches and cross talks (PETERSAN; ANLAGE, 1998). This introduces scaling, translation and a rotation of S_{21}. Along that, when the measurement plane does not coincide with the coupling ports of the resonator, for example due to the transmission line length of the probes, a frequency dependent shift from delay is also introduced, leading to a measured S_{21} closer to the form of Equation C.2, that in the complex plane shows as an enovalated trace like shown in Figure 52b.

$$\widetilde{S_{21}} = e^{i\zeta f}\left(\frac{Ae^{i\phi}}{1 + 2iQ\left(\frac{f}{f_0} - 1\right)} + X\right). \tag{C.2}$$

A VNA properly calibrated will remove these parameters; in the case the calibration is not performed, they have to be considered in the fitting procedure. A fitting procedure that corrects the data in the complex plane and obtains the resonace frequency and the quality factor accurately consists of the following steps (PETERSAN; ANLAGE, 1998; GAO, 2008):

- Correction of the phase/electrical delay (a lot of times visually)
- Circle Fit
- Translation followed by rotation of the circle to bring it to the origin (shifted by minus a radius (-r) from the canonical position of Figure 52)
- Fitting of the phase vs frequency given by Equation C.3

$$\phi = \phi_0 + 2\arctan\left[2Q\left(1 - \frac{f}{f_0}\right)\right] \tag{C.3}$$

Figure 53 shows this circle fit for the mode TE_{101} of the aluminum cavity 1. The fitted value of resonance frequency and quality for that mode were 7.435 GHz and 3060. Another fitting procedure, more simple, though less precise (PETERSAN; ANLAGE, 1998) is simply to fit in the magnitude data in the skewed Lorentzian given by:

$$|S_{21}|(f) = A_1 + A_2 f + \frac{|S_{max}| + A_3 f}{\sqrt{1 + 4\frac{f - f_0}{\Delta f}}}, \tag{C.4}$$

where Q is calculated by f_0 and Δf. Similarly, the other S parameters can be fitted. Note that the magnitude square of C.1 (same for the reflection parameter) is a proper Lorentzian.

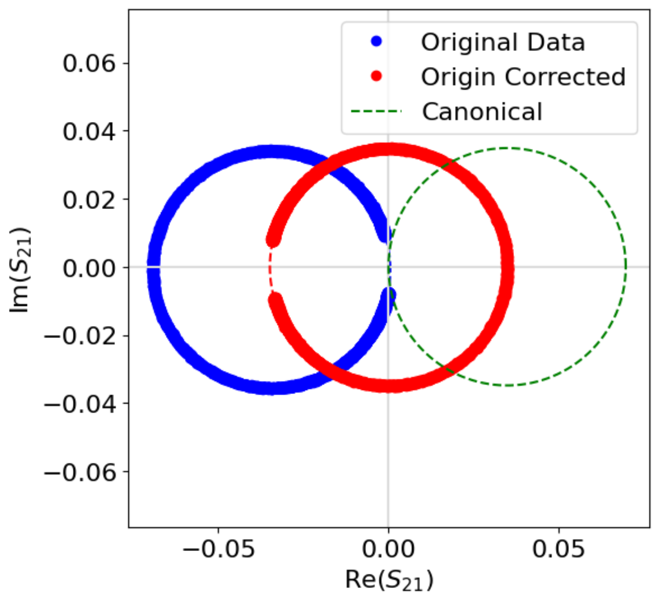

Figure 53 – Measurement of S_{21} by a calibrated VNA in blue, basically showing just a phase shift. The data was corrected to the canonical position and then shifted to the origin, shown in red.

APPENDIX D – Python Program to Control the Room T. System

```
import matplotlib.pyplot as plt
import numpy as np
import pyvisa
import time
import pandas as pd

rm = pyvisa.ResourceManager()
rm.list_resources()
fonte=rm.open_resource('GPIB0::6::INSTR')
vna=rm.open_resource('GPIB0::16::INSTR')
gauss=rm.open_resource('GPIB0::10::INSTR')
gauss.read_termination = '\r'
gauss.write_termination = '\r'
fonte.read_termination = '\r'
fonte.write_termination = '\r'

def writeB(B):
    C=1 #Conversion factor in A/T
    VMAX=20 #Maximum Voltage
    #Conversion Factors Obtained from Calibration

    C=36.01249612
    C2=-0.11840127
    I=C*B+C2
    if (I>=0):
        fonte.write('CURR {}; VOLT {} '.format(I,VMAX))
    if (I<0):
        fonte.write('CURR {}; VOLT {} '.format(I,-VMAX))
    return None

def zeroI():
    I=fonte.query('CURR?')
    I=float(I)
```

```
    for n in reversed(range(6)):
        i=str(I*n/6)
        fonte.write('CURR {}; VOLT 20'.format(i))
        time.sleep(2.5)

def measB():
    b=gauss.query('FIELD?')
    b=b.strip('\n')
    b=float(b)
    return b

def FMR_map_meas_all(Binicial,Bfinal,pB,finicial,ffinal,N,
   sleep,ifres,nome_arquivo):

    psweep=(ffinal-finicial)/N

    Blst=np.arange(Binicial,Bfinal+pB,pB)


    vna.write('SENS:SWE:POIN {}'.format(N))
    vna.write('SENS1:FREQ:START {}; :SENS1:FREQ:STOP {}'.
       format(finicial,ffinal))
    vna.write('SENS1:BANDwidth:RES {}'.format(ifres))
    vna.write(":SENSe1:AVERage:COUNt 10")
    vna.write('SENS1:BANDwidth:RES {}'.format(ifres))
    vna.write('DISP:WIND:TRAC1:Y:SCAL:AUTO')
    vna.write('SENS1:AVER:STATE ON')

    column_list=['B','freq', 'S11mag', 'S11ph', 'S21mag', '
       S21ph','S12mag','S12ph','S22mag','S22ph']

    DADOS = {}
    for column in column_list:
        DADOS[column]=[]


    for b in Blst:
        writeB(b)
        time.sleep(2)
```

```

        B=measB()

        vna.write('SENS1:AVER:CLE')
        vna.write(':DISPlay:WINDow1:TRACe1:Y:SCALe:AUTO')
        vna.write(':DISPlay:WINDow1:TRACe2:Y:SCALe:AUTO')
        vna.write(':DISPlay:WINDow1:TRACe3:Y:SCALe:AUTO')
        vna.write(':DISPlay:WINDow1:TRACe4:Y:SCALe:AUTO')
        vna.write('CALC:PAR:DEF MEAS,S21')
        time.sleep(sleep)
        vna.write('CALC:PAR:SEL MEAS')



        dados=vna.query('CALC:DATA:SNP?') #coleta o arquivo SNP com as medidas
        ''' SNP Format :
            Freq/S11 linmag/S11 ph/S21 linmag/ S21 ph/ S12 linmag/ S12 ph/ S22 linmag/ S22 ph
            Data comes in a long string
        '''

        lst=dados.split(',')
        for i in range(len(lst)):
            lst[i]=float(lst[i])

        DADOS['B'].append(B)
        for i,column in enumerate(column_list[1:]):
            DADOS[column].append(lst[N*i:N*(i+1)])

        vna.write('CALC:PAR:DEL MEAS')


    zeroI()

    final_data=pd.DataFrame(DADOS)
    final_data.to_csv("{}.csv".format(nome_arquivo), index = False)
    return DADOS
```

APPENDIX E – Python Module that creates a class to control the superconducting magnet

```python
'''
This module creates a class for the American Magnetics,Inc.
   Model 430 power supply programmer that controls the
   quadupolar power supply
4Q06125PS. The communication is realized by a ethernet
   connection.

Disclaimer:
This is a module under construction so it has few
   functionalities implemented, but if the ethernet
   connection is successfull,
any acceptable command or query can be send through these
   commands below. One should consult the manuals to get a
   full
understanding of the workings of the system and the different
    SCPI commands.

Comment about units:
Our model is (or should be) always set to use teslas and
   teslas/min. Other units may be set/used either by
   programming or
directly in the instrument. Just be aware to consider the
   correct values and change all the code acordingly.
'''



import socket
from time import sleep



class Model_430:
```

```

    def __init__(self,DeviceIP,timeout=10):
        self.DVM=socket.socket()
        self.DVM.settimeout(timeout)
        try:
            self.DVM.connect((DeviceIP, 7180))
            sleep(1e-2)
            print(self.DVM.recv(1024))
        except socket.timeout:
            print('Socket Timed Out')



    def query(self,question):
        '''
        This command sends a query to the instrument in the
           SCPI format.
        Example: instrument_name.query('CURR:SUPP?\n'). One
           should always add the end termination \n.
        '''
        self.DVM.send(question.encode())
        sleep(1e-2)
        try:
            response=self.DVM.recv(1024)
            return response
        except socket.timeout:
            print('Socket Timed Out')
            return None


    def write(self,command):
        '''
        This command writes a command onto the instrument in
           the SCPI format.
        Example: instrument_name.write('PAUSE\n'). One should
            always add the end termination \n.
        '''
        self.DVM.send(command.encode())

```

```python

    def field(self):
        '''
        This command queries the supply current in amp res, and from that, calculates the applied field in teslas
        with the coil conversion factor. So this command should give the current magnetic field generated by the coil
        in case the persistent switch heater is on.
        '''
        return float(self.query('CURR:SUPP?\n').decode().strip('\r\n'))*0.0912


    def ramp_to_and_monitor(self,value):
        '''
        This command initiates the field ramp to the inputed value in teslas. It is advised to determine and check the ramp rate
        beforehand.
        This command has a loop that print the current field value, monitoring the ramp. If one wants only to initiate the ramp
        and execute any other sequential line of code, it should use the ramp_to(value) command instead.
        '''
        self.field_target=value
        self.write('RAMP\n')
        sleep(1e-2)
        state=self.query('STATE?\n').decode().strip('\r\n')
        while state=='1':
            field_now=self.field()
            print(f'\r{field_now} T'+' '*100,end='\r',flush=True)
            sleep(1)
            state=self.query('STATE?\n').decode().strip('\r\n')
        final_field= float(self.query('CURR:SUPP?\n').decode
```

```
().strip('\r\n'))*0.0912
        print('Target Reached {}'.format(final_field))
        self.pause()

    def ramp_to(self,value):
        '''
        This command initiates the field ramp to the inputed value in teslas. It is advised to determine and check the ramp rate
        beforehand, though the ramp rate can usually be changed during the ramp. One can also use the command pause() to pause the ramp.
        '''
        self.field_target=value
        self.write('RAMP\n')


    def ramp_to_zero(self):
        '''
        This command ramps to zero field while monitoring. It is advised to determine and check the ramp rate beforehand.
        '''
        self.write('ZERO\n')

        while True:
            field_now=self.field()
            print(f'\r{field_now} T'+' '*100,end='\r',flush=True)
            sleep(1)
            if (abs(field_now)<5e-6):
                print('Field at Zero')
                break


    def pause(self):
        self.write('PAUSE\n')
```

```

    @property
    def ramp_rate(self):
        '''
        Get the ramp rate in teslas per minute
        '''
        result = self.query('RAMP:RATE:FIELD:1?\n').decode().strip('\r\n').split(',')[0]
        return result

    @property
    def field_target(self):
        '''
        Get the field target in teslas
        '''
        result= self.query('FIELD:TARG?\n').decode().strip('\r\n')
        return result

    @ramp_rate.setter
    def ramp_rate(self,value):
        '''
        Set the ramp rate value in teslas per minute of segment 1 and an upper bound field of 8 teslas.
        '''
        self.write('CONF:RAMP:RATE:FIELD 1,{},8\n'.format(value))

    @field_target.setter
    def field_target(self,value):
        '''
        Set the field_target value in teslas
        '''
        self.write('CONF:FIELD:TARG {}\n'.format(value))
```

APPENDIX F – *Autodesk Inventor* Projects

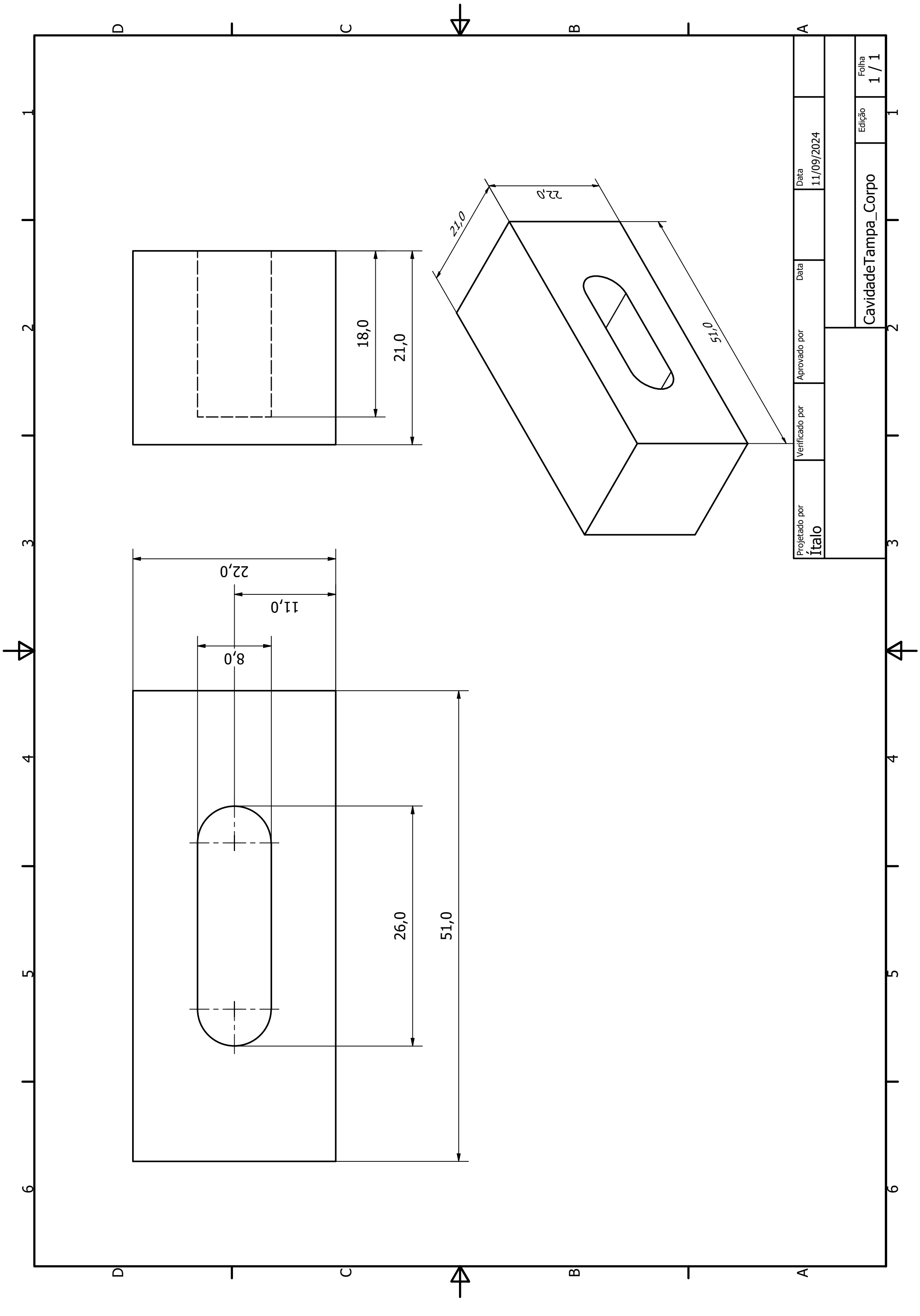

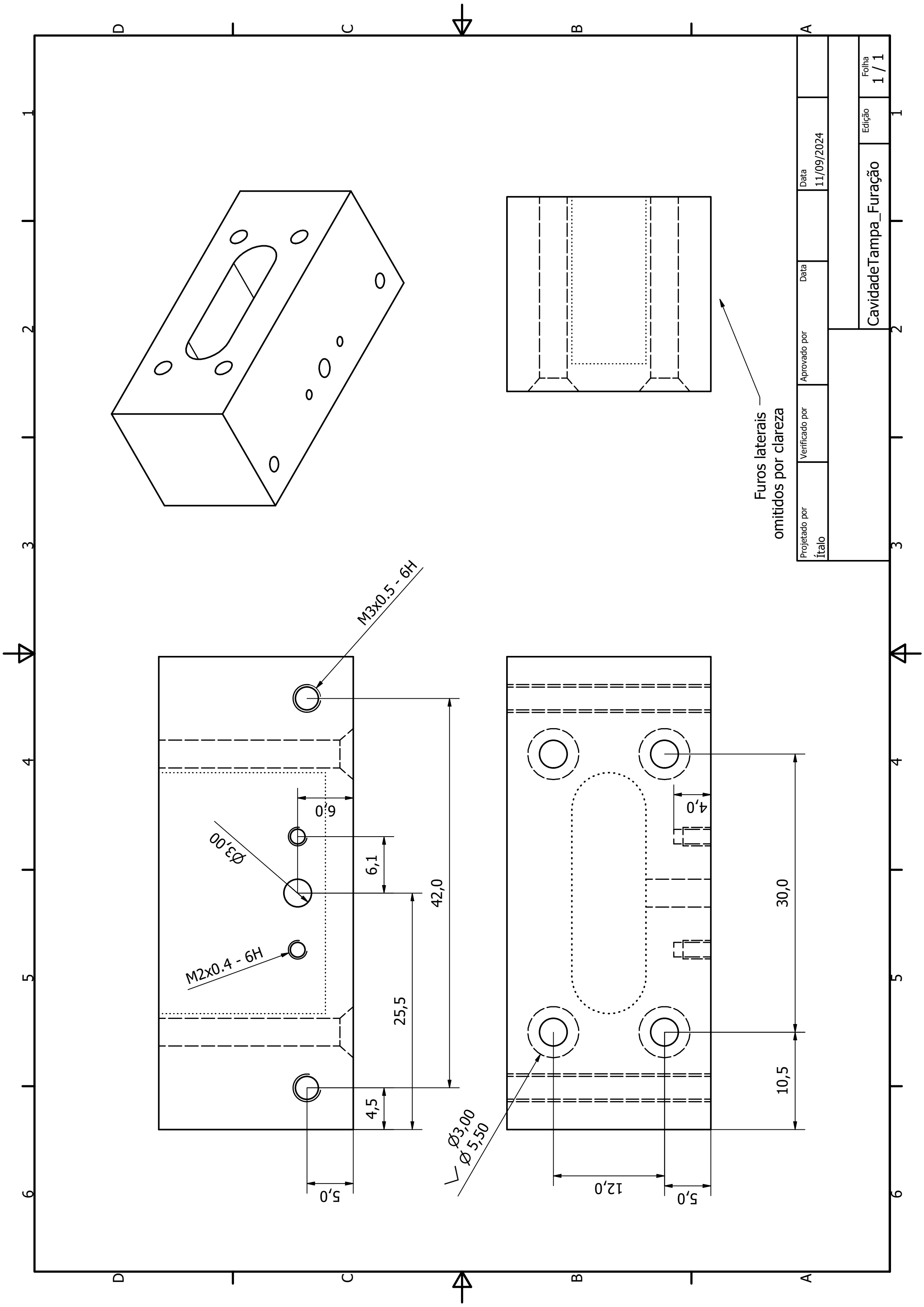

M3x0.5 - 6H
Ø3,00
M2x0.4 - 6H
6,0
6,1
42,0
25,5
4,5
5,0
Ø3,00
Ø 5,50
12,0
5,0
4,0
30,0
10,5
Furos laterais
omitidos por clareza
Projetado por
Ítalo
Verificado por
Aprovado por
Data
Data
11/09/2024
CavidadeTampa_Furação
Edição
1
Folha
1 / 1

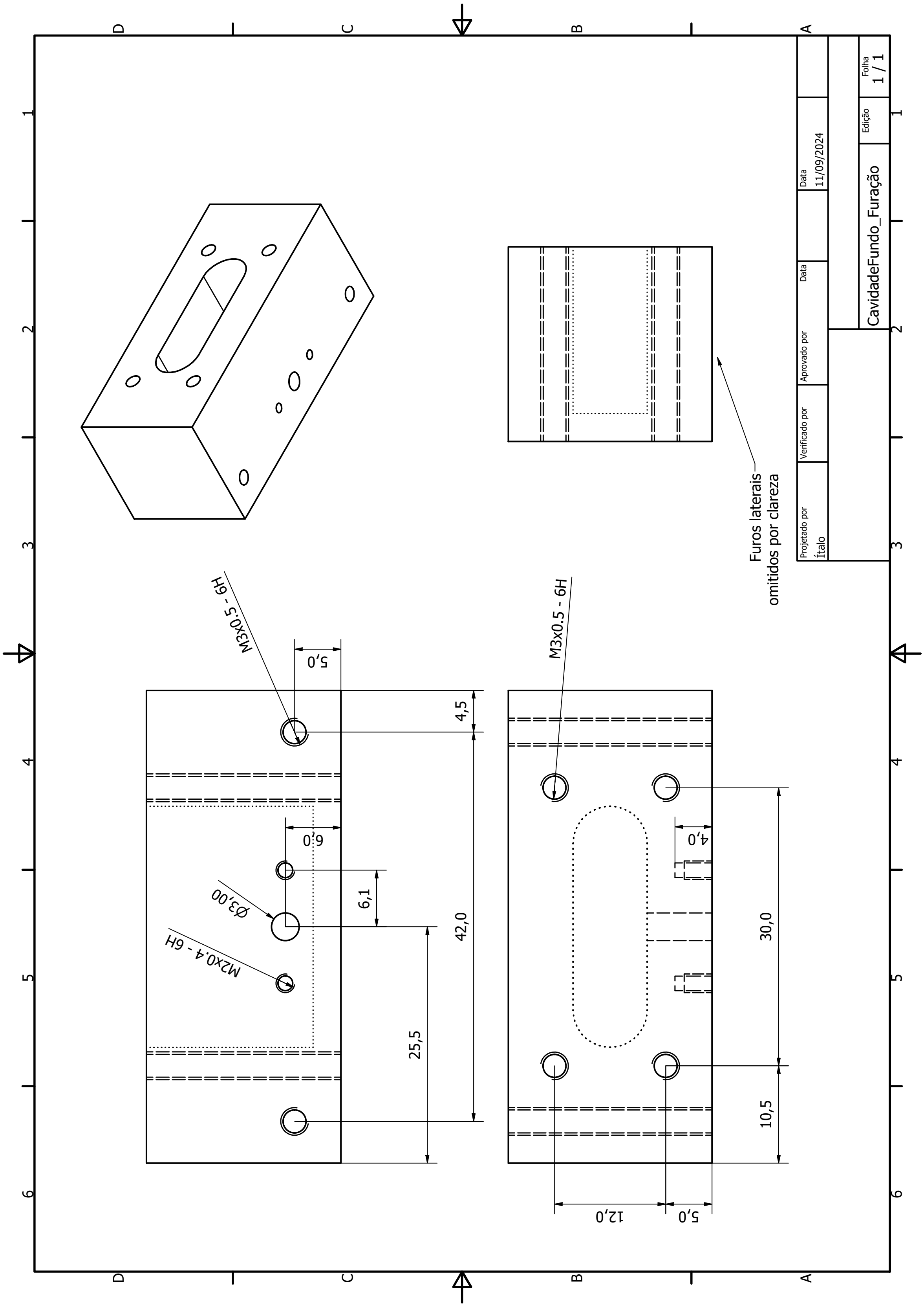

M3x0.5 - 6H
M3x0.5 - 6H
M2x0.4 - 6H
Ø3,00
5,0
4,5
42,0
6,0
6,1
25,5
4,0
30,0
10,5
12,0
5,0
Furos laterais omitidos por clareza
Projetado por
Ítalo
Verificado por
Aprovado por
Data
Data
11/09/2024
CavidadeFundo_Furação
Edição
Folha
1 / 1

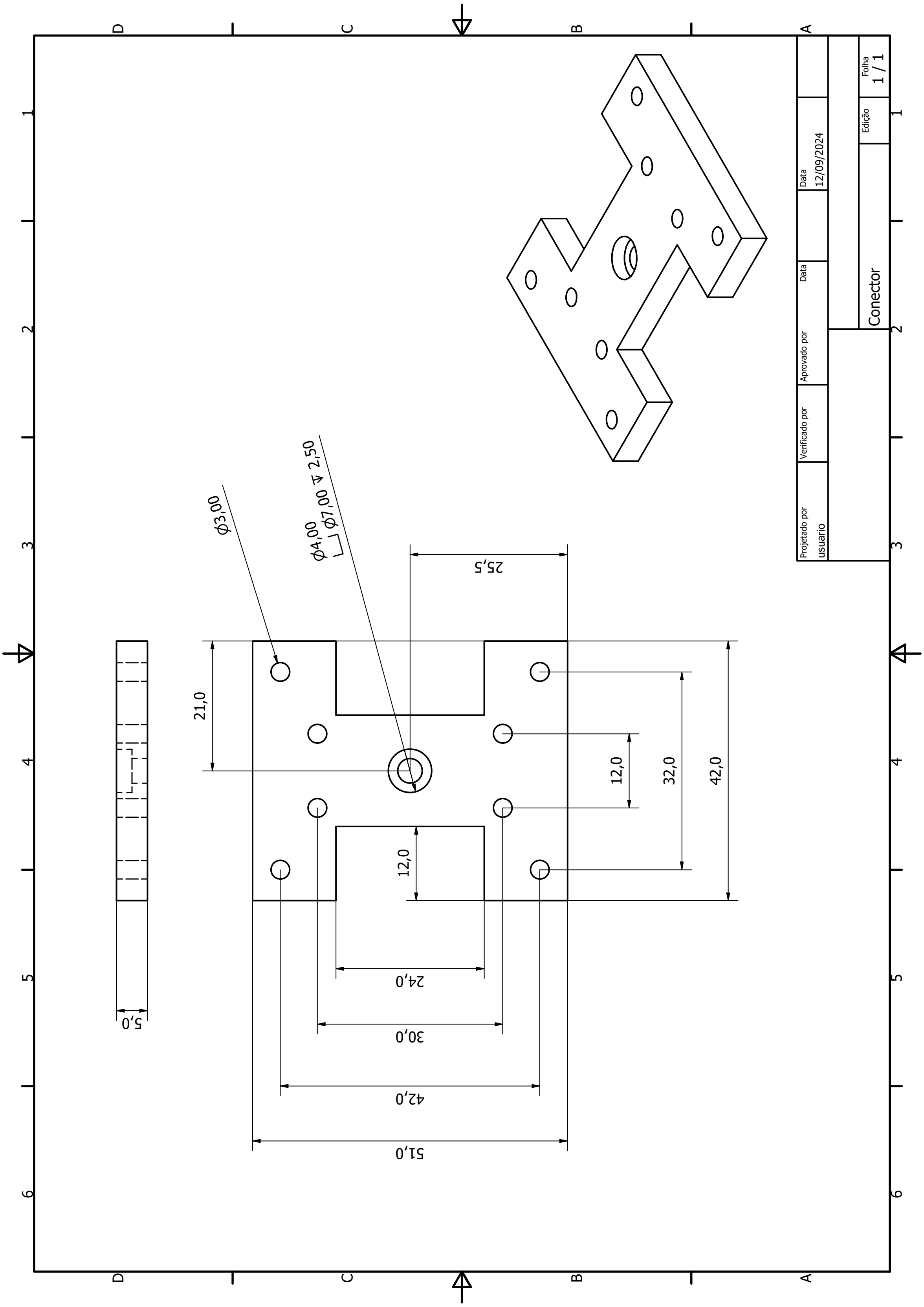
Projetado por
usuario
Verificado por
Aprovado por
Data
Data
12/09/2024
Conector
Edição
Folha
1 / 1
ϕ3,00
ϕ4,00
ϕ7,00 ↧ 2,50
25,5
21,0
12,0
32,0
42,0
12,0
24,0
30,0
42,0
51,0
5,0

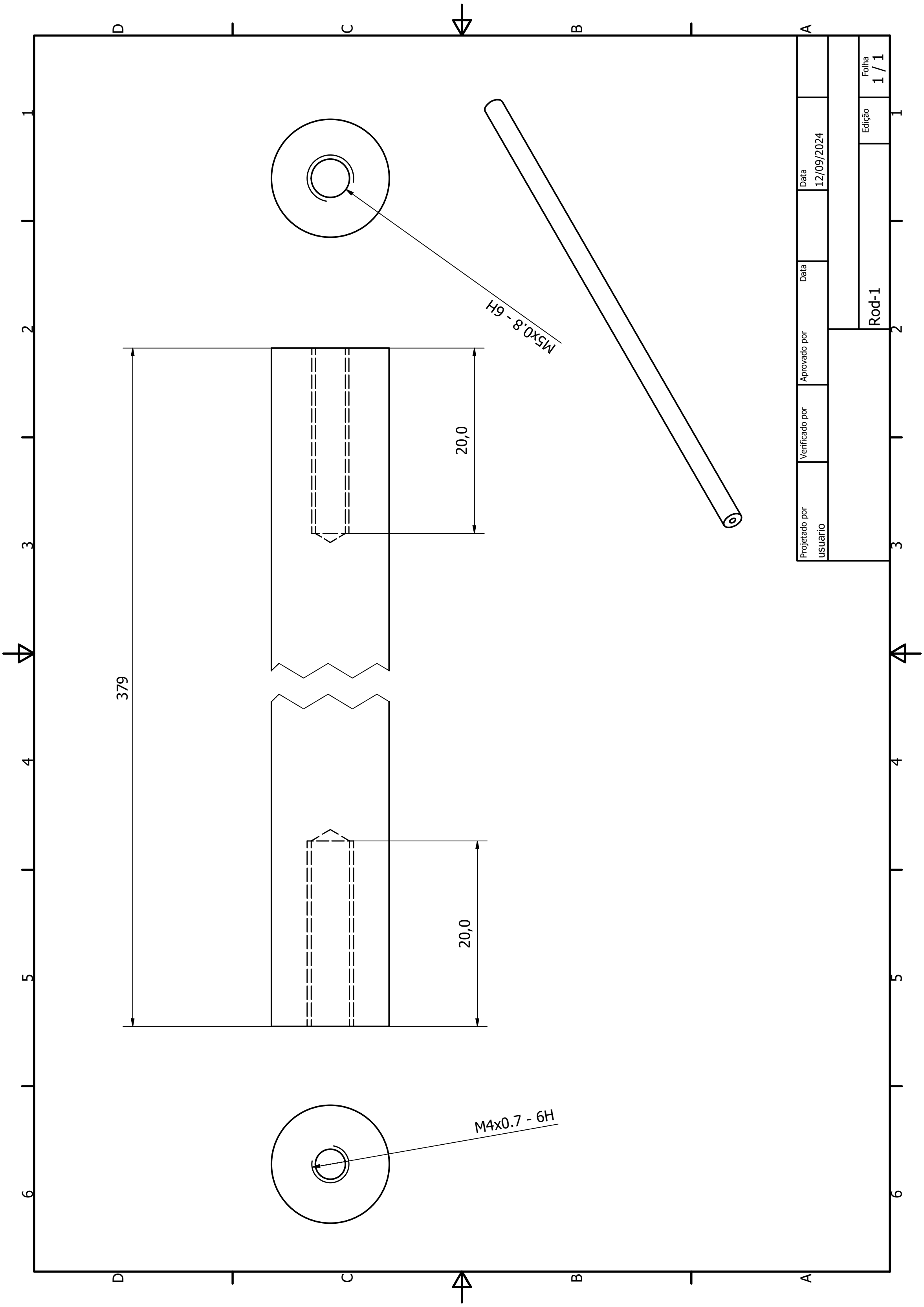
M5x0.8 - 6H
20,0
379
20,0
M4x0.7 - 6H
Projetado por
usuario
Verificado por
Aprovado por
Data
Data
12/09/2024
Rod-1
Edição
Folha
1 / 1

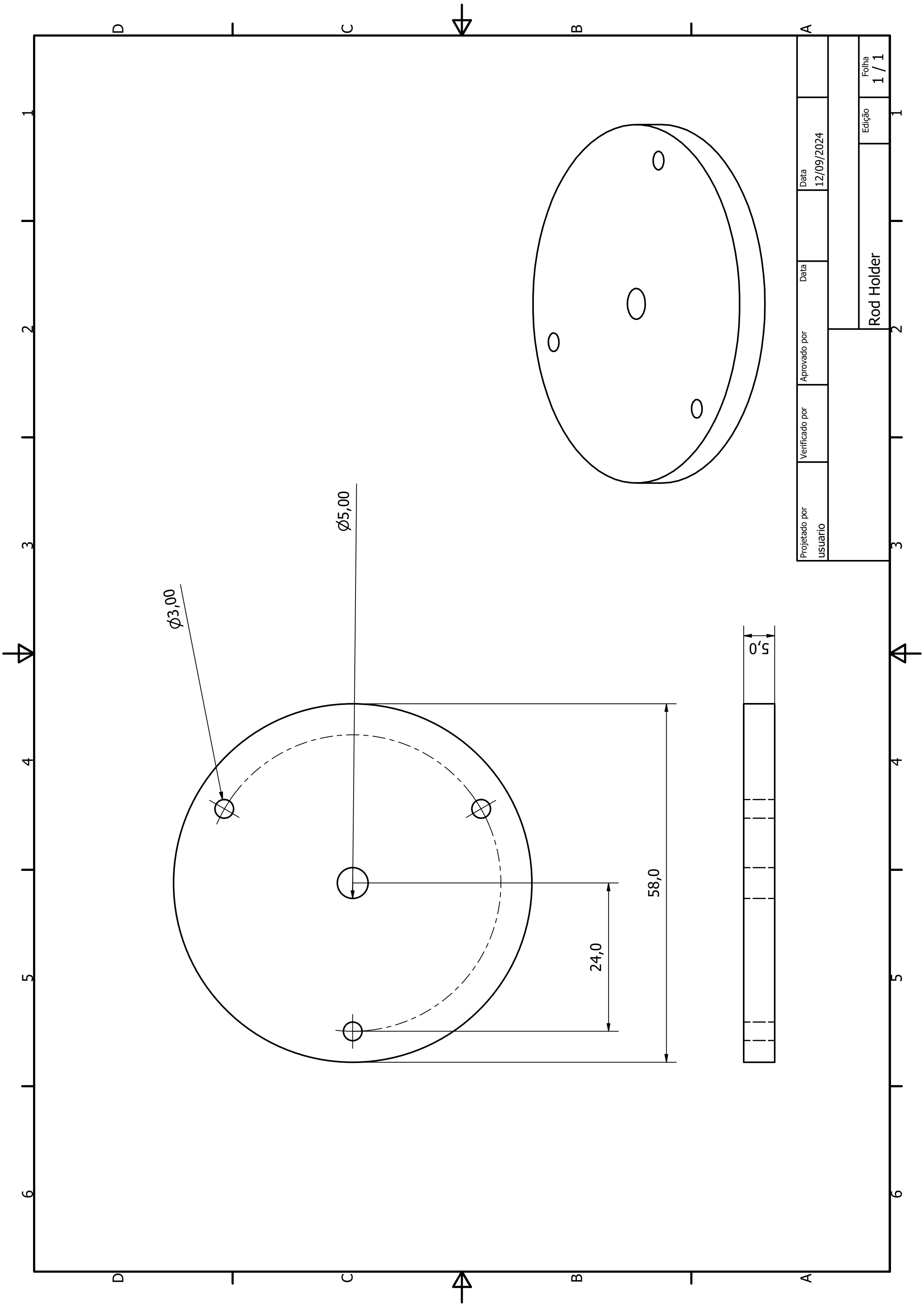
Projetado por
usuario
Verificado por
Aprovado por
Data
Data
12/09/2024
Rod Holder
Edição
Folha
1 / 1
Ø5,00
Ø3,00
58,0
24,0
5,0

APPENDIX G – Cavity Background Resonance

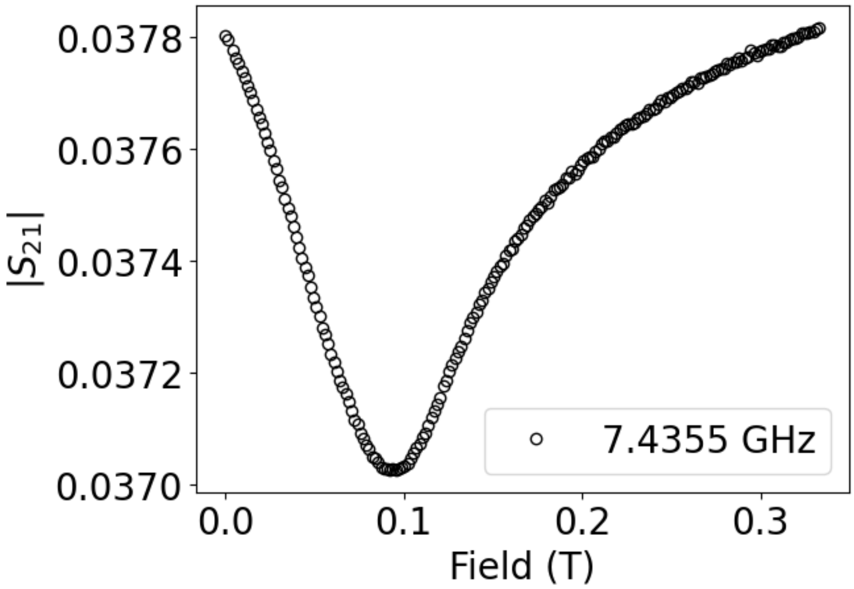

Figure 54 – FMR measurement of empty cavity A, showing a small resonance close to 0.1 T. The field at minimum is 92 mT. The amplitude of the signal is $\Delta S_{21} \sim 8 \times 10^{-4}$.